공학박사 학위논문

Hydrogen Production by Steam Reforming of Ethanol over Mesoporous Nickel-Alumina-Zirconia Catalysts

중형기공성 니켈-알루미나-지르코니아 촉매 상에서 에탄올의 수증기 개질 반응을 통한 수소 생산

2017 년 2 월

서울대학교 대학원

화학생물공학부

한 승 주

Abstract

Hydrogen Production by Steam Reforming of Ethanol over Mesoporous Nickel-Alumina-Zirconia Catalysts

Seung Ju Han
School of Chemical and Biological Engineering
The Graduate School
Seoul National University

As a renewable energy, hydrogen has received much attention on the basis of their potential contribution to the sustainable energy development. High energy density and environmental compatibility is main advantages of hydrogen utilization. Hydrogen production technologies can be classified into thermal processes, electrolyte processes, and photolytic processes. Although splitting of water through photo-catalysis and electrolysis is known as an ultimate method for hydrogen production, most hydrogen production is based on LNG (liquefied natural gas) reforming process which is still based on non-renewable fossil fuel system. Therefore, development of hydrogen production technology using renewable source is required to attain sustainability and fuel flexibility. In this situation, hydrogen production by bio-derived liquids

reforming has been studied, which is the most viable renewable hydrogen pathway in the near future. Among the bio-derived liquids, ethanol is the most feasible source for hydrogen production in the near term due to its non-toxicity, storage facility, and biodegradable nature. Moreover, bio-ethanol can be used as a source for SOFC vehicle which has potential to become an alternative transportation in the future. As a consequence, ethanol steam reforming is a promising technology for hydrogen production which is expected to mitigate the environmental problems.

For steam reforming of ethanol, Ni-based catalyst has been extensively used as a non-noble metal catalyst due to its low cost and high activity in C-C cleavage reaction. In general, Ni/Al_2O_3 catalyst has been widely employed for steam reforming of ethanol, because Al_2O_3 has large surface area and strong metal-support interaction with Ni particles. However, Al_2O_3 support with acidic nature induces ethanol dehydration, leading to coke formation. Therefore, many attempts have been made to increase both catalytic activity and durability of Ni/Al_2O_3 catalysts through modification of supporting materials. Alkaline earth metal oxides such as MgO and CaO have been used as promoters because they can suppress coke deposition by neutralizing acid sites of Al_2O_3. Addition of lanthanide oxides can also increase the catalytic activity by promoting gasification reaction of dissolved carbon species on the surface of nickel catalysts. Among various metal oxides, ZrO_2 is known to be the effective promoter for Ni/Al_2O_3 catalysts in the steam reforming of ethanol, because ZrO_2 can not only enhance the stability of the catalysts but also promote adsorption and dissociation of water on the surface of nickel catalysts.

In this work, in order to achieve efficient catalyst for steam reforming of ethanol, mesoporous nickel-alumina-zirconia catalysts were designed by various catalyst compositions and preparation methods, including epoxide-driven sol-gel method, P123-assissted sol-gel method, supercritical CO_2 drying method, and copper addition.

First of all, a series of mesoporous nickel-alumina-zirconia xerogel catalysts (denoted as Ni-AZ-X) with different Zr/Al molar ratio (X) were prepared by a single-step epoxide-driven sol-gel method, and they were applied to the hydrogen production by steam reforming of ethanol. Surface area of Ni-AZ-X catalysts decreased with increasing Zr/Al molar ratio due to the lattice contraction of ZrO_2 caused by the incorporation of Al^{3+} into ZrO_2. Interaction between nickel oxide species and support (Al_2O_3-ZrO_2) decreased with increasing Zr/Al molar ratio through the formation of NiO-Al_2O_3-ZrO_2 composite structure. Acidity of reduced Ni-AZ-X catalysts decreased with increasing Zr/Al molar ratio due to the loss of acid sites of Al_2O_3 by the addition of ZrO_2. Among the catalysts tested, Ni-AZ-0.2 (Zr/Al = 0.2) catalyst with an intermediate acidity exhibited the best catalytic performance in the steam reforming of ethanol.

A series of mesoporous nickel-alumina-zirconia xerogel catalysts (denoted as XNiAZ) with different nickel content (X, wt%) were prepared by a single-step epoxide-driven sol-gel method. All the XNiAZ catalysts exhibited a well-developed mesoporous structure and they dominantly showed an amorphous NiO-Al_2O_3-ZrO_2 composite phase, leading to high dispersion of NiO. Nickel surface area and reducibility of XNiAZ catalysts showed volcano-shaped trends with respect to nickel content. Among the catalysts tested, 15NiAZ catalyst with the highest nickel surface area exhibited the best catalytic performance in the steam reforming of ethanol.

A mesoporous nickel-alumina-zirconia aerogel (Ni-AZ) catalyst was prepared by a single-step epoxide-driven sol-gel method and a subsequent supercritical CO_2 drying method. For comparison, a mesoporous alumina-zirconia aerogel (AZ) support was prepared by a single-step epoxide-driven sol-gel method, and subsequently, a mesoporous nickel/alumina-zirconia aerogel (Ni/AZ) catalyst was prepared by an incipient wetness impregnation method. Although both catalysts retained a mesoporous structure, Ni/AZ catalyst showed lower surface area than Ni-AZ catalyst. From TPR, XRD, and H_2-TPD results, it was revealed that Ni-AZ catalyst retained higher reducibility and higher nickel dispersion than Ni/AZ catalyst. In the hydrogen production by steam reforming of ethanol, Ni-AZ catalyst with superior textural properties, high reducibility, and high nickel surface area showed a better catalytic performance than Ni/AZ catalyst.

A series of mesoporous nickel-alumina-zirconia xerogel (denoted as X-NAZ) catalysts were prepared by a P123-assisted epoxide-driven sol-gel method under different P123 concentration (X, mM), and they were applied to the hydrogen production by steam reforming of ethanol. All the catalysts retained a mesoporous structure. Pore volume of the catalysts increased with increasing P123 concentration. Nickel surface area and ethanol adsorption capacity of X-NAZ catalysts exhibited volcano-shaped trends with respect to P123 concentration. Among the catalysts tested, 12-NAZ catalyst with the highest Ni surface area and the largest ethanol adsorption capacity showed the best catalytic performance in the steam reforming of ethanol.

A series of mesoporous copper-nickel-alumina-zirconia (XCNAZ) xerogel catalysts with different copper content (X, wt%) were prepared by a single-step epoxide-driven sol-gel method, and they were applied to the hydrogen production by steam reforming of ethanol. All the calcined XCNAZ catalysts retained a mesoporous structure, and their surface area increased with increasing copper content. Metal-support interaction of XCNAZ catalysts decreased with increasing copper content due to the electronic effect. Nickel surface area and ethanol adsorption capacity of the catalysts exhibited volcano-shaped trends with respect to copper content. Among the catalysts, 0.2CNAZ catalyst exhibited the highest nickel surface area and the largest ethanol adsorption capacity. Catalytic performance in the steam reforming of ethanol over XCNAZ catalysts showed a volcano-shaped trend with respect to copper content. This result was well matched with the trend of nickel surface area. Among the catalysts tested, 0.2CNAZ catalyst with the highest nickel surface area showed the highest hydrogen yield.

In summary, various physicochemically-modified nickel-alumina-zirconia catalysts were designed and they were applied to the hydrogen production by steam reforming of ethanol in this study. In order to elaborate the effect of physicochemical properties of catalyst on catalytic performance in the steam reforming of ethanol, several characterizations such as N_2 adsorption-desorption, XRD, TPR, TEM, XPS, H_2-TPD, EtOH-TPD, and in-situ FT-IR analyses were conducted. It was concluded that nickel surface area served as a crucial factor determining the catalytic performance in the hydrogen production by steam reforming of ethanol.

Keywords: Hydrogen production, Steam reforming of ethanol, Nickel catalyst, Epoxide-driven sol-gel method, CO_2 supercritical drying, Copper, Xerogel, Aerogel

Student Number: 2012-20983

Contents

List of Tables

List of Figures

Chapter 1. Introduction

1.1. Hydrogen energy

The global energy demand is expected to increase rapidly due to population growth, urbanization, and modernization [1]. According to the UN report, the world population is projected to reach 8.5 billion by 2030 and 9.7 billion by 2050. However, most global energy supply relies on fossil fuel and extensive utilization of fossil fuel has accelerated its depletion [2]. The utilization of fossil fuel has also caused environmental problems such as air pollution and global warming. Although fossil fuel will last for a few more decades, it will not be able to meet the world's growing energy demand in the future. In this situation, development of renewable energy source is required to reduce dependence on fossil fuel and to cope with future energy demand [3]. As a renewable energy, hydrogen has received much attention on the basis of their potential contribution to the sustainable energy development. Hydrogen is abundant, nontoxic, and clean energy which burns clean with only water [4,5]. Moreover, hydrogen has the highest energy content per unit of weight (> 140 kJ/g) than any other known fuels (Table 1.1). Therefore, investigation and optimization of hydrogen production technology is required for stable and efficient hydrogen supply.

Table 1.1

Energy density and hydrogen to carbon ratio of various fuels

Fuel	Energy density (MJ/kg)	H/C ratio
Hydrogen	142.0	-
Natural gas	55.5	4.0
LPG	50.0	2.5-2.7
Methanol	22.5	4.0
Biogas (from gasifier)	4-14	0.7-2.0
Ethanol	29.7	3.0
Gasoline	45.8	1.6-2.1
Jet fuel	46.3	1.6-2.0
Diesel	45.3	1.8-2.3

1.2. Hydrogen production and utilization

Hydrogen energy is primarily used in petroleum refining, ammonia production, desulphurization, metal refining, Fischer-tropsch (FT) synthesis, and synthesis of methanol, ethanol, dimethyl ether [6,7]. In particular, hydrogen is being majorly used for production of ammonia and chemical compounds.

The prospect of hydrogen as an energy carrier is closely linked to the growth of fuel cell market. The main application areas of fuel cell are transportation, stationary power, and portable power [8]. According to the Department of Energy (DOE) of U.S., more than 80% of fuel cells were used in stationary application in 2013. There are various types of fuel cells, including polymer electrolyte membrane fuel cell (PEMFC), alkaline fuel cell (AFC), phosphoric acid fuel cell (PAFC), molten carbonate fuel cell (MCFC), and solid oxide fuel cell (SOFC) [9]. Among the fuel cell types, PEMFCs provide high power density and can be operated at relatively low temperature (50-100 ^{o}C). However, PEMFC requires hydrogen-rich stream with low CO concentration. On the other hand, SOFC system is available for generating power from hydrogen, natural gas, and other renewable fuels. Due to its fuel flexibility, SOFC has attracted much attention to become an alternative transportation system in the future.

According to the Department of Energy (DOE) of U.S., the global market for fuel cells grew by almost 400% between 2008 and 2013. Due to the rapid growth of fuel cell market, demand of hydrogen is expected to grow in the near future. Because hydrogen is the major source for fuel cell, hydrogen has the potential to be used in various fields including transportation, electricity generation, and residential utilization.

Because of its simple atomic structure, hydrogen has high reactivity with other elements [10]. Thus, most hydrogen exist in the form of chemical compounds like water, fossil fuels, and biomass. Accordingly, many technologies has been employed to produce hydrogen from diverse resources. Hydrogen production methods can be classified into three major categories: thermal, electrolytic, and photolytic processes [11].

- Thermal processes convert hydrogen containing materials (fossil fuels and biomass) into hydrogen with thermal methods. 95% of current world hydrogen is produced by thermal processes including natural gas reforming (48%), partial oxidation of refinery oil (30%), and coal gasification (17%).
- Water electrolysis process uses an electrical current passing through two electrodes to break water into hydrogen and oxygen. 5% of world hydrogen production is based on water electrolysis. Electrolysis can be classified into three types according to its cell: alkaline based electrolysis, proton exchange membrane (PEM), and solid oxide electrolysis cells (SOEC).
- Photolytic process uses a sunlight energy to split water into hydrogen and oxygen. Photolytic process includes photo-electrochemical water splitting and photo-biological water splitting. Although photolytic

process is environmentally friendly, it is longer-term technology.

Currently, most hydrogen production is based on LNG (liquefied natural gas) reforming process which is still based on non-renewable fossil fuel system [12]. Therefore, development of hydrogen production technology using renewable source is required to attain sustainability and fuel flexibility.

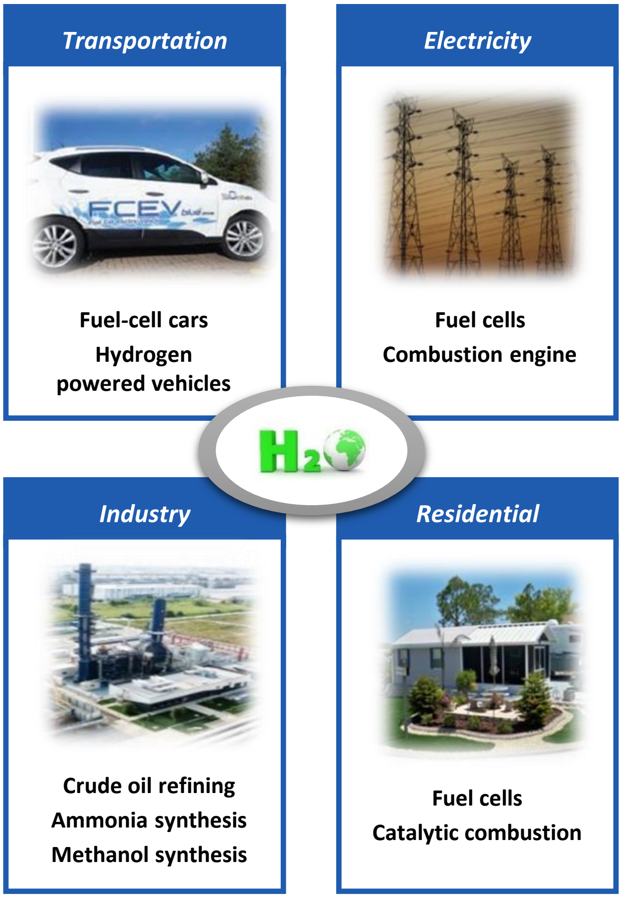

Fig. 1.1. Various applications of hydrogen.

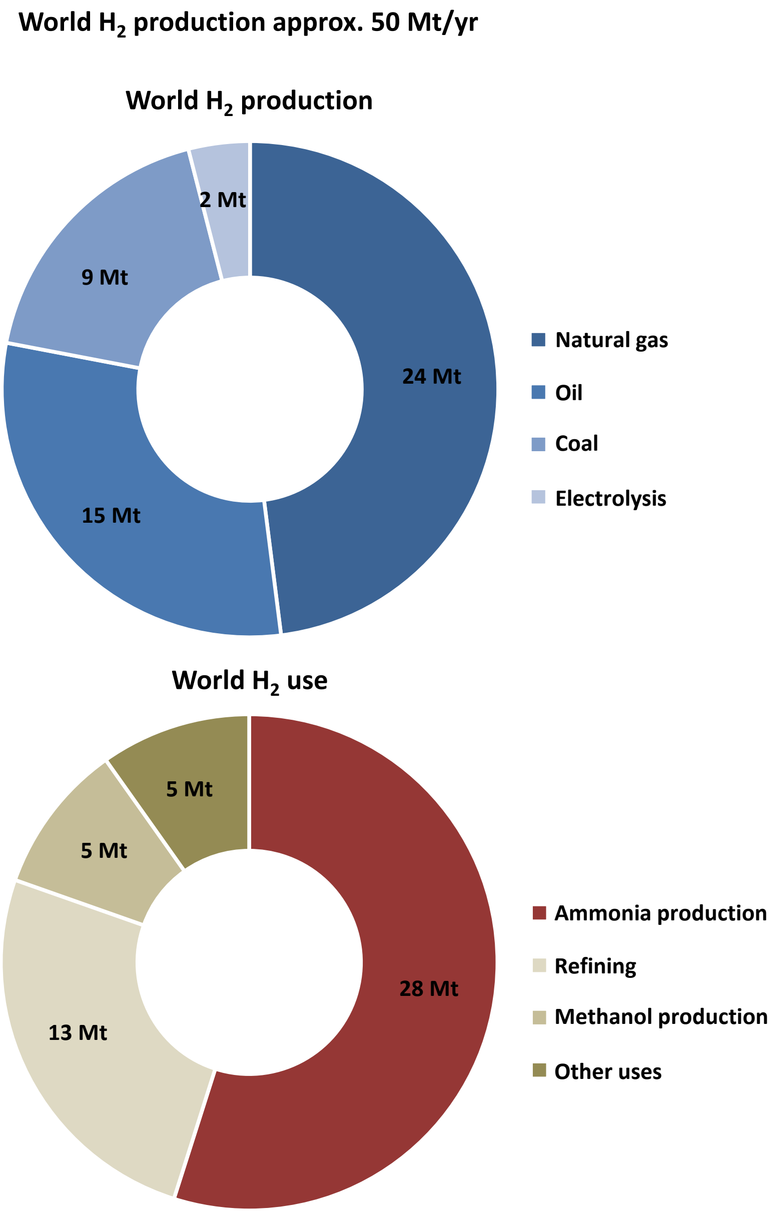

Fig. 1.2. Estimated world hydrogen production and utilization (2008) [13].

1.3. Steam reforming of ethanol

Hydrogen can be produced from hydrocarbon fuels via reforming processes. Reforming processes can be classified into three primary processes: steam reforming, autothermal reforming, and partial oxidation [14]. Among them, steam reforming process is the most promising process showing the highest hydrogen production efficiency. Although natural gas is the most common source for hydrogen production by steam reforming process, bio-liquid is an attractive candidate as a hydrogen source. Bio-liquid is considered as an environmentally friendly resource because CO_2 emitted from bio-liquid is recycled for the growth of biomass in a closed ecology system. Among the bio-liquid, ethanol is expected to be most viable source for hydrogen production in the near future due to its non-toxicity, storage facility, and biodegradable nature [15,16]. As a consequence, ethanol steam reforming is a promising technology for hydrogen production which can mitigate environmental problems in the future.

Thermodynamics and reaction mechanisms of ethanol steam reforming have been extensively studied [17]. Ideal reaction of ethanol steam reforming (Equation 1.1) is endothermic reaction and it only produces H_2 and CO_2. However, ethanol steam reforming in practice comprises many side reactions such as dehydrogenation of ethanol (Equation 1.2), decomposition of ethanol (Equation 1.3), dehydration of ethanol (Equation 1.4), methanation (Equation 1.5), methane steam reforming (Equation 1.6), boudouard reaction (Equation 1.7), and water gas shift reaction (Equation 1.8).

$$C_2H_5OH + 3H_2O \rightarrow 2CO_2 + 6H_2 \quad (\Delta H^o_{298\,K} = 174\ kJ/mol) \qquad (1.1)$$

$$C_2H_5OH \leftrightarrow C_2H_4O + H_2 \quad (\Delta H^o_{298\,K} = 68\ kJ/mol) \qquad (1.2)$$

$$C_2H_5OH \leftrightarrow CH_4 + CO + H_2 \quad (\Delta H^o_{298\,K} = 49\ kJ/mol) \qquad (1.3)$$

$$C_2H_5OH \leftrightarrow C_2H_4 + H_2O \quad (\Delta H^o_{298\,K} = 45\ kJ/mol) \qquad (1.4)$$

$$CO + 3H_2 \leftrightarrow CH_4 + H_2O \quad (\Delta H^o_{298\,K} = -251\ kJ/mol) \qquad (1.5)$$

$$CH_4 + H_2O \leftrightarrow CO + 3H_2 \quad (\Delta H^o_{298\,K} = 206.2\ kJ/mol) \qquad (1.6)$$

$$2CO \leftrightarrow CO_2 + C \quad (\Delta H^o_{298\,K} = -171.5\ kJ/mol) \qquad (1.7)$$

$$CO + H_2O \leftrightarrow CO_2 + H_2 \quad (\Delta H^o_{298\,K} = -41.2\ kJ/mol) \qquad (1.8)$$

Ethanol dehydrogenation reaction followed by acetaldehyde steam reforming is known to be a major reaction pathway of ethanol steam reforming [14,18]. Additional water gas shift reaction reduces coke formation and enhances hydrogen production. On the other hand, dehydration and decomposition of ethanol are undesired reactions which lead to coke formation [14]. Therefore, it is important to develop a catalyst which suppresses undesired reactions to improve hydrogen production in the steam reforming of ethanol.

For steam reforming of ethanol, nickel-based catalyst has been widely used as a non-noble metal catalyst due to its low cost and high activity in C-C cleavage reaction [19,20]. However, nickel-based catalyst is vulnerable to sintering and coking during steam reforming of ethanol, resulting in a catalyst deactivation [21]. Therefore, developing an efficient nickel-based steam reforming catalyst with high catalytic activity and durability is of great importance.

There have been many attempts to improve the physicochemical properties of nickel-based catalysts in order to achieve high catalytic performance in ethanol steam reforming.

- It is known that strong acidic property of Al_2O_3 promotes ethanol dehydration to ethylene, which causes coke formation on the catalyst surface. Therefore, many attempts have been made to neutralize Ni/Al_2O_3 catalyst by addition of alkaline earth metals. Alkaline earth metal oxides such as MgO and CaO have been used as additives for Ni/Al_2O_3 and catalytic stability was enhanced [16].
- ZrO_2 was introduced into Ni/Al_2O_3 catalysts to improve the catalytic activity, because ZrO_2 not only enhances the stability of the catalyst but also promotes adsorption and dissociation of water on the surface of nickel catalyst. It has been reported that $Ni\text{-}Al_2O_3\text{-}ZrO_2$ catalyst with optimal amount of ZrO_2 showed high and stable catalytic activity in the steam reforming of ethanol compared to Ni/Al_2O_3 catalyst [22-24].
- A nickel catalyst supported on $La_2O_3\text{-}Al_2O_3$, $MgO\text{-}Al_2O_3$, and $CeO_2\text{-}Al_2O_3$ exhibited high and stable catalytic performance in steam reforming of ethanol. La and Ce additives were found to inhibit the coke formation on nickel surfaces during steam reforming of ethanol [20].
- Addition of strontium onto Ni/Al_2O_3 catalyst reduced support acidity

and increased selectivity toward hydrogen. It has been reported that optimal amount of strontium was required for high and stable catalytic activity in steam reforming of ethanol [25].

- Copper was also used as promoter of nickel catalyst in steam reforming. Addition of copper increased catalytic stability in steam reforming of ethanol [26-28].
- Textural modification of supported nickel catalysts has also been attempted in order to achieve high catalytic performance in the steam reforming reaction. It has been reported that xerogel-based nickel catalysts exhibited a strong resistance toward coke deposition and nickel sintering due to their well-developed mesoporous structure [29,30].
- Gel-derived materials with improved physicochemical properties called aerogels exhibited high catalytic activity and durability compared to xerogels in steam reforming of ethanol [31-33].
- Surfactants, which contain a hydrophilic head group and a long hydrophobic tail group, have been widely used for soft-templating method to prepare mesoporous structured catalysts in steam reforming of ethanol [34-36].
- Ordered mesoporous alumina support has been employed for nickel catalyst in order to mitigate mass transfer limitation of reactants and to enhance nickel dispersion of catalyst [37-39].
- Supported Ni-Co bimetallic catalyst have also been employed to steam reforming of ethanol, and they showed the enhanced catalytic activity

and high coke resistance [40].

- Abelló et al also employed Ni-Fe bimetallic catalysts to steam reforming of ethanol and they exhibited higher activities than single metallic catalysts. Synergetic effect of Ni and Fe on catalytic activity was also investigated [41].
- Multifunctional catalysts with high catalytic activity and CO_2 sorption property have been studied. In particular, hydrotalcite and Ca-based sorbents have been used in sorption-enhanced steam reforming of ethanol [42,43].

Table 1.2

Reforming technologies for hydrogen production from ethanol

Process	Equation	Characteristics
Steam reforming	$C_2H_5OH + 3H_2O \leftrightarrow 2CO_2 + 6H_2$	• Endothermic • Simple and most extensive • High H_2/CO ratio (= 3) • No oxygen is required • Applicable to high pressure process • Suitable for hydrogen production
Auto-thermal reforming	$C_2H_5OH + 2H_2O + 0.25O_2 \leftrightarrow 2CO_2 + 5H_2$	• Limited commercial experience • Oxygen supply facility is required • High energy efficiency
Partial oxidation	$C_2H_5OH + 0.5O_2 \leftrightarrow 2CO + 3H_2$	• Exothermic • Oxygen supply facility is required • Low reliability for large volume processing • Low stability due to hot-spot generation
CO_2 reforming (dry reforming)	$C_2H_5OH + CO_2 \leftrightarrow 3CO + 3H_2$	• Endothermic • Use of greenhouse gas (CO_2) • Low efficiency • Severe catalyst deactivation due to coking • Hard to be commercialized

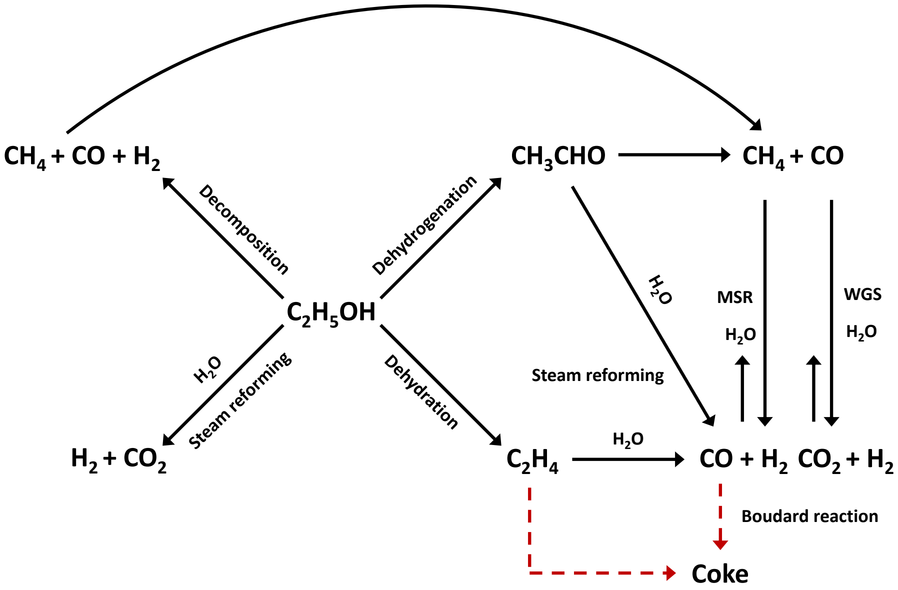

Fig. 1.3. Reaction mechanism of ethanol steam reforming.

1.4. Objective

Conventionally, nickel catalysts supported on alumina (Ni/Al_2O_3) have been widely used in the steam reforming of ethanol due to their high dehydrogenation activity and low cost [44,45]. However, it is known that Ni/Al_2O_3 catalysts suffer from significant deactivation caused by carbon deposition on their acid sites during the ethanol steam reforming reaction [46]. For this reason, many attempts have been made to increase both catalytic activity and durability of Ni/Al_2O_3 catalysts through modifications of catalyst such as zirconium addition, optimization of catalyst composition, and copper addition. Also, various preparation methods such as epoxide-driven sol-gel method, supercritical drying, and soft templating were employed to improve physicochemical properties of catalyst. Textural properties, crystalline structure, metal-support interaction, acid-base property, and nickel dispersion could be tuned by these methods, resulting in the enhanced catalytic performance in the steam reforming of ethanol. Also, ethanol adsorption-desorption behavior was studied to understand reaction mechanism of ethanol steam reforming and to measure the ethanol adsorption capacity of catalyst. In this work, therefore, modifications of mesoporous nickel-alumina catalysts have been attempted to enhance catalytic activity and durability in the steam reforming of ethanol. Then the effect of catalyst physicochemical properties and reaction parameters on catalytic performance in the steam reforming of ethanol was investigated.

It is known that acid sites of alumina support promote dehydration of ethanol to ethylene, resulting in coke formation. Therefore, neutralization of alumina support is required to achieve coke resistance in steam reforming of ethanol. Among various metal oxides, ZrO_2 is known to be the most effective additive for Ni/Al_2O_3 catalysts in steam reforming of ethanol, because ZrO_2 can not only enhance the stability of the catalysts but also promote adsorption and dissociation of water on the surface of nickel catalyst. In this point of view, a systematic investigation on optimizing ZrO_2 addition to $Ni-Al_2O_3$ xerogel catalyst for hydrogen production by steam reforming of ethanol would be worthwhile.

The property of active metal is also an important factor determining the catalytic performance in the steam reforming reactions. It has been reported that nickel surface area is intimately related to both reducibility and coking resistance in the steam reforming reactions [47,48]. Therefore, a systematic investigation on the effect of nickel surface area by optimizing nickel content of $Ni-Al_2O_3-ZrO_2$ xerogel catalyst on hydrogen production by steam reforming of ethanol was carried out.

Xerogel-based nickel catalysts prepared by a sol-gel method and a subsequent conventional drying method have attracted much attention due to their well-developed mesoporous structure [29,30]. However it is known that conventional drying of gel structure results in the formation of crumbled masses of gel material [49,50]. Because this disruption of gel structure is caused by large liquid-vapor interfacial forces, it is necessary to avoid a liquid-to-vapor phase transition in order to improve physicochemical properties of sol-gel- derived materials. To avoid a liquid-to-vapor phase transition during drying process, supercritical drying has been employed

[51,52]. Gel-derived materials with improved physicochemical properties called aerogels can be obtained by supercritical drying [53]. Therefore, a systematic investigation on the application of aerogel-based catalyst to hydrogen production by steam reforming of ethanol was conducted. The effect of drying method on the physicochemical properties and catalytic activities of Ni-AZ and Ni/AZ catalysts in the steam reforming of ethanol was investigated.

There have been many attempts to enhance textural properties of the catalysts by employing templating method. In particular, surfactants, which contain a hydrophilic head group and a long hydrophobic tail group, have been widely used for soft-templating method to prepare mesoporous materials [34-36]. Since the synthesis of supramolecular-templated mesoporous materials such as MCM-41 and M41S [54,55], ordered mesoporous alumina has been successfully prepared by evaporation induced self-assembly (EISA) method using P123 as a surfactant material [56]. Although surfactant does not build micelle in ethanol medium because of its low polarity, surfactant in the epoxide-driven sol-gel method can improve physicochemical properties by working as a soft template [57]. Therefore, a systematic investigation on the effect of P123 addition on the catalytic activities and physicochemical properties of mesoporous Ni-Al_2O_3-ZrO_2 prepared by a epoxide-driven sol-gel method would be worthwhile. The effect of P123 concentration on the physicochemical properties and catalytic activities in the steam reforming of ethanol was investigated.

Cu-based catalyst is known to have poor catalytic activity in the steam reforming of ethanol [58]. However, addition of copper to nickel-based catalyst can induce synergetic effect by enhancing dehydrogenation activity and reducibility of the catalyst [26-28]. Therefore, a systematic investigation on the effect of copper addition on the catalytic activity and physicochemical property of copper-nickel-alumina-zirconia catalyst was performed. The effect of Cu content on the physicochemical properties and catalytic activities of mesoporous XCNAZ catalysts in the steam reforming of ethanol was investigated.

Chapter 2. Experimental

2.1. Preparation of catalysts

2.1.1. Preparation of mesoporous nickel-alumina-zirconia xerogel catalyst with various zirconium/aluminum molar ratio

A series of mesoporous Ni-Al_2O_3-ZrO_2 xerogel catalysts with different Zr/Al molar ratio were prepared by a single-step epoxide-driven sol-gel method, according to the similar methods reported in the literatures [59,60]. Known amounts of aluminum precursor (aluminum nitrate nonahydrate, Sigma-Aldrich, 98%) and zirconium precursor (zirconium oxynitrate hydrate, Sigma-Aldrich, 99%) were dissolved in ethanol (58 ml). The total amount of two precursors was 0.04 mol. An appropriate amount of nickel precursor (nickel nitrate hexahydrate, Sigma-Aldrich, 97%) was then dissolved in the solution containing aluminum and zirconium precursors with vigorous stirring. Propylene oxide (29 ml) as a gelation agent was then added into the resulting solution. Upon maintaining the solution for a few minutes, deprotonation of hydrated metal salts and subsequent cross-linking of metal ion complex occurred for the formation of Ni-Al_2O_3-ZrO_2 composite gel. After the gel was aged for 2 days, it was washed with ethanol two times in order to minimize the destruction of pore structure of the catalyst by removing foreign substances in the gel with ethanol. The product was then dried at 80 ^{o}C in a convection oven for 5 days. The resulting powder was finally calcined at 550 ^{o}C for 5 h to obtain a mesoporous Ni-Al_2O_3-ZrO_2 xerogel catalyst. The prepared mesoporous Ni-Al_2O_3-ZrO_2 xerogel catalysts were denoted as Ni-AZ-X (X = 0, 0.1, 0.2, 0.3, and 0.4), where X represented Zr/Al molar ratio. Nickel loading of Ni-AZ-X catalysts was fixed at 10 wt%.

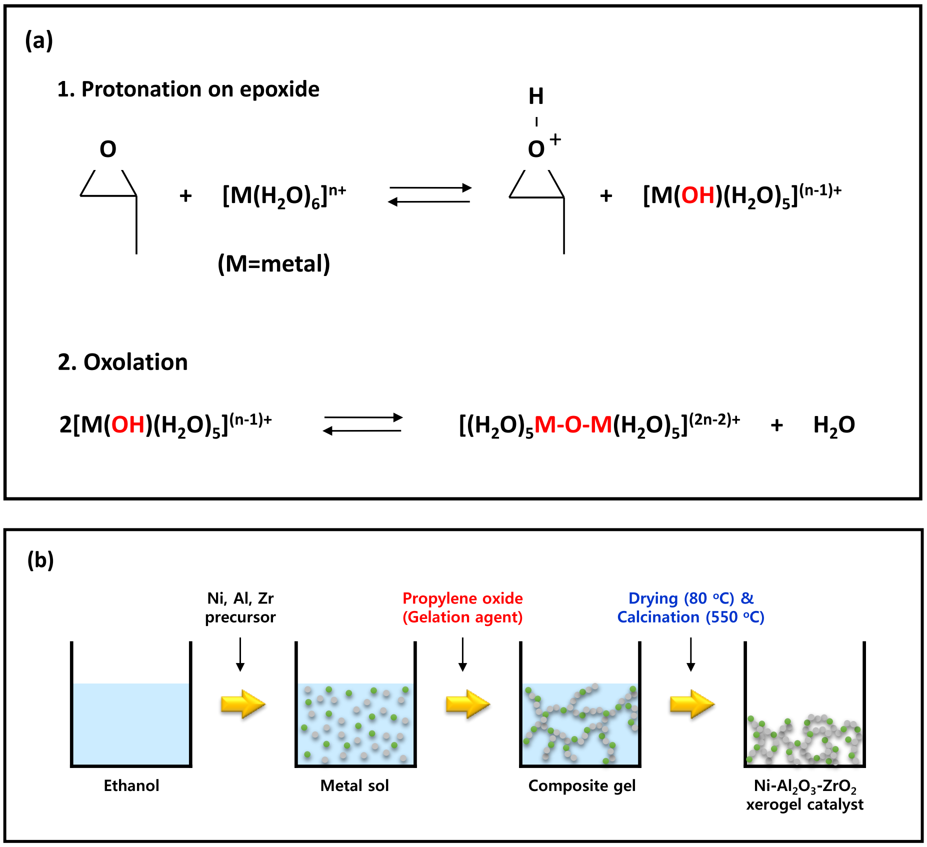

Fig. 2.1. (a) Reactions involved in the preparation of metal oxide by an epoxide-driven sol-gel method and (b) schematic procedures for the preparation of $Ni\text{-}Al_2O_3\text{-}ZrO_2$ xerogel catalyst by an epoxide-driven sol-gel method.

2.1.2. Preparation of mesoporous nickel-alumina-zirconia xerogel catalyst with various nickel content

A set of mesoporous Ni-Al_2O_3-ZrO_2 xerogel catalysts with different nickel content were prepared by a single-step epoxide-driven sol-gel method as previously reported in the literatures [59,60]. 12.4 g of aluminum precursor (aluminum nitrate nonahydrate, Sigma-Aldrich, 98%) and 1.6 g of zirconium precursor (zirconium oxynitrate hydrate, Sigma-Aldrich, 99%) were dissolved in ethanol (54, 58, 62, 66, and 70 ml). In order to control nickel content, an appropriate amount of nickel precursor (nickel nitrate hexahydrate, Sigma-Aldrich, 97%) was dissolved in the solution containing aluminum and zirconium precursors. The solution was vigorously stirred at room temperature, and then a known amount of propylene oxide was added into the solution for gelation. After maintaining the resulting solution for a few minutes, Ni-Al_2O_3-ZrO_2 composite gel was obtained [61,62]. The gel was aged for 2 days in order to obtain composite gel with uniform density, and subsequently, it was washed with ethanol two times. The obtained gel was kept at 80 ^oC in a convection oven for 3 days. The resulting powder was finally calcined at 550 ^oC for 5 h at a heating rate of 5 ^oC/min. The prepared mesoporous Ni-Al_2O_3-ZrO_2 xerogel catalysts were denoted as XNiAZ (X = 5, 10, 15, 20, and 25), where X represented nickel content (wt%). Zr/Al molar ratio was fixed at 0.2 in all the catalysts [63].

2.1.3. Preparation of nickel-alumina-zirconia aerogel catalyst by carbon dioxide supercritical drying

A mesoporous Ni-Al_2O_3-ZrO_2 aerogel (denoted as Ni-AZ) catalyst was prepared by a single-step epoxide-driven sol-gel method and a subsequent supercritical CO_2 drying method [33]. 6.00 g of aluminum precursor (aluminum nitrate nonahydrate, Sigma-Aldrich, 98%), 0.93 g of zirconium precursor (zirconium oxynitrate hydrate, Sigma-Aldrich, 99%), and 1.14 g of nickel precursor (nickel nitrate hexahydrate, Sigma-Aldrich, 97%) were dissolved in ethanol (30 ml). The resulting solution was vigorously stirred at room temperature to obtain a homogeneous solution. Propylene oxide (14.7 ml) was then added into the solution for gelation. After a few minutes, a homogeneous gel was obtained. The obtained gel was aged for 2 days and washed with ethanol. The solvent in the gel matrix was exchanged with carbon dioxide at 20 ^{o}C and 100 atm for 4 h in a stream of liquid carbon dioxide. After eliminating ethanol in the gel, it was dried at 50 ^{o}C and 100 atm for 2 h in a stream of supercritical carbon dioxide. The resulting solid was calcined at 550 ^{o}C for 5 h to obtain a mesoporous Ni-Al_2O_3-ZrO_2 (denoted as Ni-AZ) catalyst. Ni content in the Ni-AZ catalyst was fixed at 15 wt%.

For comparison, a mesoporous Ni/Al_2O_3-ZrO_2 (denoted as Ni/AZ) catalyst was prepared by an incipient wetness impregnation method [64]. After preparing Al_2O_3-ZrO_2 aerogel (denoted as AZ) support by an epoxide-driven sol-gel method and a subsequent supercritical CO_2 drying method, Ni/AZ catalyst was obtained by an incipient wetness impregnation method.

6.00 g of aluminum precursor (aluminum nitrate nonahydrate, Sigma-Aldrich, 98%) and 0.93 g of zirconium precursor (zirconium oxynitrate hydrate, Sigma-Aldrich, 99%) were dissolved in ethanol (25 ml). The resulting solution was vigorously stirred at room temperature to obtain a homogeneous solution. Propylene oxide (12.3 ml) was then added into the solution for gelation. After aging and washing processes, the solvent in the gel matrix was exchanged with carbon dioxide at 20 ^{o}C and 100 atm for 4 h in a stream of liquid carbon dioxide. It was then dried at 50 ^{o}C and 100 atm for 2 h in a stream of supercritical carbon dioxide. The resulting solid was calcined at 550 ^{o}C for 5 h to obtain a mesoporous Al_2O_3-ZrO_2 support. 1 g of Al_2O_3-ZrO_2 aerogel support was impregnated with an ethanol solution (5 ml) containing 0.87 g of nickel precursor (nickel nitrate hexahydrate, Sigma-Aldrich, 97%). After the incipient wetness impregnation, the resulting powder was dried at 80 ^{o}C for a day. The resulting solid was finally calcined at 550 ^{o}C for 5 h to obtain a mesoporous Ni/AZ catalyst. Ni content in the Ni/AZ catalyst was fixed at 15 wt%.

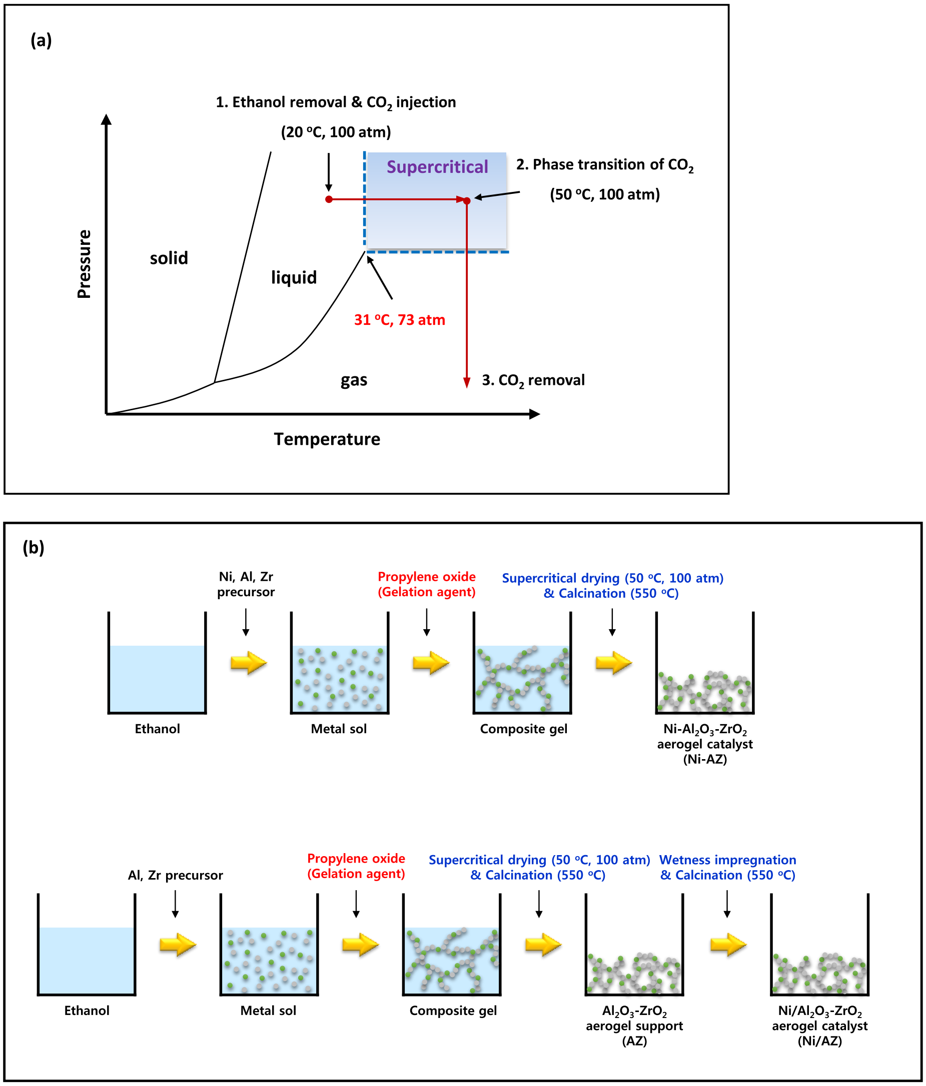

Fig. 2.2. (a) CO$_2$ supercritical drying process expressed on phase diagram and (b) schematic procedures for the preparation of Ni-AZ and Ni/AZ aerogel catalysts.

2.1.4. Preparation of mesoporous nickel-alumina-zirconia xerogel catalyst by P123-assisted sol-gel method

A series of mesoporous Ni-Al_2O_3-ZrO_2 xerogel catalysts were prepared by a P123-assisted epoxide-driven sol-gel method. P123 (Pluronic P123, Sigma-Aldrich) solution with different concentration was prepared by dissolving an appropriate amount of P123 in ethanol (29 ml). To obtain clear P123 solution, 4 ml of hydrochloric acid (hydrochloric acid, Sigma-Aldrich, 36%) was added into the solution. 6.00 g of aluminum precursor (aluminum nitrate nonahydrate, Sigma-Aldrich, 98%), 0.93 g of zirconium precursor (zirconium oxynitrate hydrate, Sigma-Aldrich, 99%), and 1.14 g of nickel precursor (nickel nitrate hexahydrate, Sigma-Aldrich, 97%) were dissolved in the acidic solution containing P123. The homogeneous solution was obtained by vigorous stirring at room temperature. 14 ml of propylene oxide, proton scavenger in the epoxide-driven sol-gel method, was then added into the solution. After maintaining the solution for a few minutes, Ni-Al_2O_3-ZrO_2 composite gel was obtained. The gel was aged for 2 days and it was dried at 80 ^{o}C for 5 days. The resulting solid was calcined at 550 ^{o}C for 5 h to obtain a mesoporous Ni-Al_2O_3-ZrO_2 xerogel catalyst. The prepared P123-assisted mesoporous Ni-Al_2O_3-ZrO_2 xerogel catalysts were denoted as X-NAZ (X = 0, 6, 12, 18, and 24), where X represented P123 concentration (mM). Ni content was fixed at 15 wt% and Zr/Al molar ratio was fixed at 0.2 in all the catalysts.

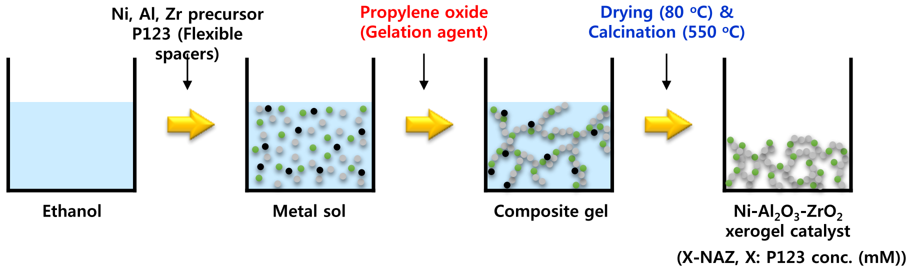

Fig. 2.3. Schematic procedures for the preparation of X-NAZ xerogel catalysts by P123-assisted sol-gel method.

2.1.5. Preparation of mesoporous copper-nickel-alumina-zirconia xerogel catalyst with various copper content

A series of mesoporous Cu-Ni-Al_2O_3-ZrO_2 xerogel catalysts were prepared by a single-step epoxide-driven sol-gel method. 0.93 g of zirconium precursor (zirconium oxynitrate hydrate, Sigma-Aldrich, 99%) was dissolved in ethanol (29 ml), and 3 ml of hydrochloric acid (hydrochloric acid, Samchun, 35-37%) was added into the solution. 6.00 g of aluminum precursor (aluminum nitrate nonahydrate, Sigma-Aldrich, 98%), 0.97 g of nickel precursor (nickel nitrate hexahydrate, Sigma-Aldrich, 97%), and an appropriate amount of copper precursor (copper nitrate hydrate, Sigma-Aldrich, 98%) were simultaneously dissolved in the solution. A homogeneous solution was obtained by vigorous stirring at room temperature. 14 ml of propylene oxide was then added into the solution for gelation. After a few minutes, Cu-Ni-Al_2O_3-ZrO_2 composite gel was formed. The gel was aged for 2 days and it was dried at 80 ^{o}C for 5 days. The resulting solid was calcined at 550 ^{o}C for 5 h at a heating rate of 5 ^{o}C/min. The prepared Cu-Ni-Al_2O_3-ZrO_2 xerogel catalysts were denoted as XCNAZ (X = 0, 0.1, 0.2, 0.3, and 1.0), where X represented Cu content (wt%). Ni content was fixed at 15 wt% and Zr/Al molar ratio was fixed at 0.2 in all the catalysts.

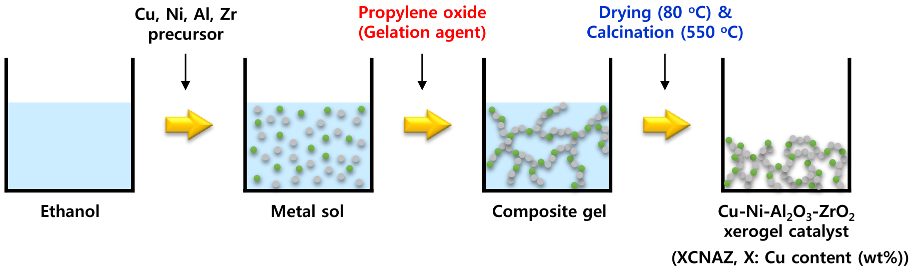

Fig. 2.4. Schematic procedures for the preparation of XCNAZ xerogel catalysts by epoxide-driven sol-gel method.

2.2. Characterization

2.2.1. Physicochemical properties

Chemical compositions of the calcined catalysts were measured by inductively coupled plasma atomic emission spectroscopy using ICPS-100IV (Shimadzu).

Textural properties of the calcined catalysts were measured by N_2 adsorption-desorption experiments at 77 K using a BELSORP-mini II (BEL Japan) apparatus. Prior to the measurements, the catalysts were degassed at 150 ^oC for 6 h for removal of moisture and other adsorbed gases on the surface. The Brunauer-Emmett-Teller (BET) equation was used to calculate surface area of the catalysts. Pore volume and pore diameter of catalyst were calculated by the BJH (Barret-Joyner-Hallender) method.

2.2.2. Crystalline structure

Crystalline structures of calcined and reduced catalysts were determined by XRD measurements with a D-Max2500-PC (Rigaku) instrument using Cu-Kα radiation (λ = 1.541 Å) operated at 50 kV and 100 mA. For the XRD measurements of reduced catalysts, 0.1 g of each catalyst was reduced with a mixed stream of H_2 (3 ml/min) and N_2 (30 ml/min).

2.2.3. Metal-support interaction

Metal-support interaction of the catalysts was evaluated by conducting temperature-programmed reduction (TPR) experiments. For the TPR experiments, 100 mg of catalyst sample was loaded in a quartz reactor and it was reduced with a mixed stream of H_2 (2 ml/min) and N_2 (20 ml/min) at temperatures ranging from room temperature to 1000 ^oC with a ramping rate of 5 ^oC/min. H_2 consumption rate of the catalysts was measured by thermal conductivity detector (TCD).

X-ray photoelectron spectroscopy (XPS) analyses were conducted to determine the binding energies of nickel species in the calcined catalysts using an AXIS-HSi (KRATOS) apparatus. All the spectra were calibrated taking C 1s peak at 284.5 eV as a reference.

2.2.4. Acid property

NH_3-TPD experiments were conducted to determine the acid property of reduced catalysts (BELCAT-B, BEL Japan). 0.07 g of each catalyst charged into the TPD apparatus was reduced with a mixed stream of H_2 (2.5 ml/min) and Ar (47.5 ml/min). After cooling the catalyst to room temperature, a mixed stream of NH_3 (2.5 ml/min) and He (47.5 ml/min) was introduced into the reactor at 50 ^oC for 50 min to saturate acid sites of the catalyst. Physisorbed ammonia was removed at 100 ^oC for 1 h under a flow of He (50 ml/min). After cooling the sample, furnace temperature was increased from 50 ^oC to 900 ^oC at a heating rate of 5 ^oC/min under a flow of He (30 ml/min). The desorbed ammonia was detected using a TCD (thermal conductivity detector).

2.2.5. Morphological feature

Morphologies of reduced catalysts were examined by transmission electron microscopy (TEM) analyses (JEM-2000EXII, Jeol). For the TEM analyses of reduced catalysts, ex-situ reduction with a mixed stream of H_2 (3 ml/min) and N_2 (30 ml/min) was preliminarily conducted.

Dispersion of metal species on the reduced catalysts was examined by TEM-EDX analyses (Tecnai F20, FEI). Prior to the TEM analyses, each catalyst was preliminarily reduced.

2.2.6. Hydrogen chemisorption studies

Nickel surface area was determined from the amount of hydrogen chemisorption using a dynamic flow technique (BELCAT-B, BEL Japan). Prior to each measurement, 50 mg of calcined catalyst was loaded and reduced with a mixed stream of hydrogen (2.5 ml/min) and argon (47.5 ml/min). It was then purged with pure argon (50 ml/min) for 15 min and cooled to 50 ^{o}C under a flow of argon (50 ml/min). The amount of hydrogen chemisorption was measured by periodically injecting diluted hydrogen (5% hydrogen and 95% argon) into the reduced catalyst using an on-line sampling valve. To calculate nickel surface area, adsorption stoichiometry of H/Ni = 1 was assumed. Cross-sectional area of atomic nickel was also assumed to be

6.49×10^{-20} m^2/Ni-atom.

H_2 temperature-programmed desorption (H_2-TPD) measurements were conducted to measure the amount of hydrogen uptake and hydrogen-binding strength on the surface of reduced catalysts using a BELCAT-B (BEL Japan) apparatus equipped with a thermal conductivity detector (TCD). Prior to the hydrogen adsorption, 50 mg of catalyst sample was loaded into the TPD apparatus and it was preliminarily reduced with a mixed stream of hydrogen (2.5 ml/min) and argon (47.5 ml/min). It was purged for 10 min and cooled to 50 ^{o}C under pure argon flow (50 ml/min). The reduced catalyst was saturated with hydrogen (5% hydrogen and 95% argon) at 50 ^{o}C for 30 min. Physisorbed hydrogen was removed under argon flow (50 ml/min) at 100 ^{o}C for 1 h. The sample was then heated to 1000 ^{o}C with a heating rate of 5 ^{o}C/min under argon flow (30 ml/min), and the amount of H_2 desorbed was measured by a thermal conductivity detector (TCD). Adsorption stoichiometry of H/Ni = 1 and atomic cross-sectional area of 6.49×10^{-20} m^2/Ni-atom were assumed to calculate active nickel surface areas of reduced catalysts.

2.2.7. Ethanol adsorption-desorption studies

Ethanol adsorption-desorption behavior of the catalysts was investigated by EtOH-TPD experiments. For the experiment, reduction of each catalyst was conducted under a mixed flow of H_2 (3 ml/min) and He (30 ml/min). After cooling the sample to 50 ^{o}C, 10 ml of ethanol vapor (49.7% ethanol and 50.3% helium) was pulsed into the reactor every minute with a stream of helium (5 ml/min) until the active sites were saturated with ethanol. To remove the physisorbed ethanol, the sample was purged in a vacuum at 100 ^{o}C for 1 h under a He flow (15 ml/min). The furnace temperature was then increased to 800 ^{o}C with a heating rate of 10 ^{o}C/min under a He flow (10 ml/min). The desorbed ethanol and carbon-containing species were detected using a GC-MSD (6890N GC-5975MSD, Agilent).

In-situ infrared spectroscopy analyses of adsorbed ethanol were conducted to study ethanol adsorption-desorption behavior with a Fourier transform infrared (FT-IR) spectrometer (Thermo Scientific, Nicolet 6700). Prior to the analyses, the catalyst sample was reduced under a mixed flow of hydrogen (2 ml/min) and helium (20 ml/min). 10 ml of vaporized ethanol (49.7% ethanol and 50.3% helium) was then pulsed into the reactor every minute at room temperature under a flow of helium (5 ml/min). Physisorbed ethanol was removed at 100 ^{o}C for 1 h under a flow of helium (20 ml/min), and the spectra were collected at temperatures ranging from 100 ^{o}C to 450 ^{o}C.

2.2.8. Carbon deposition on used catalysts

Crystalline structures of coke on the used catalysts were determined by XRD measurements with a D-Max2500-PC (Rigaku) instrument using Cu-Kα radiation (λ = 1.541 Å) operated at 50 kV and 100 mA.

The amount of carbon deposition on used catalysts after the reaction was determined by CHNS elemental analyses (CHNS 932, Leco).

2.3. Hydrogen production by steam reforming of ethanol

The catalytic evaluation for steam reforming of ethanol was conducted in a continuous flow fixed-bed reactor under atmospheric pressure. Prior to the reaction, 100 mg of catalyst was loaded and reduced under a mixed stream of hydrogen (3 ml/min) and nitrogen (30 ml/min) at the designated temperature. The reactor was purged with nitrogen flow (30 ml/min) for 30 min, and the reactor temperature was fixed at reaction temperature under N_2 flow (30 ml/min). A liquid mixture of ethanol and water with a molar ratio of EtOH:H_2O = 1:6 was constantly fed to the inlet line by a syringe pump (US/KDS-101, KdScientific). The outlet products were analyzed with an online gas chromatograph (ACME 6000, Younglin) equipped with a thermal conductivity detector (TCD). Porapak N and Molecular Sieve 5A columns were used for product separation. Ethanol conversion, hydrogen yield, and selectivity for carbon-containing product were calculated according to the following equations.

$$Ethanol\ conversion\ (\%) = \left(\frac{F_{EtOH,in} - F_{EtOH,out}}{F_{EtOH,in}}\right) \times 100 \qquad (2.1)$$

$$Hydrogen\ yield\ \ (\%) = \frac{F_{H_2,out}}{3 \times (F_{EtOH,in} - F_{EtOH,out})} \times 100 \qquad (2.2)$$

$$S_{i,Carbon-containing\ product}(\%) = \frac{n_i \times F_{i,Carbon-containing\ product}}{2 \times (F_{EtOH,in} - F_{EtOH,out})} \times 100 \qquad (2.3)$$

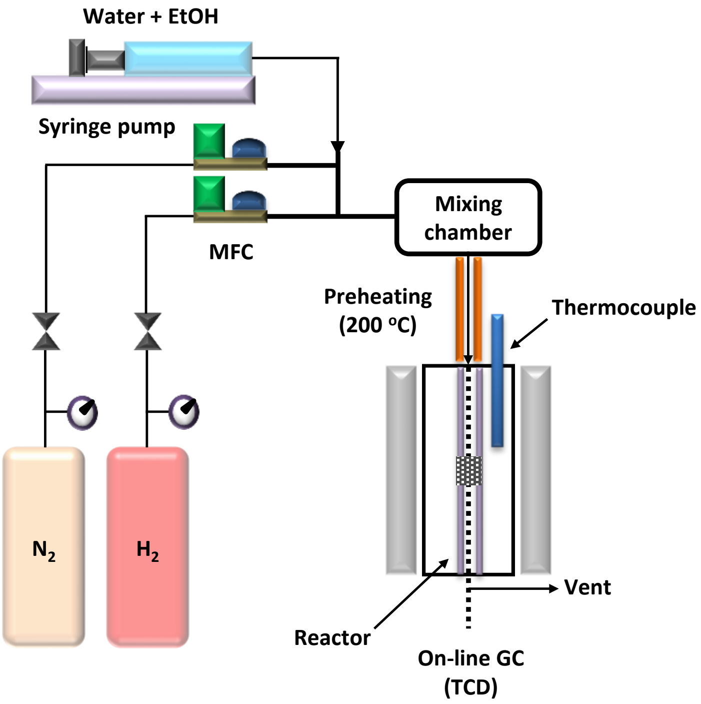

Fig. 2.5. Reaction system for steam reforming of ethanol.

Table 2.1

Steam reforming reaction conditions

	Reduction temperature (^{o}C)	Reaction temperature (^{o}C)	Catalyst weight (mg)	S/C molar ratio	Total flow rate (ml/h·g-cat.)
Section 3.1	550	500	100	3	23,140
Section 3.2	550	500	100	3	28,280
Section 3.3	650	500	100	3	28,280
Section 3.4	650	500	100	3	28,280
Section 3.5	650	450	100	3	28,280

Chapter 3. Results and Discussion

3.1. Mesoporous nickel-alumina-zirconia xerogel catalyst with various zirconium/aluminum molar ratio

3.1.1. Textural properties of calcined catalysts

Textural properties of Ni-AZ-X (X = 0, 0.1, 0.2, 0.3, and 0.4) catalysts were examined by nitrogen adsorption-desorption isotherm measurements as represented in Fig. 3.1. All the Ni-AZ-X catalysts exhibited type-IV isotherms with H2-type hysteresis loops, indicating the presence of well-developed mesopores [65]. Detailed physicochemical properties of Ni-AZ-X (X = 0, 0.1, 0.2, 0.3, and 0.4) catalysts are summarized in Table 3.1. The observed Zr/Al molar ratios of Ni-AZ-X catalysts were quite similar to the designed values. Surface area of Ni-AZ-X catalysts decreased with increasing Zr/Al molar ratio. This might be due to the increased textural density of Ni-AZ-X catalysts caused by the addition of ZrO_2 into Ni-Al_2O_3 composite [66]. The lowest surface area of Ni-AZ-0.4 catalyst could be explained by higher surface energy of Zr^{4+} than Al^{3+}; the coalescence of structure occurred for the minimization of surface energy, resulting in the decrease of surface area [67]. However, pore volume and average pore diameter of Ni-AZ-X catalysts showed no consistent trend with respect to Zr/Al molar ratio.

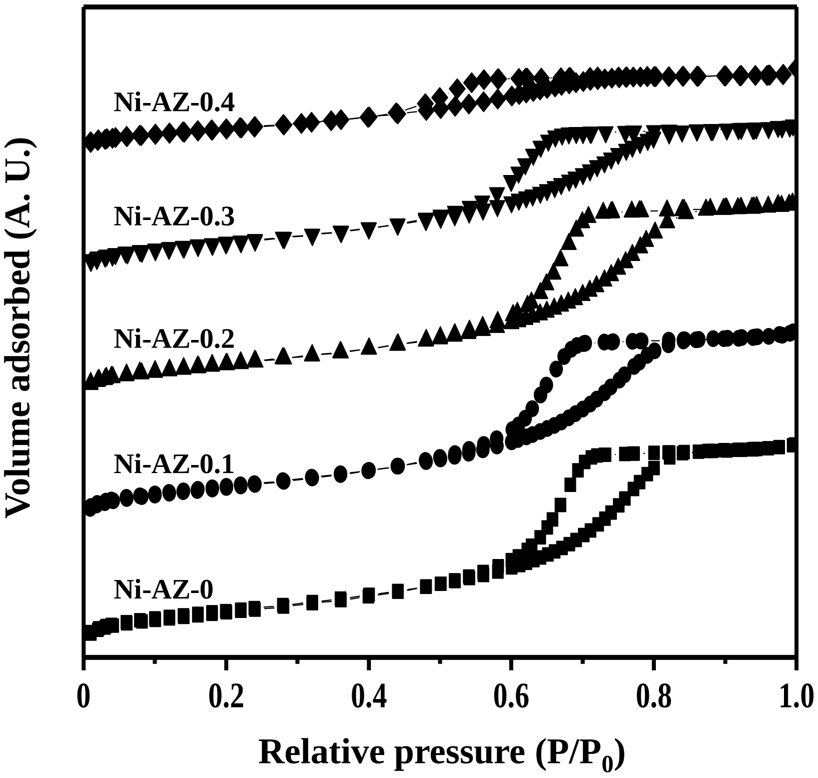

Fig. 3.1. Nitrogen adsorption-desorption isotherms of Ni-AZ-X (X = 0, 0.1, 0.2, 0.3, and 0.4) catalysts calcined at 550 °C.

Table 3.1

Detailed physicochemical properties of Ni-AZ-X catalysts calcined at 550 ^oC for 5 h

Catalyst	Zr/Al molar ratio[a]	Surface area (m^2/g)[b]	Pore volume (cm^3/g)[c]	Average pore diameter (nm)[d]
Ni-AZ-0	0	339	0.66	5.5
Ni-AZ-0.1	0.07	336	0.62	5.3
Ni-AZ-0.2	0.15	320	0.63	5.7
Ni-AZ-0.3	0.25	292	0.49	5.0
Ni-AZ-0.4	0.39	214	0.28	3.9

[a] Determined by ICP-AES measurement

[b] Calculated by the BET equation

[c] BJH desorption pore volume

[d] BJH desorption average pore diameter

3.1.2. Crystalline structures of calcined catalysts

Fig. 3.2 shows the XRD patterns of Ni-AZ-X (X = 0, 0.1, 0.2, 0.3, and 0.4) catalysts calcined at 550 °C. In the Ni-AZ-0 catalyst, three diffraction peaks indicative of $NiAl_2O_4$ phase (solid lines in Fig. 3.2) were observed, as reported in the literatures [68]. However, the peak intensity of $NiAl_2O_4$ gradually decreased with increasing Zr/Al molar ratio. Instead, the diffraction peak of tetragonal ZrO_2 (1 1 1) (dashed line in Fig. 3.2) became strong with increasing Zr/Al molar ratio. It is noticeable that XRD peak of tetragonal ZrO_2 (1 1 1) in the Ni-AZ-X (X = 0.1, 0.2, 0.3, and 0.4) catalysts shifted to the higher diffraction angle than its original angle ($2\theta = 30.2^{\circ}$), representing the lattice contraction of ZrO_2 caused by the incorporation of Al^{3+} ions into ZrO_2. This is because the radius of Zr^{4+} ion (= 0.84 Å) is larger than that of Al^{3+} ion (= 0.54 Å) [69]. Thus, it can be inferred that $NiO-Al_2O_3-ZrO_2$ composite structure was developed in the Ni-AZ-X catalysts by the simultaneous solid-state reaction among NiO, Al_2O_3, and ZrO_2 [70]. Interestingly, diffraction peaks corresponding to NiO (closed circles in Fig. 3.2) suddenly appeared in the Ni-AZ-0.4 catalyst. This is because some Ni^{2+} ions hardly interacted with Al_2O_3 when an excess amount of ZrO_2 was added into the Ni-AZ-X catalysts.

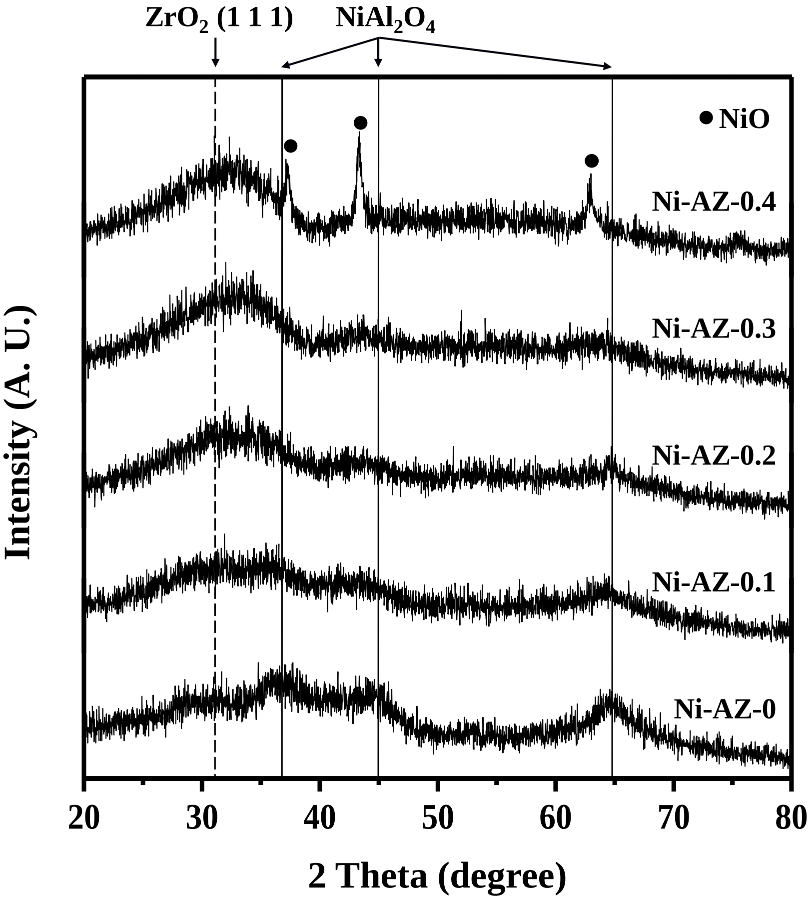

Fig. 3.2. XRD patterns of Ni-AZ-X (X = 0, 0.1, 0.2, 0.3, and 0.4) catalysts calcined at 550 °C.

3.1.3. Reducibility and metal-support interaction

In order to elucidate the metal-support interaction in the Ni-AZ-X (X = 0, 0.1, 0.2, 0.3, and 0.4) catalysts, TPR measurements were carried out as shown in Fig. 3.3. All the catalysts exhibited a reduction band at relatively high temperature within the range of 568-638 ^{o}C. On the other hand, Ni-AZ-X (X = 0.2, 0.3, and 0.4) catalysts showed an additional reduction band at relatively low temperature ranging from 454 ^{o}C to 486 ^{o}C. It has been reported that the band appeared at high temperature is related to the reduction of nickel oxide species strongly interacted with Al_2O_3 [71], while the band appeared at low temperature is associated with the reduction of nickel oxide species weakly interacted with ZrO_2 [72]. It is noticeable that reduction peak temperature of nickel oxide species interacting with Al_2O_3 decreased with increasing Zr/Al molar ratio, while that of nickel oxide species interacting with ZrO_2 increased with increasing Zr/Al molar ratio. In other words, reducibility of nickel oxide species in the Ni-AZ-X catalysts increased with increasing Zr/Al molar ratio. From these results, it can be inferred that the addition of ZrO_2 suppressed the interaction between nickel oxide and support (Al_2O_3 or Al_2O_3-ZrO_2) through the formation of NiO-Al_2O_3-ZrO_2 composite structure.

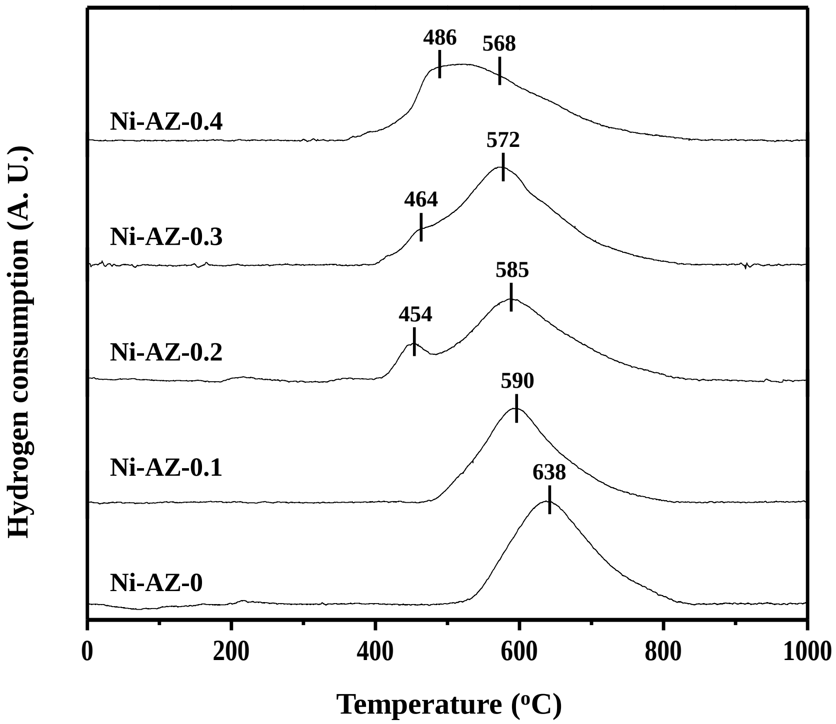

Fig. 3.3. TPR profiles of Ni-AZ-X (X = 0, 0.1, 0.2, 0.3, and 0.4) catalysts calcined at 550 °C.

3.1.4. Characterization of reduced catalysts

Fig. 3.4 shows the XRD patterns of Ni-AZ-X (X = 0, 0.1, 0.2, 0.3, and 0.4) catalysts reduced at 550 ^oC. All the reduced catalysts showed diffraction peaks corresponding to metallic Ni (solid lines in Fig. 3.4). Furthermore, diffraction peaks indicative of NiO and $NiAl_2O_4$ were not observed, indicating that nickel species in all the Ni-AZ-X catalysts were completely reduced into metallic nickel during the reduction process employed in this work.

TEM images of Ni-AZ-0, Ni-AZ-0.2, and Ni-AZ-0.4 reduced at 550 ^oC, and EDX maps with distribution of Ni, Al, and Zr are represented in Fig. 3.5. It was observed that density of Al decreased while that of Zr increased with increasing Zr/Al molar ratio, in accordance with ICP-AES analyses (Table 3.1). It is noteworthy that Al and Zr were homogeneously distributed throughout the catalysts without any significant aggregation regardless of the different Zr/Al molar ratio.

Fig. 3.6 shows the NH_3-TPD profiles of Ni-AZ-X (X = 0, 0.1, 0.2, 0.3, and 0.4) catalysts reduced at 550 ^oC. Acidity of reduced Ni-AZ-X catalysts was calculated from peak area as summarized in Table 3.2. It was observed that acidity of the catalysts monotonically decreased with increasing Zr/Al molar ratio. This can be explained by the fact that acidity of the catalysts is mainly related to Al_2O_3 surface, because large amount of acid sites exists in Al_2O_3 rather than ZrO_2 [73]. This result can also be deduced by the fact that the addition of ZrO_2 decreased surface area of the catalysts (Table 3.1), resulting in the decrease of acid sites of the catalysts [74].

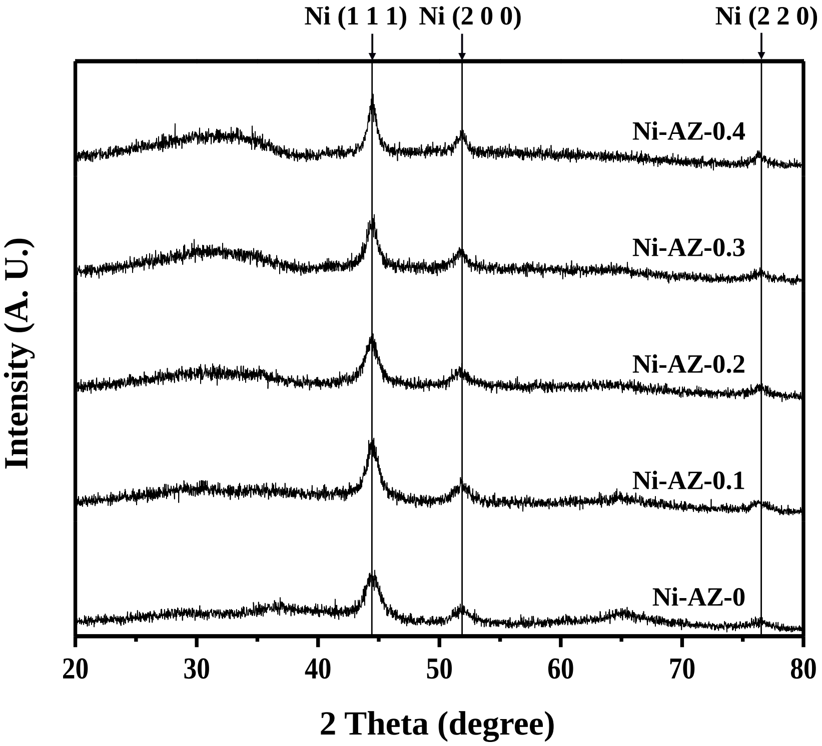

Fig. 3.4. XRD patterns of Ni-AZ-X (X = 0, 0.1, 0.2, 0.3, and 0.4) catalysts reduced at 550 ^{o}C.

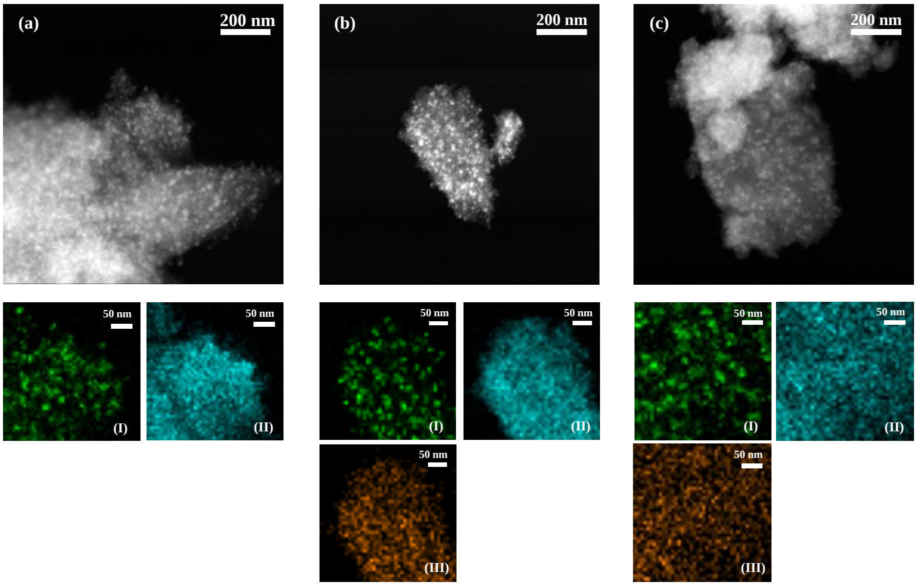

Fig. 3.5. TEM images of (a) Ni-AZ-0, (b) Ni-AZ-0.2, and (c) Ni-AZ-0.4 catalysts reduced at 550 °C, and EDX maps with distribution of (I) Ni, (II) Al, and (III) Zr.

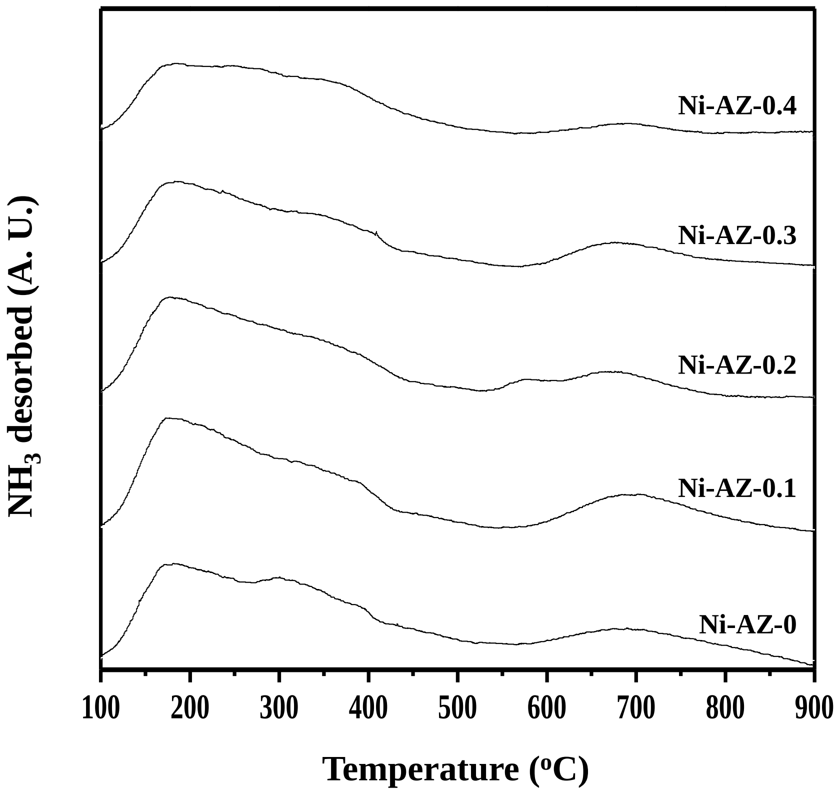

Fig. 3.6. NH_3-TPD profiles of Ni-AZ-X (X = 0, 0.1, 0.2, 0.3, and 0.4) catalysts reduced at 550 °C.

Table 3.2

Acidity of reduced Ni-AZ-X catalysts

Catalyst	Acidity (μmol-NH_3/g)[a]
Ni-AZ-0	131
Ni-AZ-0.1	124
Ni-AZ-0.2	101
Ni-AZ-0.3	86
Ni-AZ-0.4	79

[a] Calculated from peak area of NH_3-TPD profiles in Fig. 3.6

3.1.5. Catalytic performance in the steam reforming of ethanol

Fig. 3.7 shows the hydrogen yields with time on stream over Ni-AZ-X (X = 0, 0.1, 0.2, 0.3, and 0.4) catalysts in the steam reforming of ethanol at 500 °C. Both Ni-AZ-0 and Ni-AZ-0.1 catalysts experienced a catalytic deactivation resulting from the significant carbon deposition on the catalyst surface (Table 3.3). However, Ni-AZ-X (X = 0.2, 0.3, and 0.4) catalysts showed a stable performance with time on stream. It is believed that the addition of ZrO_2 improved the catalytic stability by inhibiting coke formation.

Detailed catalytic performance of Ni-AZ-X (X = 0, 0.1, 0.2, 0.3, and 0.4) catalysts in the steam reforming of ethanol at 500 °C after a 900 min-reaction is summarized in Table 3.3. Complete conversion of ethanol was achieved in all the catalysts under the conditions of high reaction temperature and excess amount of steam. This is in good agreement with the previous reports [75]. Selectivity for C_2H_4 over Ni-AZ-X catalysts decreased in the order of Ni-AZ-0 (9.8%) > Ni-AZ-0.1 (1.6%) > Ni-AZ-0.2 (0%) = Ni-AZ-0.3 (0%) = Ni-AZ-0.4 (0%). This can be explained by the fact that large amount of acid sites in the supports promoted the dehydration of ethanol to ethylene via one-step elimination mechanism [76]. The amount of carbon deposition decreased in the order of Ni-AZ-0 (28.8%) > Ni-AZ-0.1 (21.5%) > Ni-AZ-0.2 (3.5%) > Ni-AZ-0.3 (2.6%) > Ni-AZ-0.4 (1.3%) (Table 3.3). This might be because ZrO_2 in the Ni-AZ-X catalysts hindered both ethanol dehydration reaction (Equation 2) and ethylene formation reaction related to coking. It was also observed that CO/CO_2 molar ratio increased with increasing Zr/Al molar ratio (with decreasing acidity) in the order of Ni-AZ-0 (0.045) < Ni-AZ-0.1 (0.049) ≈ Ni-AZ-0.2 (0.053) = Ni-AZ-0.3 (0.053) < Ni-AZ-0.4 (0.240). This result indicates that water-gas shift reaction (Equation 6) was suppressed with increasing Zr/Al molar ratio (with decreasing acidity). It has been reported that the increased surface acidity promotes the water-gas shift reaction by increasing the number of adsorbed CO species [77]. Therefore, it can be inferred that an excess amount of ZrO_2 hindered water-gas shift reaction in the steam reforming of ethanol.

Fig. 3.8 shows the hydrogen yields over Ni-AZ-X (X = 0, 0.1, 0.2, 0.3, and 0.4) catalysts in the steam reforming of ethanol obtained after a 900 min-reaction, plotted as a function of Zr/Al molar ratio and acidity of the catalyst. Hydrogen yields showed a volcano-shaped curve with respect to Zr/Al molar ratio and acidity of the catalyst. Hydrogen yield decreased in the order of Ni-AZ-0.2 > Ni-AZ-0.3 > Ni-AZ-0.1 > Ni-AZ-0.4 > Ni-AZ-0. Among the catalysts tested, Ni-AZ-0.2 catalyst exhibited the best catalytic performance in terms of hydrogen yield. Although acidity of the catalyst was not the sole factor determining the catalytic performance in the steam reforming of ethanol, it greatly affected the reaction path and stability. Relatively more acidic catalysts (Ni-AZ-0 and Ni-AZ-0.1) exhibited low hydrogen yield because undesired ethanol dehydration reaction occurred on the acid-rich surface, resulting in a severe coke formation [76]. On the other hand, relatively less acidic catalysts (Ni-AZ-0.3 and Ni-AZ-0.4) showed low hydrogen yield due to low reactivity for water-gas shift reaction.

In the aspect of textural properties and reducibility, it was revealed that the addition of ZrO_2 decreased surface area and increased reducibility of the catalysts. As these two factors affect the catalytic activity in an opposite way, it is believed that high surface area of Ni-AZ-0 and Ni-AZ-0.1 compensates low reducibility, and high reducibility of Ni-AZ-0.3 and Ni-AZ-0.4 compensates low surface area. Consequently, it is concluded that catalytic performance of Ni-AZ-X catalysts was well correlated with acidity regardless of the effect of textural properties and reducibility. Among the catalysts tested, Ni-AZ-0.2 catalyst with an intermediate acidity showed the maximum hydrogen yield.

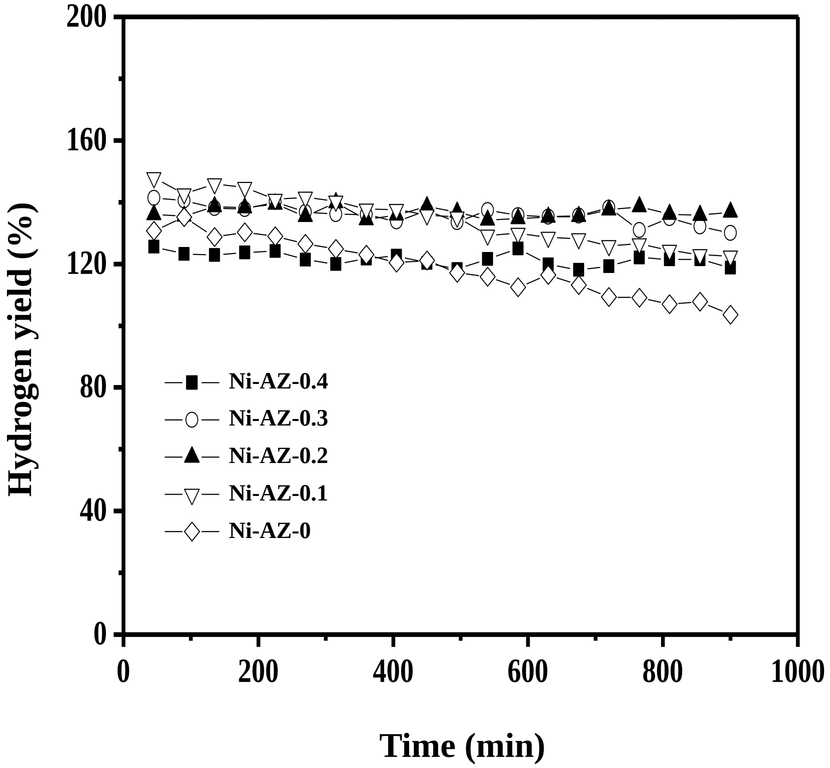

Fig. 3.7. Hydrogen yields with time on stream in the steam reforming of ethanol over Ni-AZ-X (X = 0, 0.1, 0.2, 0.3, and 0.4) catalysts at 500 ^{o}C. All the catalysts were reduced at 550 ^{o}C for 3 h prior to the reaction.

Table 3.3

Catalytic performance of Ni-AZ-X catalysts in the steam reforming of ethanol at 500 ^{o}C after a 900 min-reaction

Catalyst	Ethanol conversion (%)	Hydrogen yield (%)	Selectivity for C_2H_4 (%)	CO/CO_2 molar ratio	Amount of carbon deposition (wt%)[a]
Ni-AZ-0	100	104	9.8	0.045	28.8
Ni-AZ-0.1	100	123	1.6	0.049	21.5
Ni-AZ-0.2	100	137	0	0.053	3.5
Ni-AZ-0.3	100	130	0	0.053	2.6
Ni-AZ-0.4	100	119	0	0.240	1.3

[a] Determined by CHNS elemental analysis

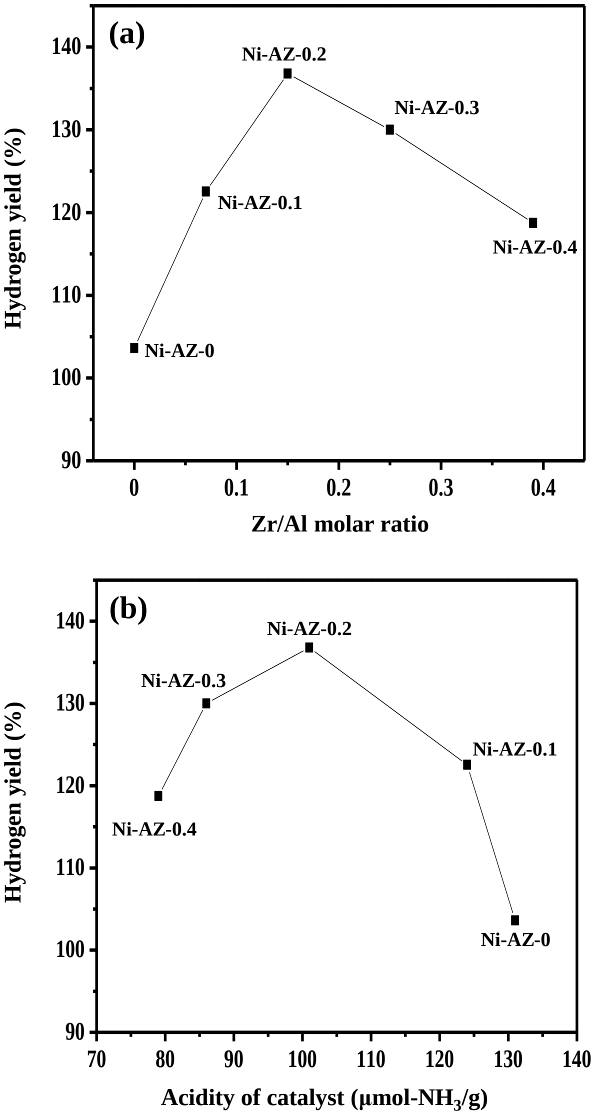

Fig. 3.8. Hydrogen yields over Ni-AZ-X (X = 0, 0.1, 0.2, 0.3, and 0.4) catalysts in the steam reforming of ethanol obtained after a 900 min-reaction, plotted as a function of (a) Zr/Al molar ratio and (b) acidity of the catalyst.

3.2. Mesoporous nickel-alumina-zirconia xerogel catalyst with various nickel content

3.2.1. Textural properties of calcined catalysts

Textural properties of XNiAZ (X = 5, 10, 15, 20, and 25) catalysts were characterized by nitrogen adsorption-desorption isotherm measurements as presented in Fig. 3.9. All the XNiAZ catalysts exhibited type-IV isotherms with H2-type hysteresis loops, indicating the capillary condensation in mesopores [65,78]. It is known that the formation of mesoporous structure in the catalysts is due to the removal of entrapped solution in the gel during the drying process. Detailed physicochemical properties of XNiAZ (X = 5, 10, 15, 20, and 25) catalysts are summarized in Table 3.4. From the ICP-AES measurements, it was revealed that measured nickel contents of XNiAZ catalysts were almost identical to the designed values. All the XNiAZ catalysts showed high surface area (> 237 m^2/g) with no great difference. Large pore volume (> 0.4 cm^3/g) and large average pore diameter (> 6 nm) were also observed in all the catalysts, with no great difference with respect to nickel content. From these results, it was confirmed that a mesoporous structure of XNiAZ catalysts was successfully formed.

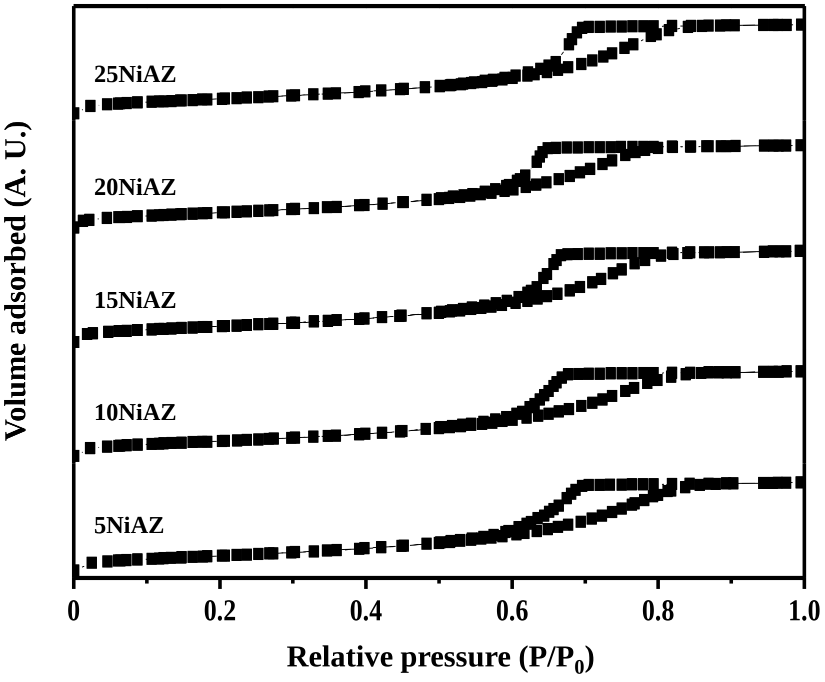

Fig. 3.9. Nitrogen adsorption-desorption isotherms of XNiAZ (X = 5, 10, 15, 20, and 25) catalysts calcined at 550 °C.

Table 3.4

Detailed physicochemical properties of XNiAZ catalysts calcined at 550 °C for 5 h

Catalyst	Ni loading (wt%)[a]	Surface area (m^2/g)[b]	Pore volume (cm^3/g)[c]	Average pore diameter (nm)[d]
5NiAZ	4.9	240	0.45	7.5
10NiAZ	9.9	243	0.43	7.2
15NiAZ	14.9	251	0.46	7.4
20NiAZ	19.7	245	0.42	6.9
25NiAZ	24.4	237	0.45	7.6

[a] Determined by ICP-AES measurement

[b] Calculated by the BET equation

[c] BJH desorption pore volume

[d] BJH desorption average pore diameter

3.2.2. Crystalline structure and reducibility

XRD techniques were employed for structure characterization of XNiAZ (X = 5, 10, 15, 20, and 25) catalysts calcined at 550 °C, as presented in Fig. 3.10(a). It is known that each precursor for Ni, Al, and Zr is readily oxidized and crystallized into NiO, γ-Al_2O_3, and monoclinic ZrO_2 when it is calcined at temperatures above 400 °C in the oxidative atmosphere [79]. However, no characteristic diffraction peaks for NiO, Al_2O_3, and ZrO_2 were detected in the 5NiAZ and 10NiAZ catalysts. This might be because NiO, Al_2O_3, and ZrO_2 independently prohibited the crystal nucleation and growth as phase retardants through the formation of amorphous NiO-Al_2O_3-ZrO_2 composite structure [80]. The diffraction peaks corresponding to NiO (solid lines in Fig. 3.10(a)) were observed in the XNiAZ (X = 15, 20, and 25) catalysts, although they were still close to amorphous phase rather than crystalline phase. This can be understood by the fact that NiO with short-range order is duplicated or superpositioned due to the increase of absolute amount of NiO species. Therefore, it can be inferred that amorphous NiO-Al_2O_3-ZrO_2 composite structure was predominantly formed in the calcined XNiAZ xerogel catalysts, resulting in high dispersion of NiO.

Fig. 3.10(b) shows the XRD patterns of XNiAZ (X = 5, 10, 15, 20, and 25) catalysts reduced at 550 °C. It is noteworthy that diffraction peaks (solid lines in Fig. 3.10(b)) corresponding to metallic nickel appeared in all the reduced catalysts; no diffraction peaks indicative of NiO were observed. This means that NiO in the NiO-Al_2O_3-ZrO_2 composite structure was completely reduced into metallic nickel during the reduction process employed in this work.

TPR profiles corresponding to XNiAZ (X = 5, 10, 15, 20, and 25) catalysts are depicted in Fig. 3.11. All the catalysts exhibited a single reduction band, which represented a homogeneous metal-support interaction. From XRD results shown in Fig. 3.10(a), it can be inferred that the reduction band is related to reduction of NiO interacting with Al_2O_3-ZrO_2 support. The amount of hydrogen consumption of XNiAZ catalysts monotonically increased with increasing nickel content due to the increase of absolute amount of nickel species. In the XNiAZ (X = 5, 10, and 15) catalysts, the reduction peak temperature decreased with increasing nickel content. This can be understood by the fact that nickel species strongly interacted with Al_2O_3-ZrO_2 support in the catalysts of low nickel content [81]. On the other hand, the reduction peak temperature increased with increasing nickel content in the XNiAZ (X = 15, 20, and 25) catalysts. This might be because NiO with short-range order was responsible for slow hydrogen diffusion into NiO phase, resulting in low reducibility [82]. In summary, reducibility of the catalysts showed a volcano-shaped trend with respect to nickel content; reducibility of the catalysts decreased in the order of 15NiAZ > 20NiAZ > 10NiAZ > 5NiAZ > 25NiAZ.

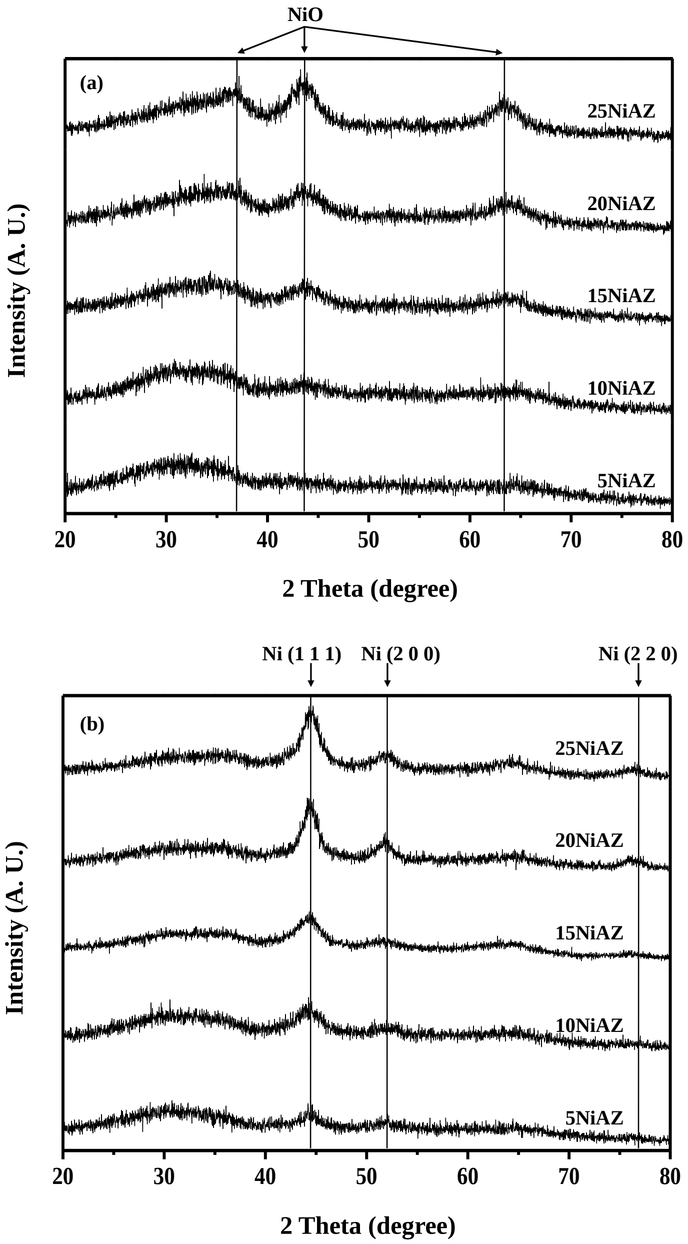

Fig. 3.10. XRD patterns of (a) calcined and (b) reduced XNiAZ (X = 5, 10, 15, 20, and 25) catalysts.

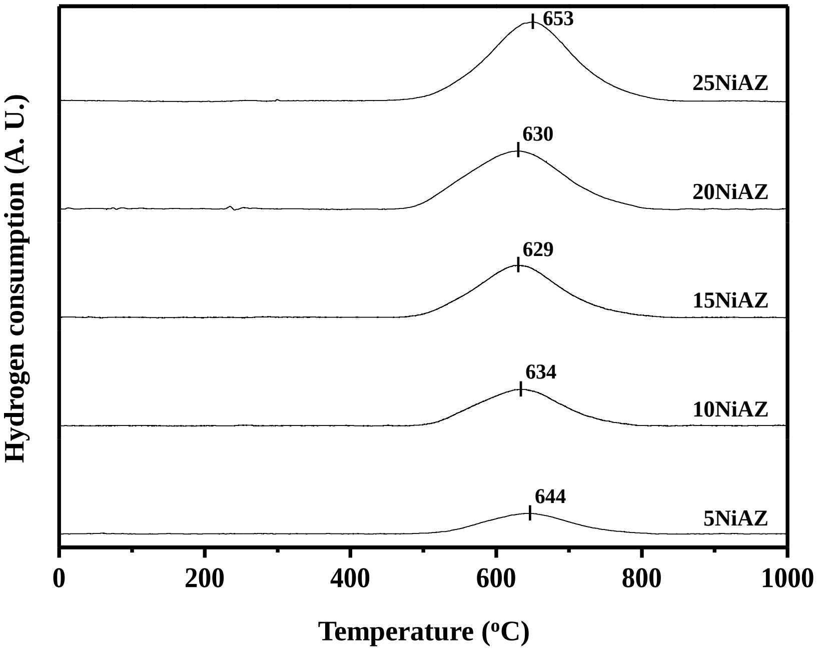

Fig. 3.11. TPR profiles of XNiAZ (X = 5, 10, 15, 20, and 25) catalysts calcined at 550 °C.

3.2.3. Characterization of reduced catalysts

Fig. 3.12 shows the nickel surface area of XNiAZ (X = 5, 10, 15, 20, and 25) catalysts, plotted as a function of nickel content. It is noticeable that nickel surface area decreased in the order of 15NiAZ > 20NiAZ > 10NiAZ > 25NiAZ > 5NiAZ and it showed a volcano-shaped trend with respect to nickel content, which was similar to the trend of reducibility. This trend can be understood by the fact that strong metal-support interaction reduced contact area of supported metal, resulting in the decrease of chemisorption capability [83]. However, 5NiAZ catalyst showed the lowest nickel surface area, while 25NiAZ catalyst showed the lowest reducibility. This is because low reducibility of 25NiAZ catalyst was caused by slow hydrogen diffusion not by strong metal-support interaction. It is also believed that large amount of support adjacent to metallic nickel in the 5NiAZ catalyst reduced the chemisorption capability, resulting in its low nickel surface area [33]. This result indicates that nickel was highly dispersed on the catalyst surface at an optimal nickel content [84]. This was further confirmed by TEM analyses. Fig. 3.13 shows the TEM images of 5NiAZ, 15NiAZ, and 25NiAZ catalysts reduced at 550 ^{o}C. No significant aggregation of metallic nickel was found in the reduced 15NiAZ catalyst (Fig. 3.13(b)). However, relatively large aggregates of metallic nickel were found in both 5NiAZ (Fig. 3.13(a)) and 25NiAZ catalyst (Fig. 3.13(c)), indicating relatively poor dispersion of metallic nickel. TEM results were well consistent with hydrogen chemisorption results (Fig. 3.12).

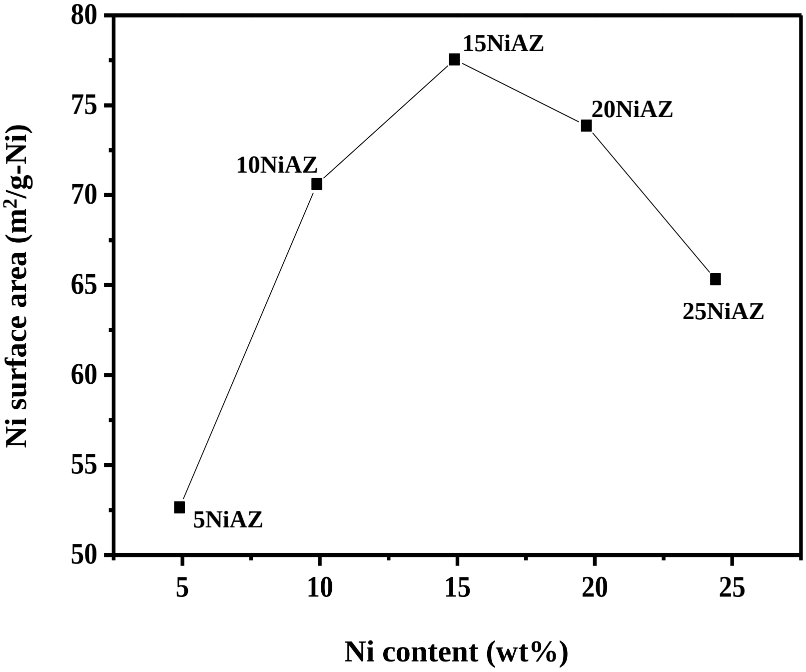

Fig. 3.12. Nickel surface area of XNiAZ (X = 5, 10, 15, 20, and 25) catalysts reduced at 550 °C, plotted as a function of nickel content.

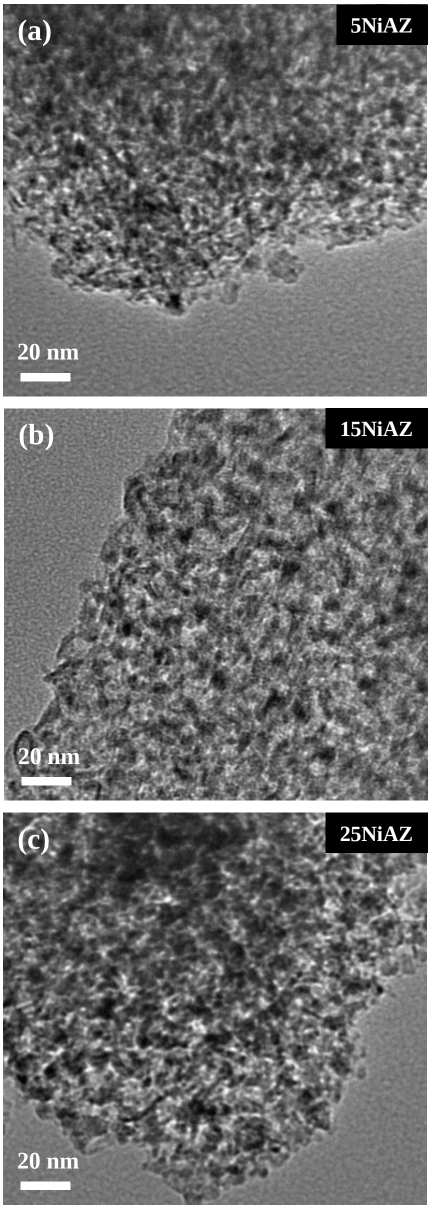

Fig. 3.13. TEM images of (a) 5NiAZ, (b) 15NiAZ, and (c) 25NiAZ catalysts reduced at 550 ^{o}C.

3.2.4. Catalytic performance in the steam reforming of ethanol

Hydrogen yield profiles with time on stream over XNiAZ (X = 5, 10, 15, 20, and 25) catalysts in the steam reforming of ethanol at 500 °C are represented in Fig. 3.14. Detailed values of ethanol conversion and hydrogen yield over XNiAZ (X = 5, 10, 15, 20, and 25) catalysts in the steam reforming of ethanol at 500 °C after a 2100 min-reaction are summarized in Table 3.5. XNiAZ (X = 10, 15, 20, and 25) catalysts exhibited a stable performance with time on stream and showed complete conversion of ethanol. In case of 5NiAZ catalyst, however, hydrogen yield drastically decreased after a 500 min-reaction. The XNiAZ (X = 5, 10, 15, 20, and 25) catalysts used for 2100 min-reaction were characterized in order to investigate the reason why 5NiAZ catalyst experienced a significant catalyst deactivation.

Fig. 3.15 shows the XRD patterns of used XNiAZ (X = 5, 10, 15, 20, and 25) catalysts after a 2100 min-reaction. No significant change in crystalline structure of metallic nickel was found in all the used catalysts, when compared to the reduced catalysts (Fig. 3.10(b)). However, diffraction peaks indicative of graphite carbon appeared in all the catalysts. It is noteworthy that the diffraction peak for graphite carbon was strongly observed in the 5NiAZ catalyst with the lowest nickel surface area. CHNS elemental analyses revealed that 36.9 wt% of carbon was deposited in the 5NiAZ catalyst after a 2100 min-reaction. It is well known that the deposited carbon species deactivate Ni-based catalysts by covering the active phase [85]. Therefore, it is believed that the large amount of carbon deposition was responsible for severe deactivation of 5NiAZ catalyst.

Selectivities for carbon-containing products over XNiAZ catalysts in the steam reforming of ethanol after a 2100 min-reaction are presented in Table 3.6. Interestingly, small amount of ethylene was observed over 5NiAZ catalyst which experienced a severe deactivation during the reaction. It has been reported that ethylene is an intermediate product formed by dehydration of ethanol ($C_2H_5OH \rightarrow C_2H_4 + H_2O$) over acid sites of the catalyst [86,87]. Therefore, it can be inferred that active phase of 5NiAZ was not sufficient to reform ethylene completely due to its low nickel surface area. Consequently, carbon deposition in the 5NiAZ catalyst can be explained by the existence of ethylene, because ethylene is the main precursor of coking [86]. On the other hand, C_2H_4 was not observed over XNiAZ (X = 10, 15, 20, and 25) catalysts, because the catalysts were sufficiently active to reform C_2H_4 completely. It is also noteworthy that selectivity for CH_4 showed an opposite trend to hydrogen yield over XNiAZ (X = 10, 15, 20, and 25) catalysts. This is because methane is another intermediate product which can be reformed depending on activity of the catalyst [88]. However, selectivities for CO and CO_2, which were related to water-gas shift reaction ($CO + H_2O \rightarrow CO_2 + H_2$), showed no consistent trend with respect to hydrogen yield. Therefore, it can be inferred that hydrogen yields over XNiAZ catalysts were mainly governed by methane reforming reaction ($CH_4 + 2H_2O \rightarrow 4H_2 + CO_2$).

A plot of the hydrogen yields over XNiAZ (X = 5, 10, 15, 20, and 25) catalysts in the steam reforming of ethanol as a function of nickel surface area is presented in Fig. 3.16. It was revealed that hydrogen yield increased with increasing nickel surface area. In other words, high nickel surface area was required to promote hydrogen production by steam reforming of ethanol. This is because nickel surface area is closely associated with accessibility of reactant to active sites of the catalyst. It has also been reported that surface area of metallic nickel is well matched with chemisorption capability of ethanol [88]. Among the catalysts tested, 15NiAZ catalyst with the highest nickel surface area showed the best catalytic performance.

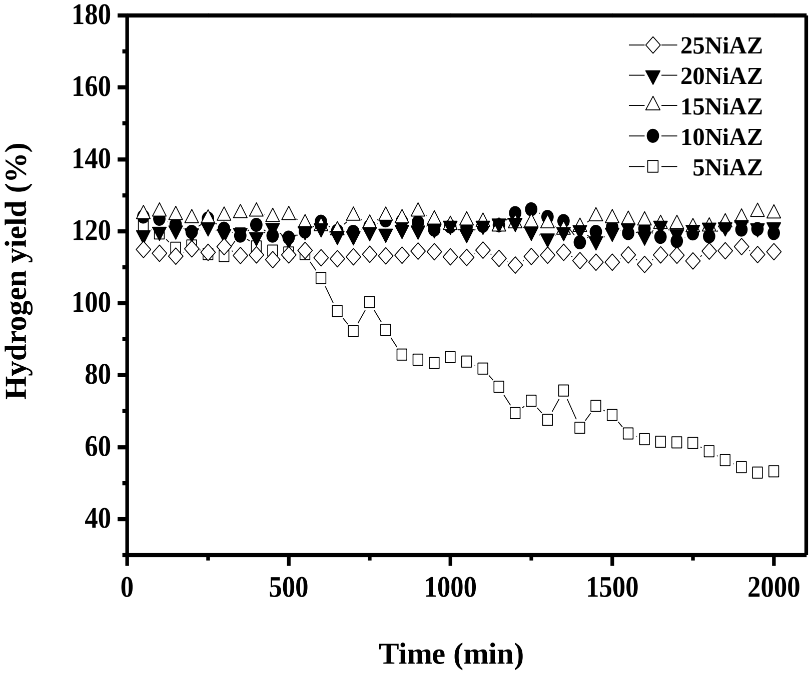

Fig. 3.14. Hydrogen yields with time on stream in the steam reforming of ethanol over XNiAZ (X = 5, 10, 15, 20, and 25) catalysts at 500 ^{o}C. All the catalysts were reduced at 550 ^{o}C for 3 h prior to the reaction.

Table 3.5

Catalytic performance of XNiAZ catalysts in the steam reforming of ethanol at 500 °C after a 2100 min-reaction

Catalyst	Ethanol conversion (%)	Hydrogen yield (%)
5NiAZ	72	54.0
10NiAZ	100	120.6
15NiAZ	100	124.9
20NiAZ	100	120.9
25NiAZ	100	110.6

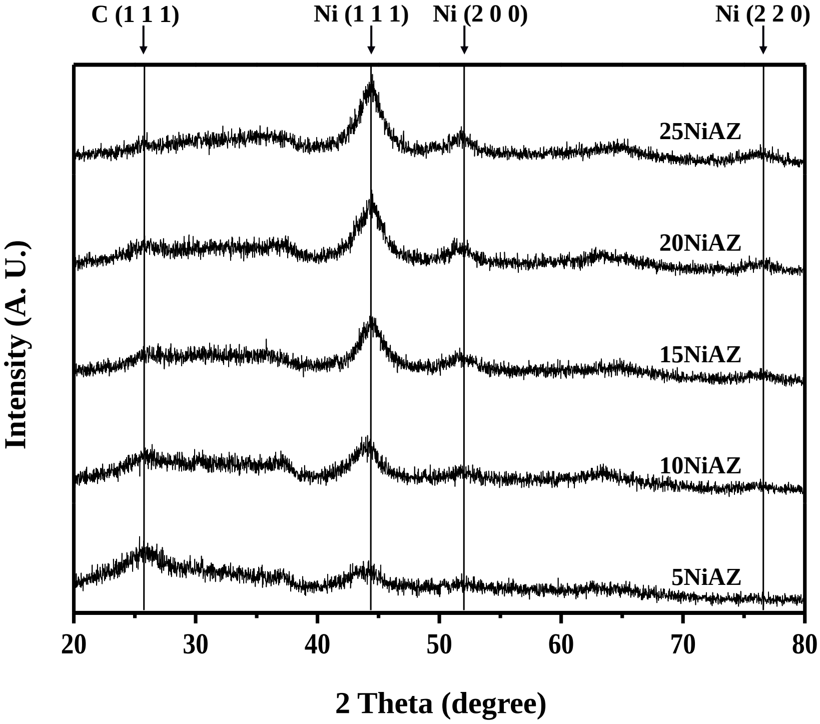

Fig. 3.15. XRD patterns of used XNiAZ (X = 5, 10, 15, 20, and 25) catalysts.

Table 3.6

Selectivities for carbon-containing products over XNiAZ catalysts in the steam reforming of ethanol at 500 °C after a 2100 min-reaction

Catalyst	Selectivity for CH_4 (%)	Selectivity for CO (%)	Selectivity for CO_2 (%)	Selectivity for C_2H_4 (%)
5NiAZ	11.6	0	47.2	2.0
10NiAZ	25.6	10.6	55.7	0
15NiAZ	21.6	10.5	57.6	0
20NiAZ	25.3	6.5	56.7	0
25NiAZ	28.6	5.3	55.7	0

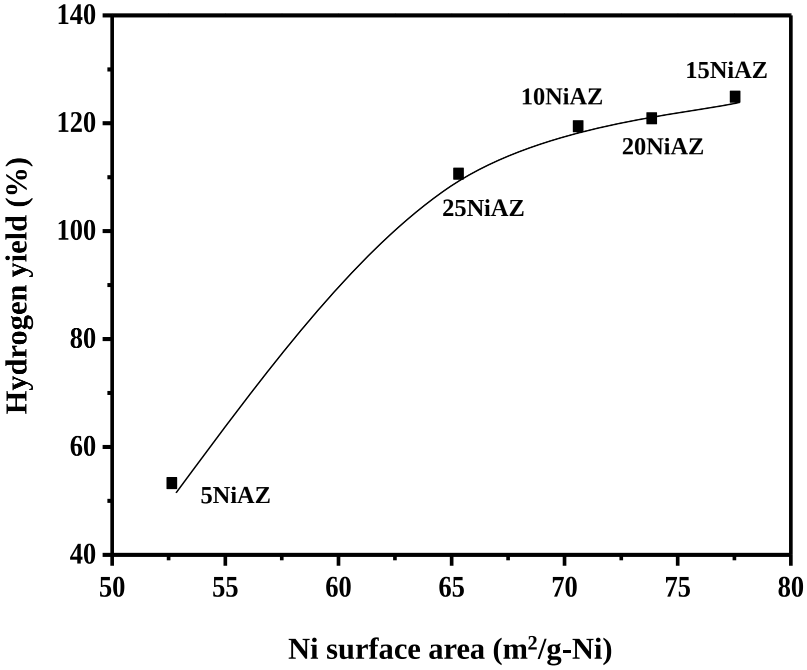

Fig. 3.16. Hydrogen yields over XNiAZ (X = 5, 10, 15, 20, and 25) catalysts in the steam reforming of ethanol obtained after a 2100 min-reaction, plotted as a function of nickel surface area.

3.2.5. Effect of total feed rate on the catalytic performance

Fig. 3.17 shows the hydrogen yields and other product distributions over 15NiAZ catalyst in the steam reforming of ethanol, plotted as a function of total feed rate. Total feed rate was controlled by changing the catalyst amount. It has been reported that total feed rate has a significant effect on the catalytic performance of reforming catalyst, because it is related to heat and mass transfer during the reforming reactions [89,90]. It is also known that total feed rate affects product distribution in the steam reforming of ethanol by modulating methane steam reforming reaction and water-gas shift reaction [90]. As shown in Fig. 3.17, selectivities for CO_2 and CH_4 were almost constant with regard to total feed rate, while selectivity for CO slightly increased with increasing total feed rate. Thus, it can be inferred that water-gas shift reaction was inhibited at high total feed rate, because contact time was not sufficient for the reaction. Nevertheless, complete conversion of ethanol was achieved and hydrogen yields over 15NiAZ catalyst were almost constant with regard to total feed rate. It can be summarized that 15NiAZ catalyst has a strong capability of facilitating heat and mass transfer of reactant and product during the steam reforming of ethanol, demonstrating its potential applicability in large-scale hydrogen production.

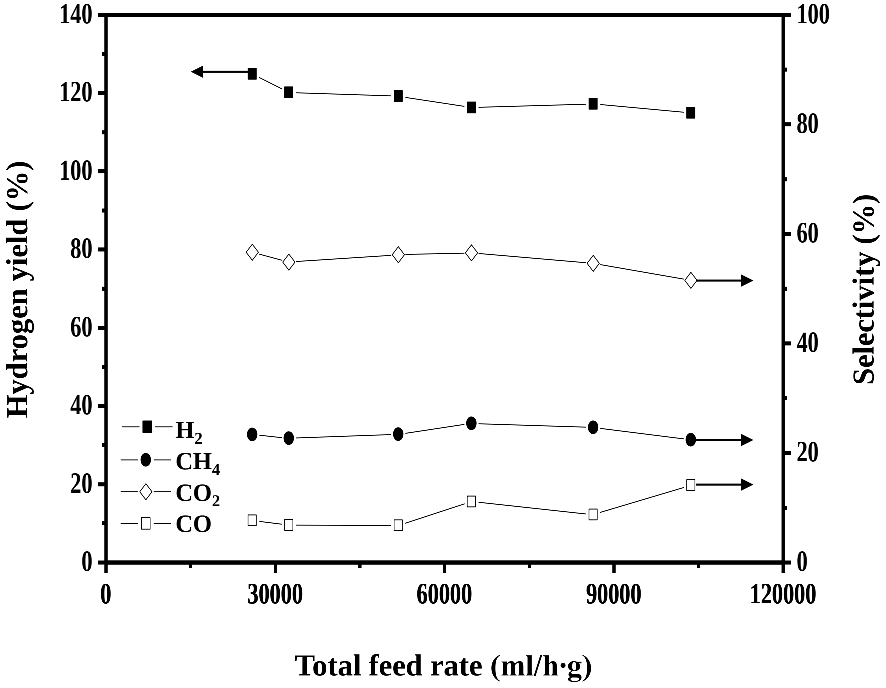

Fig. 3.17. Hydrogen yields and selectivities for CO, CO_2, and CH_4 over 15NiAZ catalyst in steam reforming of ethanol obtained after a 700 min-reaction, plotted as a function of total feed rate.

3.3. Mesoporous nickel-alumina-zirconia aerogel catalyst prepared by carbon dioxide supercritical drying

3.3.1. Textural properties of calcined catalysts

Fig. 3.18 shows the nitrogen adsorption-desorption isotherms of Ni-AZ and Ni/AZ catalysts. For comparison, isotherm of AZ support is also represented. All the samples showed type-IV isotherms with hysteresis loops, indicating the capillary condensation in mesopores [78]. It is noteworthy that all the isotherms exhibited H1-type hysteresis loop which is characteristic of spherical-shaped agglomerates or compacts in aerogel structure [91,92]. Thus, it can be inferred that the well-developed mesoporous structure of Al_2O_3-ZrO_2 support was preserved in the Ni-AZ and Ni/AZ catalysts. Table 3.7 shows the detailed textural properties of the catalysts and the support. ICP-AES results revealed that nickel content of Ni-AZ and Ni/AZ catalysts was in good agreement with the designed value. It was also observed that AZ support and both catalysts retained large pore volume (> 0.8 cm^3/g) and large average pore diameter (> 10 nm). This result indicates that pore characteristics of aerogel catalyst were improved compared to those of xerogel catalyst in the previous work [93]. However, Ni/AZ catalyst retained relatively low surface area (222 m^2/g) while AZ support and Ni-AZ catalyst exhibited high surface area (> 300 m^2/g). It is believed that the decrease in surface area of Ni/AZ catalyst was due to pore blockage occurred during the impregnation of nickel precursor [94,95]. In summary, Ni-AZ catalyst retained more favorable textural properties than Ni/AZ catalyst.

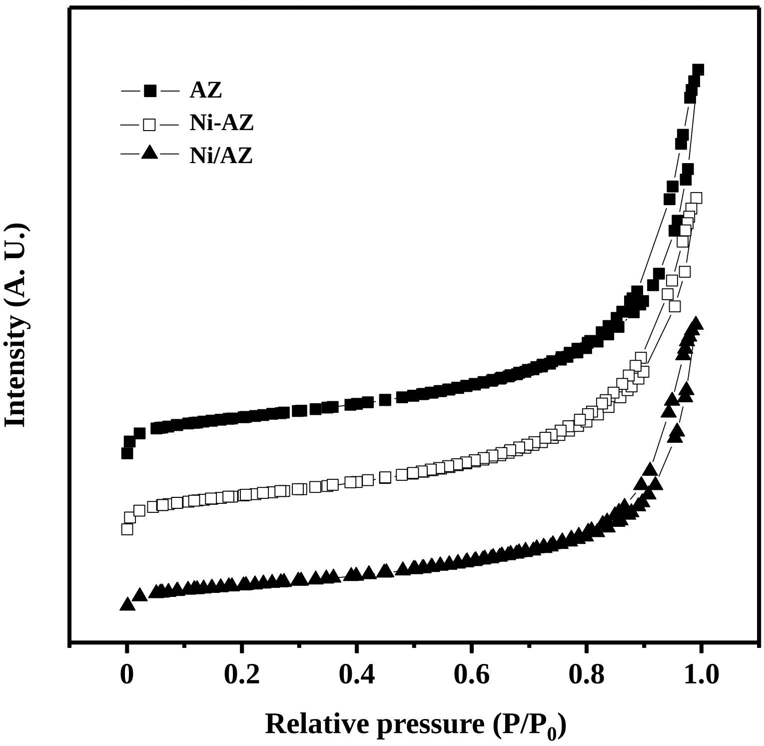

Fig. 3.18. Nitrogen adsorption-desorption isotherms of Ni-AZ and Ni/AZ catalysts calcined at 550 °C for 5 h.

Table 3.7

Detailed physicochemical properties of Ni-AZ and Ni/AZ catalysts calcined at 550 °C for 5 h

Sample	Ni content (wt%)[a]	Surface area (m^2/g)[b]	Pore volume (cm^3/g)[c]	Average pore diameter (nm)[d]
AZ	-	329	1.13	13.7
Ni-AZ	15.0	315	1.03	13.1
Ni/AZ	14.3	222	0.89	16.0

[a] Determined by ICP-AES measurement

[b] Calculated by the BET equation

[c] BJH desorption pore volume

[d] BJH desorption average pore diameter

3.3.2. Crystalline structure and reducibility

Fig. 3.19(a) shows the XRD patterns of Ni-AZ and Ni/AZ catalysts calcined at 550 ^{o}C for 5 h. For comparison, XRD pattern of AZ support is also included in Fig. 3.19(a). It is noteworthy that no characteristic diffraction peaks for NiO, Al_2O_3, and ZrO_2 were detected in the AZ support and Ni-AZ catalyst. This means that amorphous Al_2O_3-ZrO_2 and NiO-Al_2O_3-ZrO_2 composite structures were formed in the AZ support and Ni-AZ catalyst, because co-existence of NiO, Al_2O_3, and ZrO_2 significantly prohibited the crystallization of individual NiO, Al_2O_3, and ZrO_2 structure, indicating that they played a role as phase retardants [96]. On the other hand, the diffraction peaks indicative of NiO (closed circles in Fig. 3.19(a)) were observed in the Ni/AZ catalyst. This can be explained by the fact that Ni precursor in the Ni/AZ catalyst was impregnated on the amorphous AZ support while NiO species in the Ni-AZ catalyst directly participate in forming an amorphous NiO-Al_2O_3-ZrO_2 composite structure. For this reason, NiO species in the Ni/AZ catalyst exhibited high crystallinity due to its relatively weak interaction with support. As a consequence, it can be inferred that the formation of NiO-Al_2O_3-ZrO_2 composite structure in the calcined Ni-AZ catalyst was attributed to high dispersion of NiO.

TPR measurements were carried out to determine reducibility of the catalysts as presented in Fig. 3.19(b). Considering the XRD results of calcined catalysts, it is believed that the reduction band in the Ni/AZ catalyst is related to the reduction of NiO interacted with Al_2O_3-ZrO_2 support. In case of Ni-AZ catalyst, the reduction band is related to the reduction of fine crystallites of nickel oxide in the form of $NiO-Al_2O_3-ZrO_2$ composite structure [97]. Ni/AZ catalyst showed higher reduction peak temperature than Ni-AZ catalyst, because large crystallites of NiO in the Ni/AZ catalyst was unfavorable in hydrogen diffusion [98].

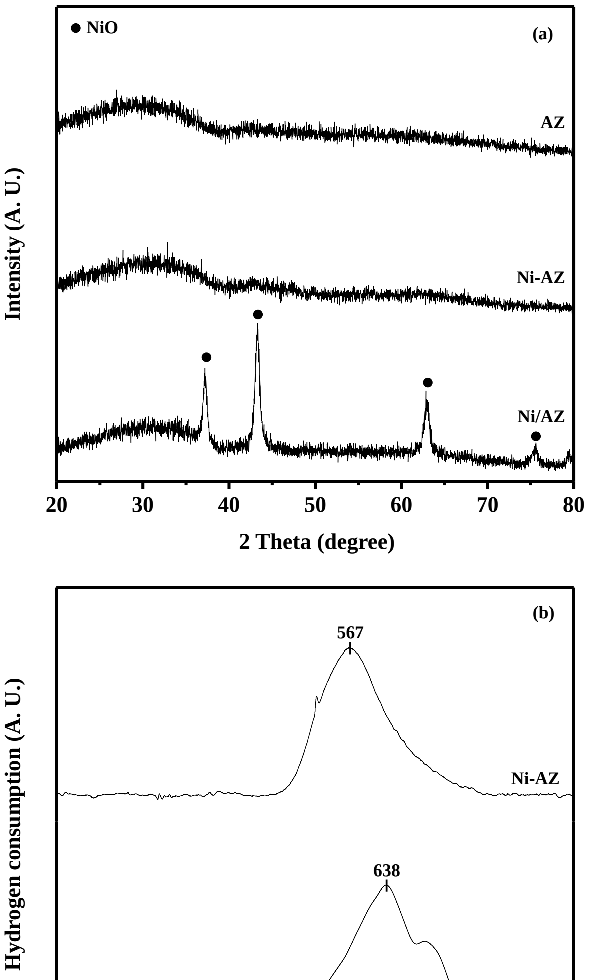

Fig. 3.19. (a) XRD patterns of Ni-AZ and Ni/AZ catalysts calcined at 550 °C for 5 h and (b) TPR profiles of Ni-AZ and Ni/AZ catalysts calcined at 550 °C for 5 h.

3.3.3. Characterization of reduced catalysts

Fig. 3.20 shows the XRD patterns of Ni-AZ and Ni/AZ catalysts reduced at 650 ^oC. Diffraction peaks (solid lines in Fig. 3.20) indicative of metallic nickel were observed in the Ni-AZ and Ni/AZ catalysts, while no diffraction peaks corresponding to NiO were observed. This indicates that NiO species in the Ni-AZ and Ni/AZ catalysts were completely reduced into metallic nickel during the reduction process employed in this work. Furthermore, metallic nickel with large particle size was formed in the Ni/AZ catalyst. For direct comparison of nickel crystallite size of the reduced catalysts, nickel particle sizes calculated from Ni (1 1 1) diffraction peak in Fig. 3.20 using the Scherrer equation are summarized in Table 3.8.

In order to evaluate Ni dispersion in the reduced catalysts, TEM analyses were conducted. From the TEM images (Fig. 3.21) of the reduced catalysts, it was observed that no aggregates of metallic nickel were found in the Ni-AZ catalyst while metallic nickel was largely aggregated in the Ni/AZ catalyst. To quantify Ni dispersion in the catalysts, particle size distribution of metallic nickel was measured on TEM images. As shown in Fig. 3.21, Ni-AZ catalyst exhibited a narrow particle size distribution of metallic nickel with an average value of 5.8 nm. However, Ni/AZ catalyst exhibited a broad particle size distribution of metallic nickel with an average value of 18.0 nm. It is believed that relatively large particle size of metallic nickel in the Ni/AZ catalyst was due to high crystallinity of NiO in the calcined Ni/AZ catalyst.

H_2-TPD experiments were performed over Ni-AZ and Ni/AZ catalysts in order to determine the amount of hydrogen chemisorbed, as shown in Fig. 3.22. TPD profiles for both catalysts were deconvoluted to three domains of H_2 desorption peaks. However, it known that the high temperature peak above 600 ^oC was attributed to H_2 located in the support by hydrogen spillover [99]. For this reason, two domains below 600 ^oC were considered to calculate nickel dispersion of the catalysts [100]. The amount of H_2 desorbed from each site was calculated from each deconvoluted area in the H_2-TPD profiles as summarized in Table 3.9. It was observed that Ni-AZ catalyst exhibited larger amount of H_2 desorbed from both weak and strong sites than Ni/AZ catalyst. Especially, the amount of H_2 desorbed from weak site showed clear distinction between two catalysts, demonstrating that preparation method strongly affected the amount of weak adsorption site. Nickel surface area and nickel particle size were calculated from total peak area of H_2-TPD profiles, except for the area above 600 ^oC (Table 3.9). Ni-AZ catalyst retained larger nickel surface area and smaller nickel particle size than Ni/AZ catalyst. This result was well consistent with XRD (Fig. 3.20 and Table 3.8) and TEM results (Fig. 3.21).

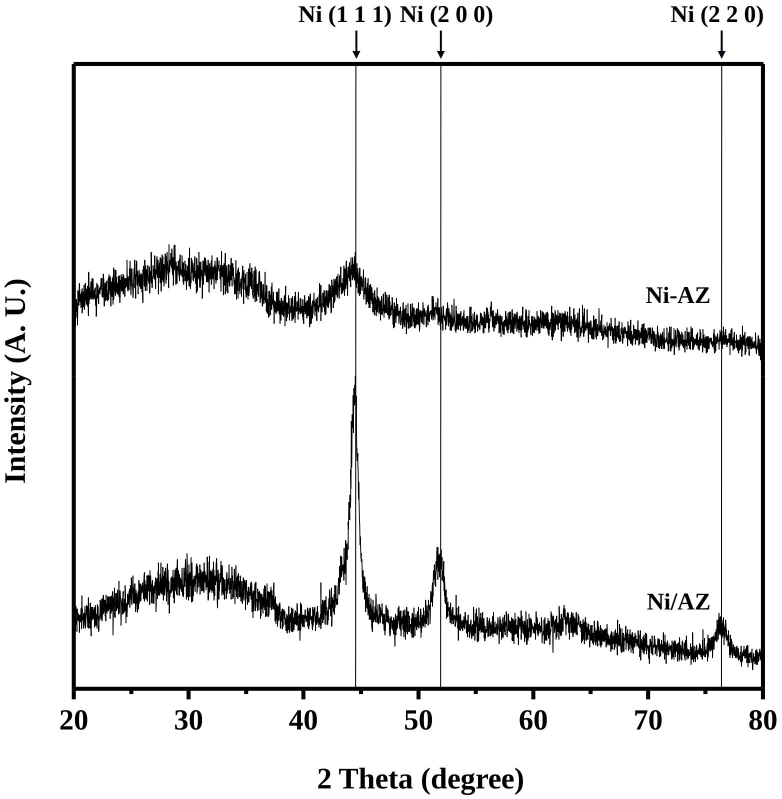

Fig. 3.20. XRD patterns of Ni-AZ and Ni/AZ catalysts reduced at 650 °C for 3 h.

Table 3.8

Nickel particle size of reduced Ni-AZ and Ni/AZ catalysts

Catalyst	Nickel particle size (nm)[a]
Ni-AZ	4.5
Ni/AZ	12.9

[a] Calculated from Ni (1 1 1) diffraction peak in Fig. 4.

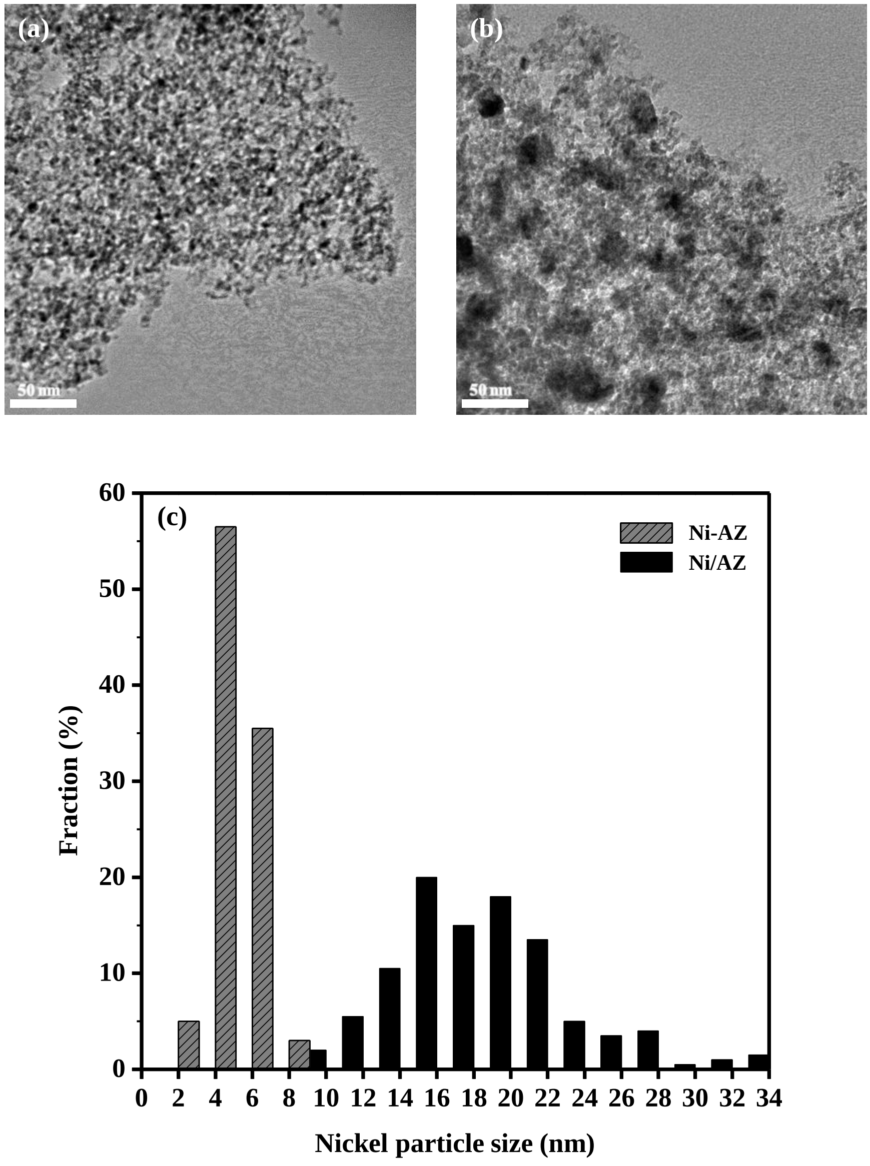

Fig. 3.21. TEM images of (a) Ni-AZ, (b) Ni/AZ catalysts reduced at 650 °C for 3 h and (c) particle size distributions of metallic nickel in the Ni-AZ and Ni/AZ catalysts reduced at 650 °C for 3 h.

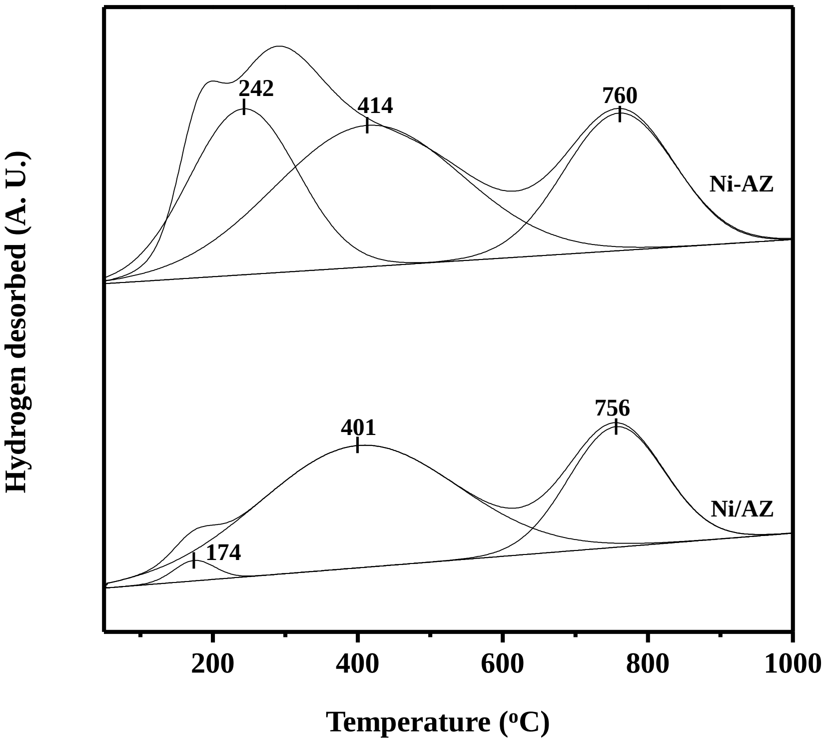

Fig. 3.22. H_2-TPD profiles of Ni-AZ and Ni/AZ catalysts reduced at 650 °C for 3 h.

Table 3.9

H_2-TPD results for reduced Ni-AZ and Ni/AZ catalysts

Catalyst		Ni-AZ	Ni/AZ
Amount of H_2 desorbed (μmol-H_2/g)[a]	Weak site (< 300 °C)	63.8 (40.3%)[b]	3.1 (3.4%)[b]
	Strong site (300-600 °C)	94.4 (59.7%)[b]	88.1 (96.6%)[b]
	Total	158.1	91.1
Nickel surface area (m^2/g-Ni)[c]		12.4	8.2
Nickel particle size (nm)[c]		7.1	14.2

[a] Calculated from peak area of H_2-TPD profiles in Fig. 3.22

[b] Values in parentheses are percentage of each deconvoluted area in the H_2-TPD profiles

[c] Calculated by assuming $H/Ni_{atom} = 1$

3.3.4. Catalytic performance in the steam reforming of ethanol

Fig. 3.23 shows the hydrogen yields with time on stream in the steam reforming of ethanol at 500 ^oC. Detailed catalytic performance of Ni-AZ and Ni/AZ catalysts in the steam reforming of ethanol at 500 ^oC obtained after a 2000 min-reaction is summarized in Table 3.10. Although both catalysts exhibited complete conversion of ethanol and stable catalytic performance, hydrogen production was more favorable over Ni-AZ catalyst in the steam reforming of ethanol. It is believed that high surface area, high reducibility, and high nickel dispersion of Ni-AZ catalyst are responsible for its superior catalytic activity.

In order to determine the reaction path, selectivities for carbon-containing by-products in the steam reforming of ethanol were obtained after a 2000 min-reaction as presented in Table 3.10. Carbon-containing compounds such as CH_4, CO, and CO_2 were produced as by-products. This implies that ethanol decomposition ($C_2H_5OH \rightarrow CH_4 + CO + H_2$) and steam reforming of ethanol to syngas ($C_2H_5OH + H_2O \rightarrow 2CO + 4H_2$) occurred for additional hydrogen production [101]. Water-gas shift reaction ($CO + H_2O \rightarrow H_2 + CO_2$) also occurred in presence of CO, because CO could be converted to CO_2 and H_2 through the reaction. As listed in Table 3.10, Ni-AZ catalyst exhibited low selectivity for CO and high selectivity for CO_2 compared to Ni/AZ catalyst, while selectivity for CH_4 over both catalysts showed no great difference. Therefore, it can be inferred that high hydrogen yield of Ni-AZ catalyst was mainly due to its high activity in water-gas shift reaction ($CO + H_2O \rightarrow CO_2 + H_2$).

CHNS elemental analyses revealed that 73.9 wt% of carbon was deposited on the Ni-AZ catalyst and 75.9 wt% of carbon was deposited on the Ni/AZ catalyst after a 2000 min-reaction. Although both catalysts experienced a severe coking, they showed a stable catalytic performance in the steam reforming of ethanol. For better investigation, TEM analyses were conducted as presented in Fig. 3.24. It was observed that filamentous carbon was formed on the used catalysts. It has been previously reported that filamentous carbon does not encapsulate active site if H_2/CO or H_2O/hydrocarbon ratios are sufficiently high [102]. Therefore, it can be inferred that both Ni/AZ and Ni-AZ catalysts showed no deactivation during the reaction in spite of large amount of carbon deposition because filamentous carbon did not encapsulate the active sites of the catalysts.

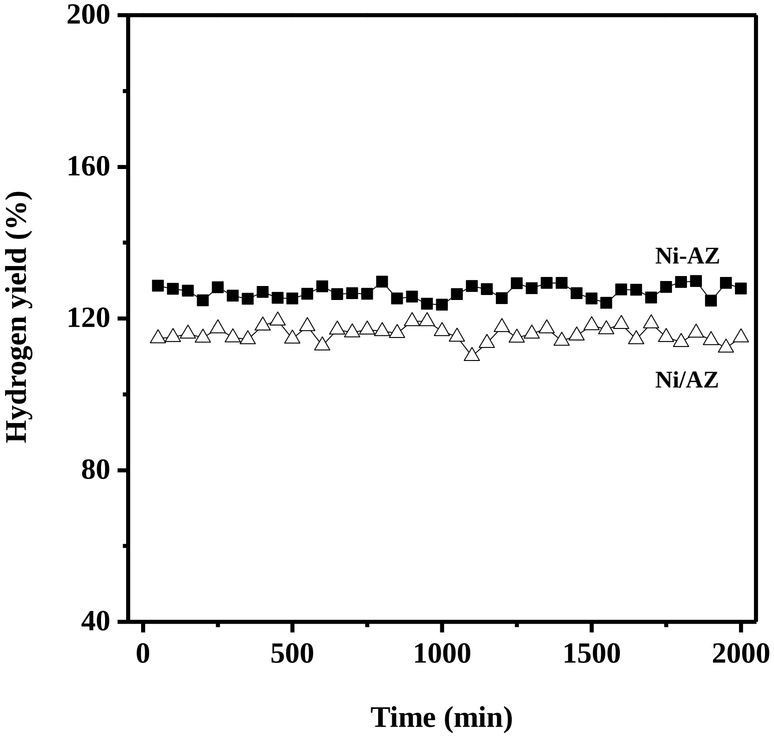

Fig. 3.23. Hydrogen yields with time on stream in the steam reforming of ethanol over Ni-AZ and Ni/AZ catalysts at 500 ^oC. Both catalysts were reduced at 650 ^oC for 3 h prior to the reaction.

Table 3.10

Detailed catalytic performance of Ni-AZ and Ni/AZ catalysts in the steam reforming of ethanol at 500 ^{o}C after a 2000 min-reaction

Catalyst	Ethanol conversion (%)	Hydrogen yield (%)	Selectivity for CH_4 (%)	Selectivity for CO (%)	Selectivity for CO_2 (%)
Ni-AZ	100	128	24.6	3.0	72.5
Ni/AZ	100	115	23.2	6.7	70.2

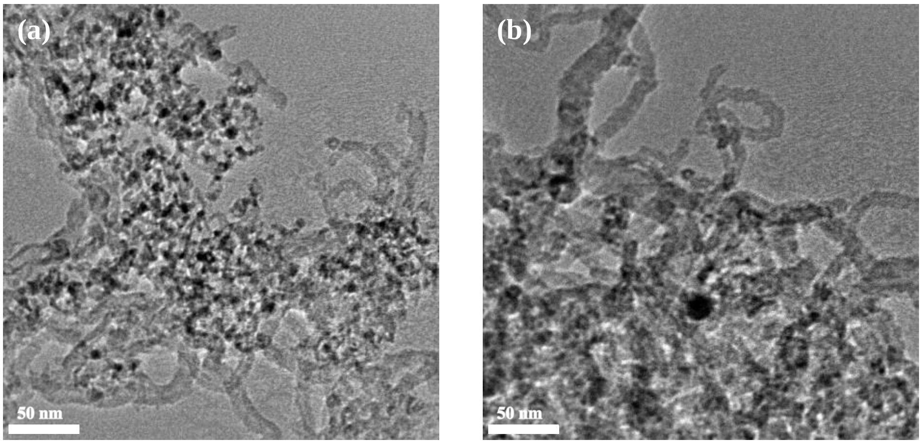

Fig. 3.24. TEM images of (a) Ni-AZ and (b) Ni/AZ catalysts used at 500 ^{o}C for 2000 min.

3.3.5. Effect of reaction temperature on catalytic performance

Fig. 3.25 shows the hydrogen yields over Ni-AZ and Ni/AZ catalysts in the steam reforming of ethanol, plotted as a function of reaction temperature. It was observed that both catalysts exhibited complete conversion of ethanol at temperatures above 400 ^{o}C, and they showed the highest hydrogen yield at 650 ^{o}C. It was also revealed that Ni-AZ catalyst exhibited higher hydrogen yield than Ni/AZ catalyst within entire temperature range, demonstrating versatile applicability of Ni-AZ catalyst in wide temperature window.

In order to elucidate the effect of reaction temperature on the reaction path, selectivities for carbon-containing by-products were plotted as a function of reaction temperature (Fig. 3.26). It has been reported that steam reforming of methane ($CH_4 + 2H_2O \rightarrow 4H_2 + CO_2$) and steam reforming of ethanol to syngas ($C_2H_5OH + H_2O \rightarrow 2CO + 4H_2$) are endothermic, while water gas shift reaction ($CO + H_2O \rightarrow CO_2 + H_2$) is exothermic [103]. Accordingly, selectivity for CH_4 decreased with increasing reaction temperature, indicating that methane steam reforming was favorable at high temperature. However, selectivity for CO increased with increasing reaction temperature, because water-gas shift reaction was inhibited at high temperature. On the other hand, selectivity for CO_2 showed no consistent trend with regard to reaction temperature, because CO_2 was produced by methane steam reforming and water-gas shift reaction. Therefore, the best catalytic performance at 650 ^{o}C can be understood by the fact that hydrogen production is governed by methane steam reforming and water-gas shift reaction.

In order to investigate the applicability of the catalysts at high reaction temperatures, stability tests for Ni-AZ and Ni/AZ catalysts were conducted at 650 ^{o}C for 2000 min as presented in Fig. 3.27. It was revealed that both catalysts exhibited a stable catalytic performance without any significant deactivation. Thus, it can be inferred that the catalysts still showed high stability even at high reaction temperature (650 ^{o}C), because coke formation reaction such as Boudouard reaction ($2CO \rightarrow CO_2 + C$) is exothermic while steam reforming reaction ($C_2H_5OH + 3H_2O \rightarrow 2CO_2 + 6H_2$) is endothermic.

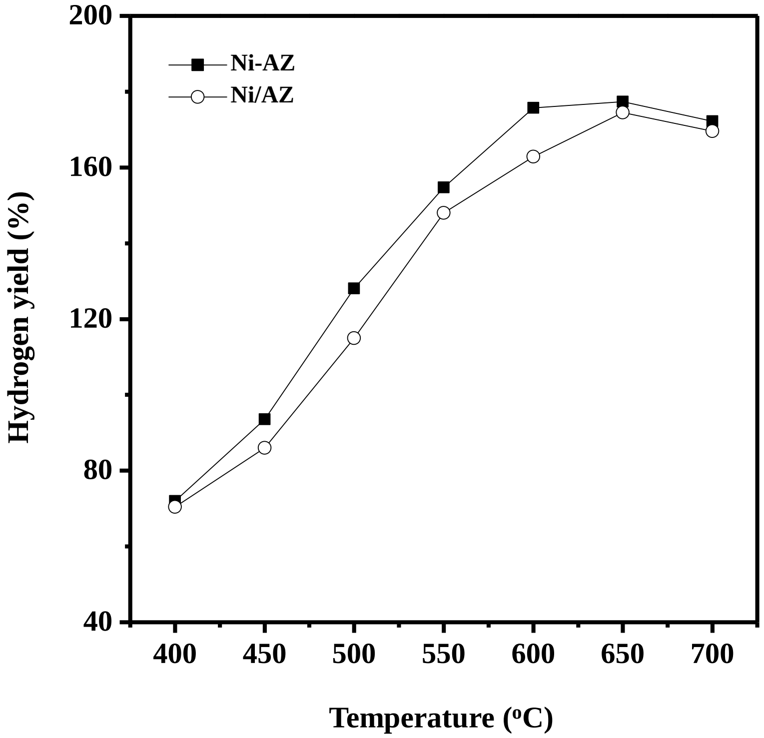

Fig. 3.25. Hydrogen yields over Ni-AZ and Ni/AZ catalysts in the steam reforming of ethanol, plotted as a function of reaction temperature.

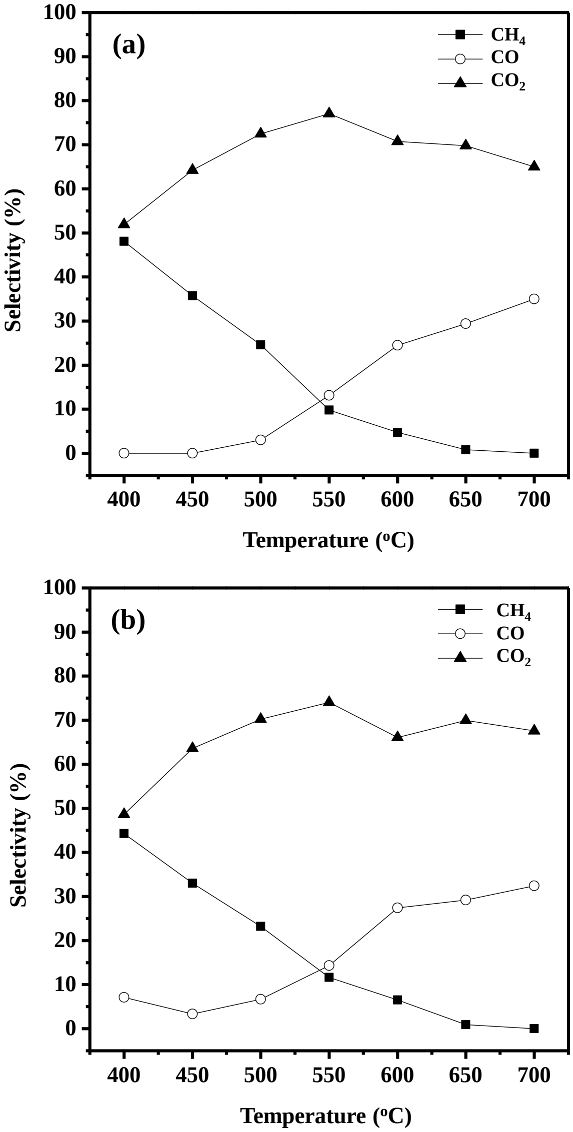

Fig. 3.26. Selectivities for CH_4, CO, and CO_2 over (a) Ni-AZ and (b) Ni/AZ catalysts in the steam reforming of ethanol, plotted as a function of reaction temperature.

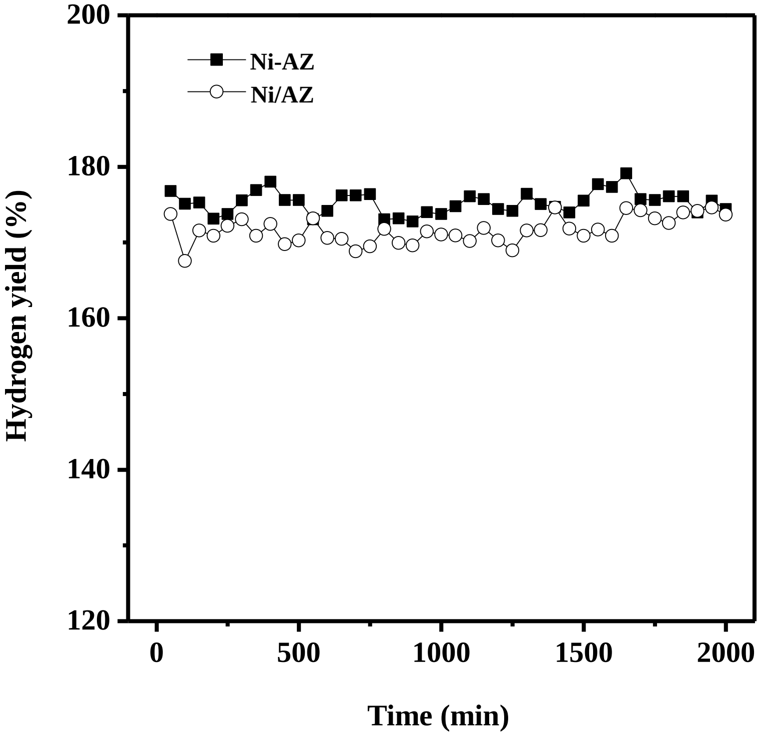

Fig. 3.27. Hydrogen yields with time on stream in the steam reforming of ethanol over Ni-AZ and Ni/AZ catalysts at 650 °C. Both catalysts were reduced at 650 °C for 3 h prior to the reaction.

3.4. Mesoporous nickel-alumina-zirconia xerogel catalyst prepared by P123-assisted sol-gel method

3.4.1. Textural properties of calcined catalysts

Nitrogen adsorption-desorption isotherms of X-NAZ catalysts are shown in Fig. 3.28. All the samples showed type-IV isotherms with H2 type hysteresis loops, indicative of bottle-shaped mesopores [104]. It is noteworthy that hysteresis pressure and adsorption volume of the catalysts increased with increasing P123 concentration. This result indicates that pore diameter and pore volume increased with increasing P123 concentration [79]. Detailed textural properties of the catalysts determined from the isotherms are given in Table 3.11. From ICP-AES result, it was revealed that nickel content of X-NAZ catalysts was in good agreement with the designed value. It was also observed that all the catalysts exhibited high surface area (300 m^2/g), large pore volume (> 0.4 cm^3/g), and large average pore diameter (> 4 nm) due to mesoporous structure. Surface area of the catalysts decreased with increasing P123 concentration, while pore volume and average pore diameter of the catalysts increased with increasing P123 concentration. It is believed that P123 in the gel structure was responsible for the formation of mesopores rather than micropores, resulting in the increase of pore volume and the decrease of surface area of the catalysts with increasing P123 concentration. Thus, X-NAZ catalysts prepared by a P123-assisted epoxide-driven sol-gel method retained enhanced mesoporosity.

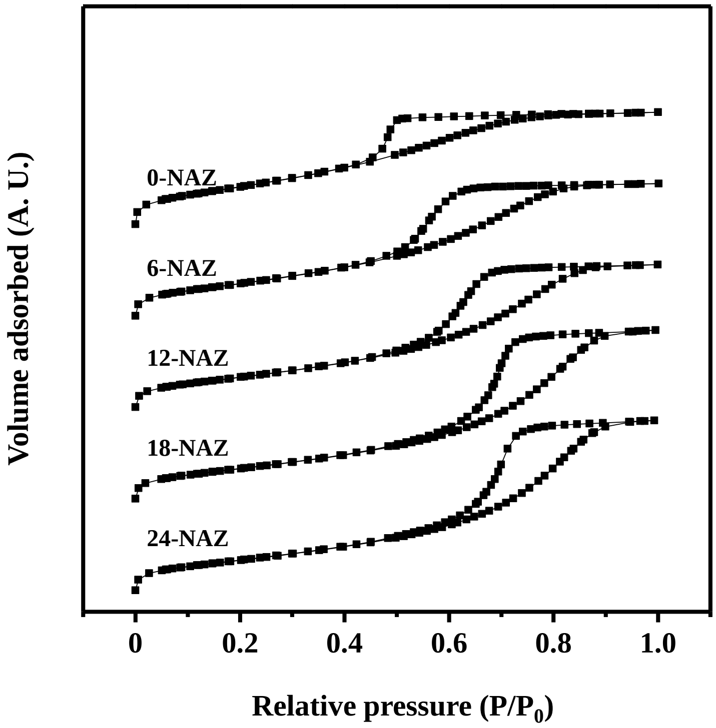

Fig. 3.28. Nitrogen adsorption-desorption isotherms of X-NAZ (X = 0, 6, 12, 18, and 24) catalysts calcined at 550 °C for 5 h.

Table 3.11

Detailed physicochemical properties of X-NAZ catalysts calcined at 550 °C for 5 h

Sample	Ni content (wt%)[a]	Surface area (m^2/g)[b]	Pore volume (cm^3/g)[c]	Average pore diameter (nm)[d]
0-NAZ	15.6	388	0.41	4.3
6-NAZ	15.6	342	0.48	5.6
12-NAZ	15.5	322	0.52	6.4
18-NAZ	15.2	319	0.60	7.6
24-NAZ	14.3	317	0.61	7.7

[a] Determined by ICP-AES measurement

[b] Calculated by the BET equation

[c] Total pore volume at P/P_0 ~ 0.995

[d] Mean pore diameter

3.4.2. Crystalline structure and reducibility

XRD patterns of X-NAZ catalysts calcined at 550 ^{o}C for 5 h are presented in Fig. 3.29(a). All the catalysts showed the weak crystalline phase of NiO, while they exhibited no crystalline phase of Al_2O_3 and ZrO_2. This indicates that amorphous Al_2O_3-ZrO_2 composite structure was formed in the X-NAZ catalysts. This is because co-existence of Al_2O_3 and ZrO_2 prohibited crystallization of individual Al_2O_3 and ZrO_2 structure by working as phase retardants.

In order to determine metal support interaction of the catalysts, TPR measurements were conducted as shown in Fig. 3.29(b). All the catalysts exhibited a single reduction peak at around 600 ^{o}C with no great difference. Judging from the XRD results of the calcined catalysts (Fig. 3.29(a)), it can be inferred that the reduction band of X-NAZ catalysts was related to the reduction of NiO interacted with Al_2O_3-ZrO_2 support.

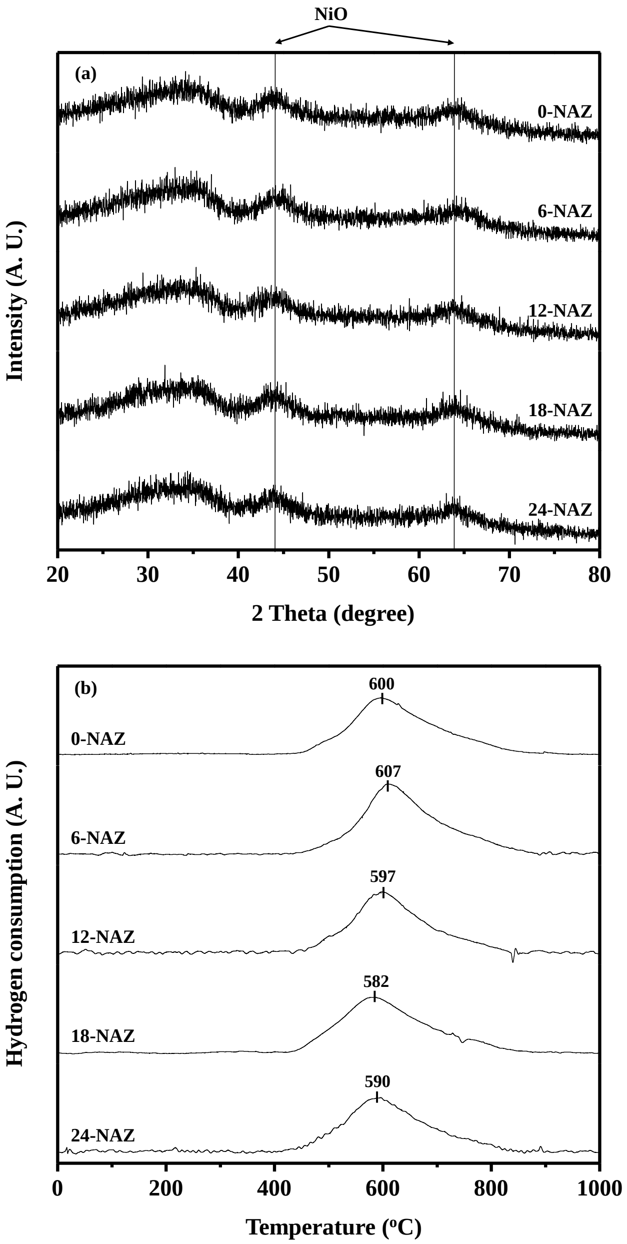

Fig. 3.29. (a) XRD patterns and (b) TPR profiles of X-NAZ (X = 0, 6, 12, 18, and 24) catalysts calcined at 550 °C for 5 h.

3.4.3. Characterization of reduced catalysts

Fig. 3.30 shows the XRD patterns of X-NAZ catalysts reduced at 650 ^{o}C. All the catalysts exhibited diffraction peaks indicative of metallic nickel, while no diffraction peaks indicative of NiO were observed. This means that NiO species in the X-NAZ catalysts were completely reduced into metallic nickel during the reduction process employed in this work. Nickel particle size of the reduced catalysts was calculated from Ni (2 0 0) peak in Fig. 3.30 using Scherrer equation as presented in Table 3.12. Nickel particle size showed a volcano-shaped trend with respect to P123 concentration. Among the catalysts, 12-NAZ catalyst retained the smallest nickel particle size. Thus, the addition of P123 strongly affected nickel dispersion of X-NAZ catalysts.

Fig. 3.31 shows the TEM images of 0-NAZ, 12-NAZ, and 24-NAZ catalysts reduced at 650 ^{o}C. It was observed that metallic nickel was well dispersed in the 12-NAZ catalyst (Fig. 3.31(b)), while metallic nickel was largely aggregated in the 0-NAZ (Fig. 3.31(a)) and 24-NAZ (Fig. 3.31(c)) catalysts.

In order to quantify the amount of hydrogen chemisorbed, H_2-TPD experiments were performed over X-NAZ catalysts as presented in Fig. 3.32. TPD profiles of the catalysts were deconvoluted into three domains of H_2 desorption peaks. Because H_2 located on the support by hydrogen spillover was responsible for desorption peak at high temperature, two domains below 600 ^{o}C were considered to calculate nickel surface area [105]. The amount of H_2 desorbed from each site was calculated from each deconvoluted area in the

H_2-TPD profiles as summarized in Table 3.13. Nickel surface area was calculated from total peak area of H_2-TPD profiles excluding the peak area above 600 ^{o}C. It is interesting to note that nickel surface area increased in the order of 0-NAZ < 6-NAZ < 24-NAZ < 18-NAZ < 12-NAZ, in good agreement with the XRD results (Fig. 3.30 and Table 3.12). Among the catalysts, 12-NAZ retained the highest nickel surface area and the smallest nickel particle size. Thus, an optimal amount of P123 was required for fine nickel dispersion in the X-NAZ catalysts prepared by an epoxide-driven sol-gel method.

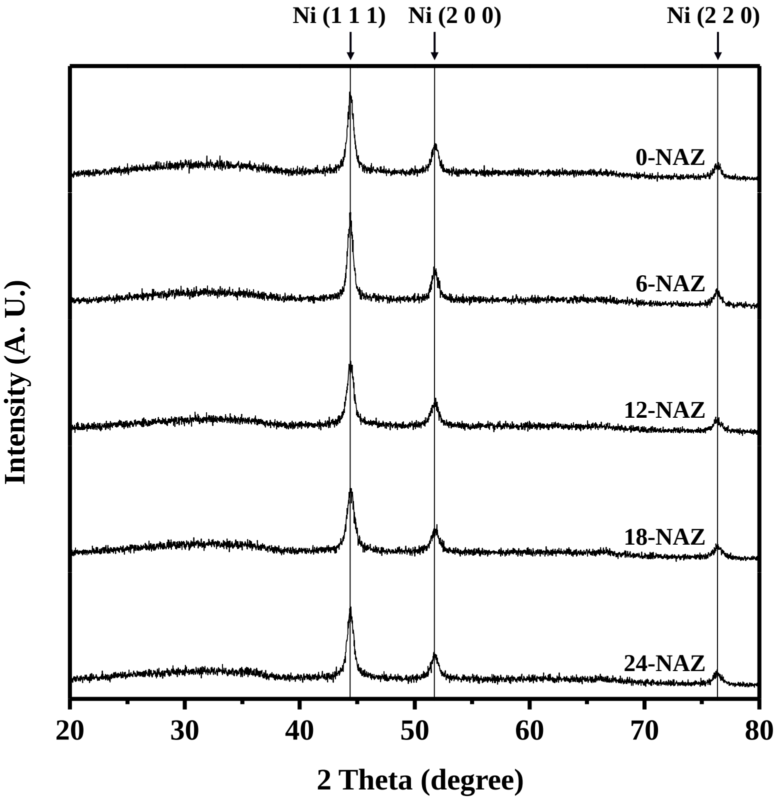

Fig. 3.30. XRD patterns of X-NAZ (X = 0, 6, 12, 18, and 24) catalysts reduced at 650 °C for 3 h.

Table 3.12

Nickel particle size of reduced X-NAZ catalysts

Catalyst	Nickel particle size (nm)[a]
0-NAZ	14.6
6-NAZ	12.7
12-NAZ	9.3
18-NAZ	10.7
24-NAZ	11.3

[a] Calculated from Ni (2 0 0) diffraction peak in Fig. 3.27.

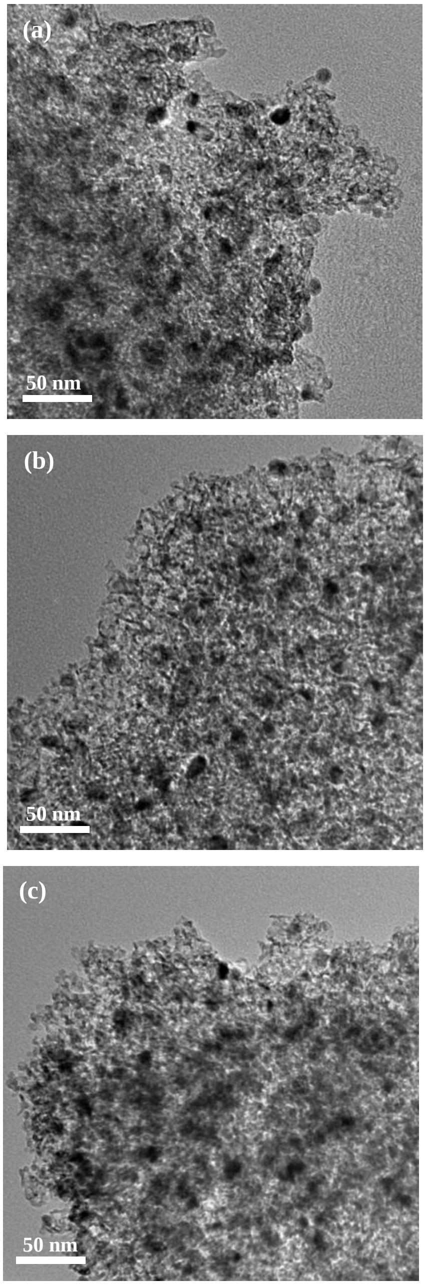

Fig. 3.31. TEM images of (a) 0-NAZ, (b) 12-NAZ, and (c) 24-NAZ catalysts reduced at 650 °C for 3 h.

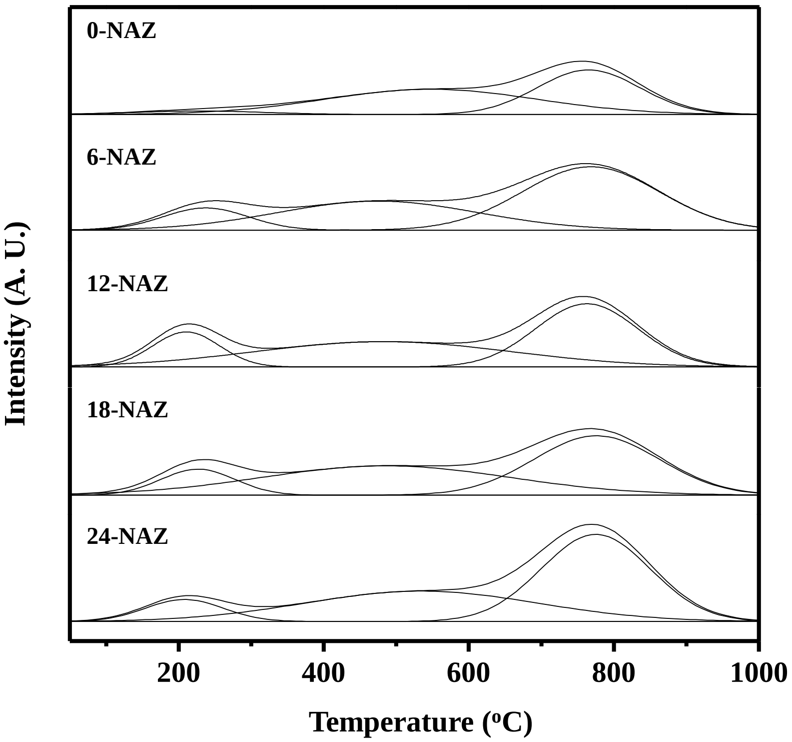

Fig. 3.32. H_2-TPD profiles of X-NAZ (X = 0, 6, 12, 18, and 24) catalysts reduced at 650 °C for 3 h.

Table 3.13

H_2-TPD results of reduced X-NAZ catalysts

Catalyst	Amount of desorbed hydrogen (μmol-H_2/g)[a]			Nickel surface area (m^2/g-Ni)[c]
	Weak site	Strong site	Total	
0-NAZ	3.1 (6.6%)[b]	43.4 (93.4%)[b]	46.5	24.2
6-NAZ	14.5 (23.4%)[b]	47.5 (76.6%)[b]	62.0	32.3
12-NAZ	21.4 (29.4%)[b]	51.4 (70.6%)[b]	72.7	37.9
18-NAZ	14.9 (21.1%)[b]	55.8 (78.9%)[b]	70.7	36.8
24-NAZ	13.3 (19.5%)[b]	54.7 (80.5%)[b]	67.9	35.4

[a] Calculated from peak area of H_2-TPD profiles in Fig. 3.32

[b] Values in parentheses are percentage of each deconvoluted area in the H_2-TPD profiles

[c] Calculated by assuming $H/Ni_{atom} = 1$

3.4.4. Ethanol adsorption study on the reduced catalysts

The affinity of nickel species toward ethanol molecule was investigated by EtOH-TPD measurements. EtOH-TPD profiles of 12-NAZ catalyst are shown in Fig. 3.33. It was observed that ethanol (m/z = 31) was molecularly desorbed at temperature up to 300 °C [106,107]. Above 250 °C, signals for carbon containing species such as methane (m/z = 16), acetaldehyde (m/z = 29), carbon monoxide (m/z = 28), and carbon dioxide (m/z = 44) were detected [108]. It is known that methane, acetaldehyde, carbon monoxide, and carbon dioxide originate from decomposition (Equation 1), dehydrogenation (Equation 2), and boudouard reaction (Equation 3) [18].

$$C_2H_5OH \leftrightarrow CH_4 + CO + H_2 \quad (\Delta H^o_{298\ K} = 49\ kJ/mol) \qquad (3.1)$$

$$C_2H_5OH \leftrightarrow C_2H_4O + H_2 \quad (\Delta H^o_{298\ K} = 68\ kJ/mol) \qquad (3.2)$$

$$2CO \leftrightarrow CO_2 \quad (\Delta H^o_{298\ K} = -171.5\ kJ/mol) \qquad (3.3)$$

It was observed that CO and CO_2 desorption peaks appeared at around 400 °C. This might be due to the carbonaceous deposits on the Ni surface and oxygen species originated from adsorbed species. Therefore, we assumed that all the adsorbed ethanol were desorbed as the carbon-containing species and the amount of adsorbed ethanol could be calculated from total amount of desorbed species. In this way, the amount of ethanol adsorbed on the X-NAZ catalysts was calculated as listed in Table 3.14. The amount of adsorbed ethanol increased in the order of 0-NAZ < 6-NAZ < 24-NAZ < 18-NAZ < 12-NAZ. It should be noted that the trend of ethanol adsorption capacity was well matched with the trend of nickel surface area (Table 3.13), demonstrating that ethanol adsorption capacity was closely related to the nickel surface area of the catalysts. Therefore, it can be inferred that the catalyst with high nickel surface area was favorable for large ethanol adsorption.

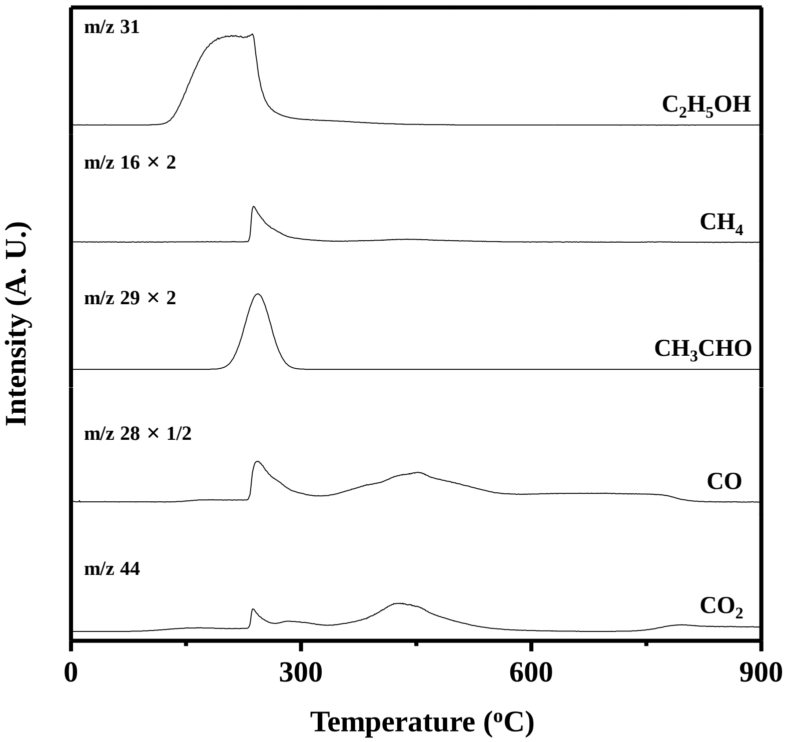

Fig. 3.33. EtOH-TPD profiles of 12-NAZ catalyst reduced at 650 °C.

Table 3.14

EtOH-TPD results for reduced X-NAZ catalysts

Catalyst	0-NAZ	6-NAZ	12-NAZ	18-NAZ	24-NAZ
Amount of ethanol adsorbed (mmol-EtOH/g)[a]	0.676	0.758	0.777	0.765	0.763

[a] Calculated from peak area of EtOH-TPD profiles

3.4.5. Catalytic performance in the steam reforming of ethanol

Fig. 3.34 shows the hydrogen yields with time on stream over X-NAZ (X = 0, 6, 12, 18, and 24) catalysts in the steam reforming of ethanol at 500 °C. X-NAZ (X = 6, 12, 18, and 24) catalysts showed a stable performance with time on stream, while 0-NAZ catalyst experienced a catalytic deactivation. It is believed that the addition of P123 improved the catalytic activity and stability by increasing pore volume and nickel surface area of the catalysts.

Table 3.15 shows the detailed catalytic performance of X-NAZ catalysts in the steam reforming of ethanol at 500 °C after a 1000 min-reaction. All the catalysts showed complete conversion of ethanol under the reaction conditions. On the other hand, hydrogen yield increased in the order of 0-NAZ < 6-NAZ < 24-NAZ < 18-NAZ < 12-NAZ. Selectivities for carbon-containing products over X-NAZ catalysts in the steam reforming of ethanol after a 1000 min-reaction were also measured as presented in Table 3.15. It is noteworthy that small amount of ethylene was formed over 0-NAZ and 6-NAZ catalysts which exhibited low hydrogen yield. Ethylene is an intermediate product formed by dehydration of ethanol ($C_2H_5OH \rightarrow C_2H_4 + H_2O$). Therefore, it can be inferred that ethylene was not completely reformed over 0-NAZ and 6-NAZ catalysts with low nickel surface area. Especially, severe deactivation of 0-NAZ catalyst might be due to the unreacted ethylene because ethylene was the main precursor of coking during the reforming reaction [76]. Methane is another intermediate product formed by decomposition of ethanol ($C_2H_5OH \rightarrow CO + CH_4 + H_2$). It was observed that selectivity for methane was relatively high in the 18-NAZ and 24-NAZ catalysts compared to 12-NAZ catalyst. CO and CO_2 were also observed over X-NAZ catalysts in the steam reforming of ethanol. However, selectivities for CO and CO_2, which were related to water-gas shift reaction ($CO + H_2O \rightarrow CO_2 + H_2$) and boudouard reaction ($2CO \rightarrow CO_2 + C$), showed no consistent trend with respect to hydrogen yield. It can be summarized that high hydrogen yield of 12-NAZ catalyst was mainly due to its high activity for reforming of ethylene and methane.

Fig. 3.35 shows the hydrogen yields over X-NAZ (X = 0, 6, 12, 18, and 24) catalysts in the steam reforming of ethanol obtained after a 1000 min-reaction, plotted as a function of P123 concentration. Hydrogen yield over X-NAZ catalysts exhibited a volcano-shaped curve with respect to P123 concentration. Hydrogen yield increased in the order of 0-NAZ < 6-NAZ < 24-NAZ < 18-NAZ < 12-NAZ. Once again, this result supports that an optimal P123 concentration was required for maximum hydrogen production by steam reforming of ethanol.

Hydrogen yields over X-NAZ (X = 0, 6, 12, 18, and 24) catalysts in the steam reforming of ethanol were correlated with nickel surface area and the amount of ethanol adsorbed as presented in Fig. 3.36. It was observed that hydrogen yield increased with increasing nickel surface area and ethanol adsorption capacity. Among the catalysts tested, 12-NAZ catalyst with the highest nickel surface area and the largest ethanol adsorption capacity exhibited the best catalytic performance in terms of hydrogen yield. Interestingly, nickel surface area and ethanol adsorption capacity showed the same trend. This is because adsorption of ethanol mainly occurred on nickel sites [107]. Furthermore, adsorption capacity of ethanol was closely related to the number of active sites where the reaction occurred. Therefore, it is summarized that high nickel surface area and large adsorption capacity of ethanol were required for high catalytic activity.

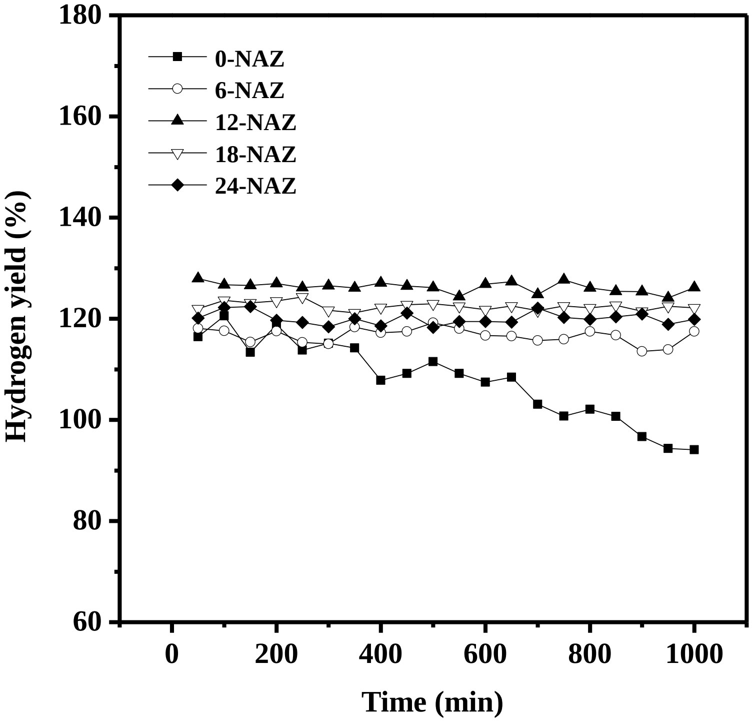

Fig. 3.34. Hydrogen yields with time on stream in the steam reforming of ethanol over X-NAZ (X = 0, 6, 12, 18, and 24) catalysts at 500 °C. All the catalysts were reduced at 650 °C for 3 h prior to the reaction.

Table 3.15

Detailed catalytic performance of X-NAZ catalysts in the steam reforming of ethanol at 500 ^{o}C after a 1000 min-reaction

Catalyst	0-NAZ	6-NAZ	12-NAZ	18-NAZ	24-NAZ
Ethanol conversion (%)	100	100	100	100	100
Hydrogen yield (%)	94	118	126	122	120
Selectivity for CH_4 (%)	22.8	23.9	24.5	24.9	27.7
Selectivity for C_2H_4 (%)	2.2	1.7	0	0	0
Selectivity for CO (%)	2.6	3.6	2.5	2.2	2.0
Selectivity for CO_2 (%)	72.4	70.8	73.0	72.9	70.2

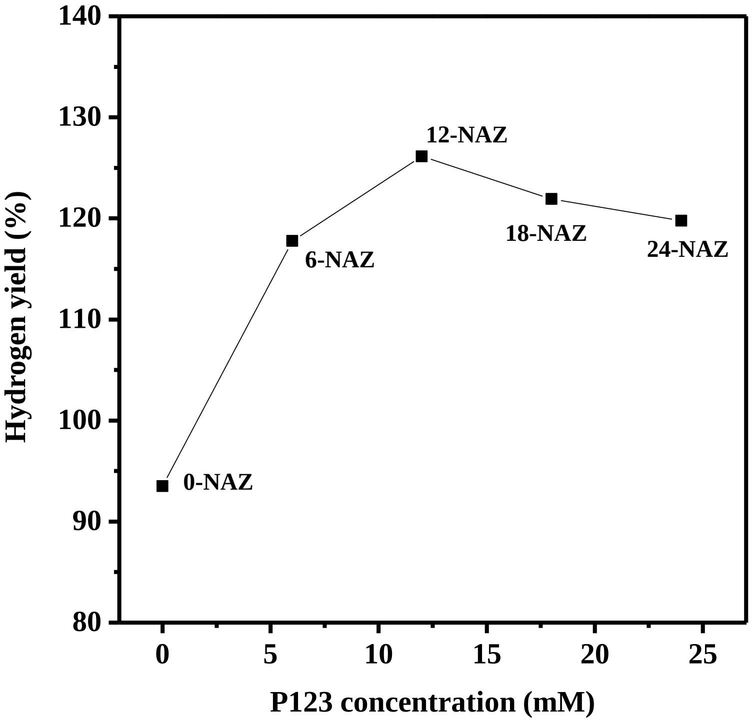

Fig. 3.35. Hydrogen yields over X-NAZ (X = 0, 6, 12, 18, and 24) catalysts in the steam reforming of ethanol obtained after a 1000 min-reaction, plotted as a function of P123 concentration.

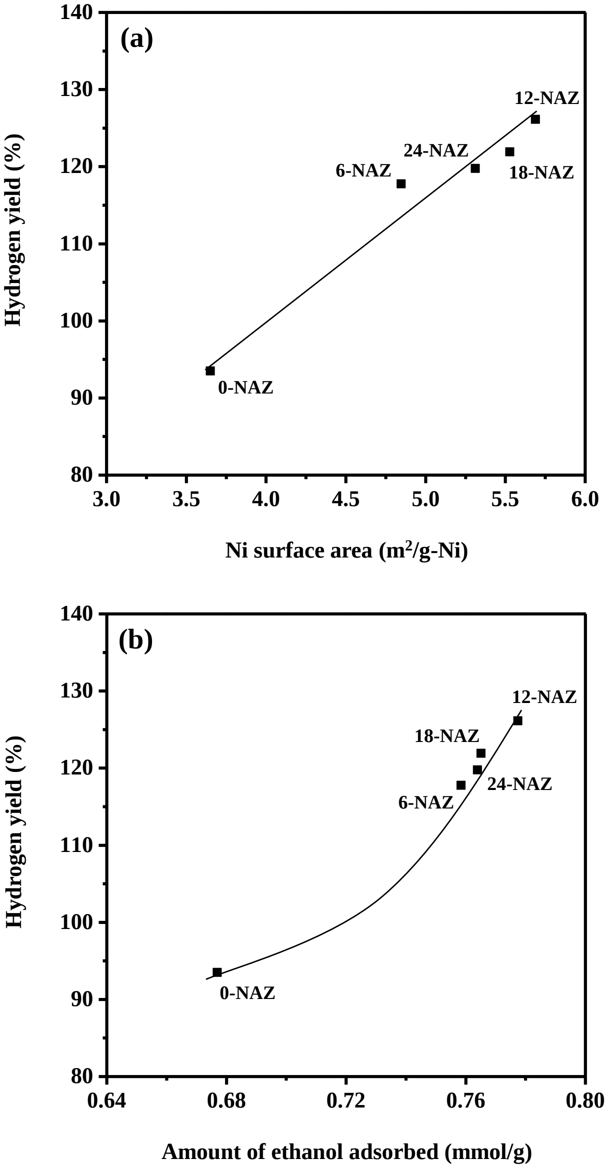

Fig. 3.36. Hydrogen yields over X-NAZ (X = 0, 6, 12, 18, and 24) catalysts in the steam reforming of ethanol obtained after a 1000 min-reaction, plotted as a function of (a) nickel surface area and (b) the amount of ethanol adsorbed.

3.5. Mesoporous copper-nickel-alumina-zirconia xerogel catalyst with various copper content

3.5.1. Characterization of calcined catalysts

Nitrogen adsorption-desorption isotherms of XCNAZ (X = 0, 0.1, 0.2, 0.3, and 1.0) catalysts are presented in Fig. 3.37(a). All the samples exhibited type-IV isotherms with H2 type hysteresis loops, which were attributed to the existence of larger pore cavity than opening [109]. It is known that conventional drying of xerogel catalysts undergoes pore shrinkage and rearrangement by liquid-vapor interfacial force [110]. Therefore, it is expected that these ink-bottle pores were formed from compaction of particulate gel structure during desiccation process. In addition, the isotherms exhibited larger adsorption volume at high relative pressure region, indicating that XCNAZ catalysts retained high mesoporosity. Detailed physicochemical properties of calcined XCNAZ catalysts are summarized in Table 3.16. From ICP-AES results, it was revealed that actual contents of Ni and Cu were well matched with the designed values. It was also observed that all the catalysts exhibited high surface area (> 240 m^2/g), large pore volume (> 0.4 cm^3/g), and large pore diameter (> 6 nm). This indicates that a mesoporous structure was successfully formed in all the catalysts. It is interesting to note that surface area of XCNAZ catalyst increased with increasing copper content. This might be due to high dissociative rate of hydrated Cu^{2+} ions. Since H_2O is the leaving group in condensation process of hydrated ions, Cu^{2+} has higher condensation rate than Al^{3+} and Ni^{2+} ions. Therefore, it is inferred that addition of Cu promoted condensation rate in the sol-gel process, which led to the production of large agglomerates. This eventually formed a highly branched gel structure with high surface area [110].

Fig. 3.37(b) shows the XRD patterns of XCNAZ catalysts calcined at 550 ^{o}C for 5 h. All the catalysts exhibited weak crystalline phases of NiO with no great difference. It is interesting to note that no crystalline phases of Al_2O_3 and ZrO_2 were observed, indicating the formation of amorphous Al_2O_3-ZrO_2 in the XCNAZ catalysts. This can be explained by the fact that co-existence of Al_2O_3 and ZrO_2 can prohibit the crystallization of Al_2O_3-ZrO_2 structure by working as phase retardants. Characteristic diffraction peaks corresponding to copper oxide were not also observed in all the XCNAZ catalysts because of relatively small amount (< 2 wt%) of copper oxide in the catalysts.

In order to determine metal-support interaction in the calcined XCNAZ catalysts, TPR measurements were conducted as presented in Fig. 3.38(a). All the XCNAZ catalysts exhibited a reduction band at around 600 ^{o}C, which was attributed to reduction of nickel oxide interacted with alumina-zirconia support. On the other hand, an additional reduction band was observed at around 350 ^{o}C in the 1.0CNAZ catalyst. The reduction band at around 350 ^{o}C might be related to the reduction of segregated copper oxide phase in the 1.0CNAZ catalyst [111]. It was also revealed that reduction peak temperature of nickel oxide decreased with increasing copper content. This is because readily reduced copper species promoted reduction of nickel oxide by transferring hydrogen during the reduction process.

The TPR results were further confirmed by XPS analyses as shown in

Fig. 3.38(b). The Ni $2p_{3/2}$ spectra for XCNAZ catalysts were deconvoluted into a main peak at 855-856 eV with a satellite at higher binding energy. It was noteworthy that binding energy of Ni $2p_{3/2}$ peak decreased with increasing copper content, in good agreement with the TPR results. Since Ni $2p_{3/2}$ peak at 855-856 eV is attributed to nickel oxide strongly interacted with support, it is inferred that metal-support interaction between nickel oxide and alumina-zirconia support decreased with increasing copper content [112]. This might be due to an increase of d hole density in nickel by charge transfer from adjacent copper [113].

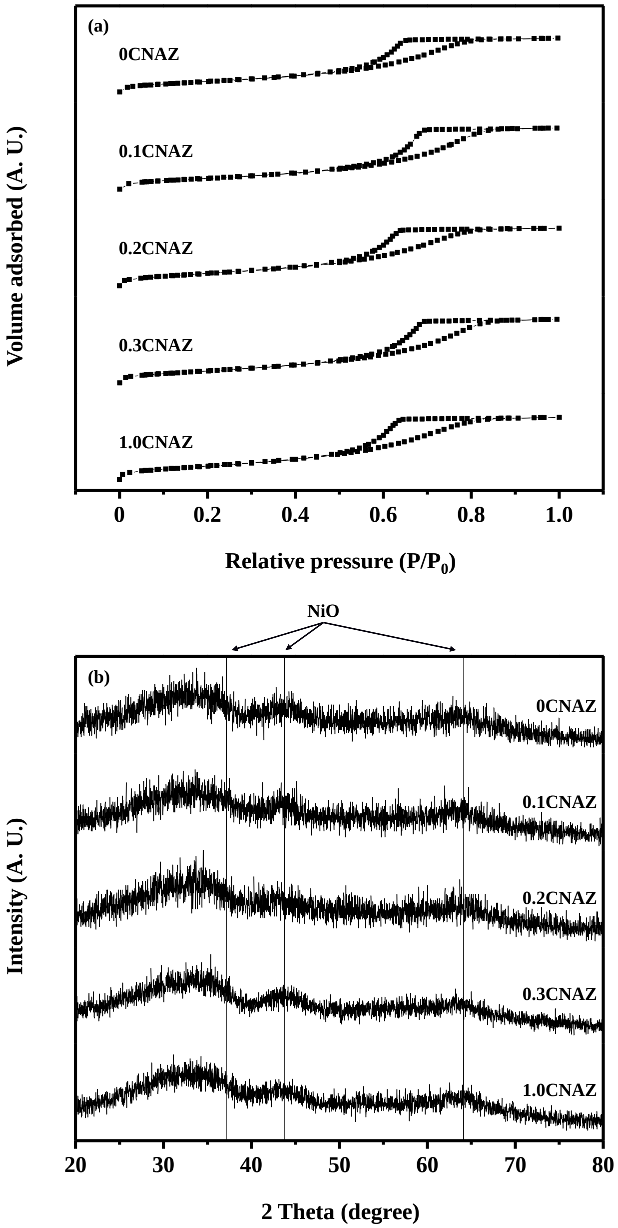

Fig. 3.37. (a) Nitrogen adsorption-desorption isotherms and (b) XRD patterns of calcined XCNAZ (X = 0, 0.1, 0.2, 0.3, and 1.0) catalysts.

Table 3.16

Detailed physicochemical properties of XCNAZ catalysts calcined at 550 °C for 5 h

Catalyst	Ni content (wt%)[a]	Cu content (wt%)[a]	Surface area (m^2/g)[b]	Pore volume (cm^3/g)[c]	Average pore diameter (nm)[d]
0CNAZ	15.3	0	246	0.40	6.5
0.1CNAZ	14.6	0.12	247	0.45	7.3
0.2CNAZ	14.1	0.17	276	0.42	6.1
0.3CNAZ	13.9	0.29	283	0.48	6.7
1.0CNAZ	14.0	1.10	295	0.45	6.2

[a] Determined by ICP-AES measurement

[b] Calculated by the BET equation

[c] Total pore volume at $P/P_0 \sim 0.995$

[d] Mean pore diameter

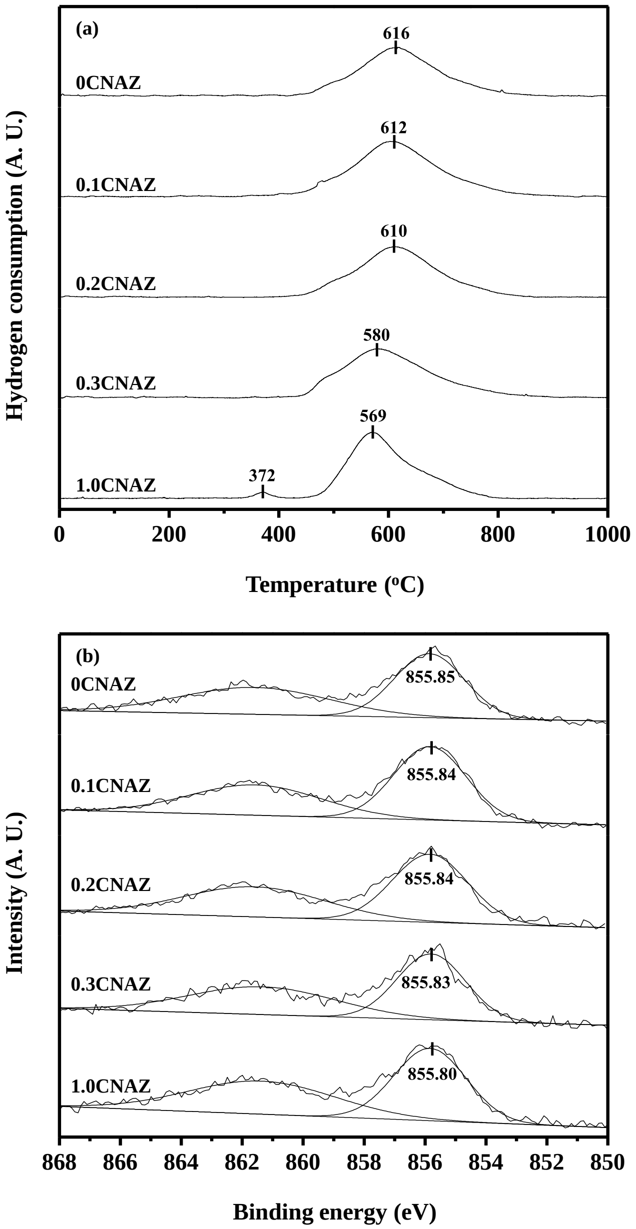

Fig. 3.38. (a) TPR profiles and (b) XPS spectra in the Ni 2p level of calcined XCNAZ (X = 0, 0.1, 0.2, 0.3, and 1.0) catalysts.

3.5.2. Characterization of reduced catalysts

Crystalline phases of XCNAZ (X = 0, 0.1, 0.2, 0.3, and 1.0) catalysts reduced at 650 ^{o}C for 3 h were examined by XRD measurements as presented in Fig. 3.39. All the catalysts exhibited diffraction peaks for metallic nickel without diffraction peaks for nickel oxide. This indicates that nickel oxide species in the XCNAZ catalysts were completely reduced during the reduction process. Crystallite sizes of metallic nickel in the reduced catalysts were calculated from Ni (1 1 1) peak in Fig. 3.39 using the Scherrer equation as listed in Table 3.17. It was revealed that crystallite size of metallic nickel decreased with increasing copper content in the reduced XCNAZ (X = 0, 0.1, and 0.2) catalysts. This might be because copper in the catalysts increased nickel dispersion by working as a spacer. However, crystallite size of metallic nickel increased with increasing copper content in the reduced XCNAZ (X = 0.3 and 1.0) catalysts. This can be explained by metal-support interaction of calcined catalysts. From the TPR and XPS results of calcined catalysts (Fig. 3.38), it was revealed that metal-support interaction between nickel oxide and alumina-zirconia support decreased with increasing copper content. Therefore, it can be inferred that 0.3CNAZ and 1.0CNAZ catalysts retained large nickel particle size because their weak metal-support interaction induced nickel particle growth during the reduction process. Accordingly, nickel particle size of reduced catalysts showed a volcano-shaped trend with respect to copper content, and 0.2CNAZ catalyst retained the smallest nickel particle size (Table 3.17).

The trend of crystallite size of metallic nickel in the reduced catalysts was further confirmed by TEM images. Fig. 3.40 shows the TEM images of 0CNAZ (Fig. 3.40(a)), 0.2CNAZ (Fig. 3.40(b)), and 1.0CNAZ (Fig. 3.40(c)) catalysts reduced at 650 ^{o}C. It was observed that metallic nickel was well dispersed in the 0.2CNAZ catalyst. While, 0CNAZ and 1.0CNAZ catalysts showed larger metallic nickel than 0.2CNAZ catalyst, which was in accordance with the XRD results.

In order to determine nickel surface area of the catalysts, H_2-TPD experiments were conducted over reduced XCNAZ catalysts as represented in Fig. 3.41. According to the literature [105], hydrogen desorption region can be classified into two regions; one is for hydrogen desorbed from exposed nickel atoms and the other is for hydrogen desorbed from subsurface layers or for hydrogen spillover. To distinguish the type of hydrogen, TPD profiles of the catalysts were deconvoluted into three domains with respect to desorption temperature. The amount of H_2 desorbed from each site was calculated from each deconvoluted area in the H_2-TPD profiles as summarized in Table 3.18. Because hydrogen desorbed from subsurface area is related to the desorption peak at high temperature ($\geq$ 600 ^{o}C), nickel surface areas of the catalysts were calculated from two domains below 600 ^{o}C. The calculated nickel surface area of the catalyst decreased in the order of 0.2CNAZ > 0.1CNAZ > 0CNAZ > 0.3CNAZ > 1.0CNAZ. Among the catalysts, 0.2CNAZ catalyst retained the highest nickel surface area due to its smallest crystallite size of metallic nickel. The smallest nickel particle size in 0.2CNAZ catalyst was attributed to the fact that addition of copper prevented aggregation of nickel species by acting as a spacer. On the other hand, the drastic decrease of nickel surface area was observed in the XCNAZ catalyst (X = 0.3 and 1.0). This can be explained by electronic effect of copper. It is known that vacancy in d-band of transition metal is a decisive factor for chemisorption [114]. Because d orbitals in copper are completely occupied with electrons, electron transfer from s orbital in copper to d orbital in nickel can reduce chemisorption ability of nickel atoms [114,115]. Therefore, it can be inferred that excess amount of copper in the XCNAZ (X = 0.3 and 1.0) catalysts reduced nickel surface area by its electronic effect. From H_2-TPD analysis, it can be summarized that an optimal amount of copper was required for high nickel surface area of XCNAZ catalyst due to geometric effect and electronic effect.

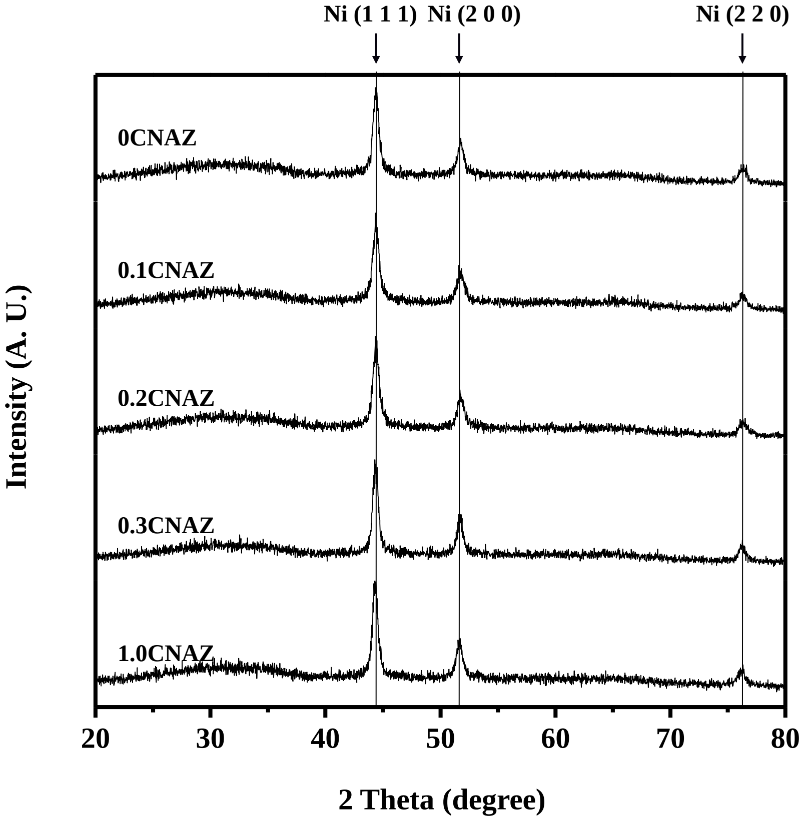

Fig. 3.39. XRD patterns of reduced XCNAZ (X = 0, 0.1, 0.2, 0.3, and 1.0) catalysts.

Table 3.17

Nickel particle size of reduced XCNAZ catalysts

Catalyst	Nickel particle size (nm)[a]
0CNAZ	14.6
0.1CNAZ	13.9
0.2CNAZ	13.6
0.3CNAZ	14.1
1.0CNAZ	14.5

[a] Calculated from Ni (1 1 1) diffraction peak in Fig. 3.39

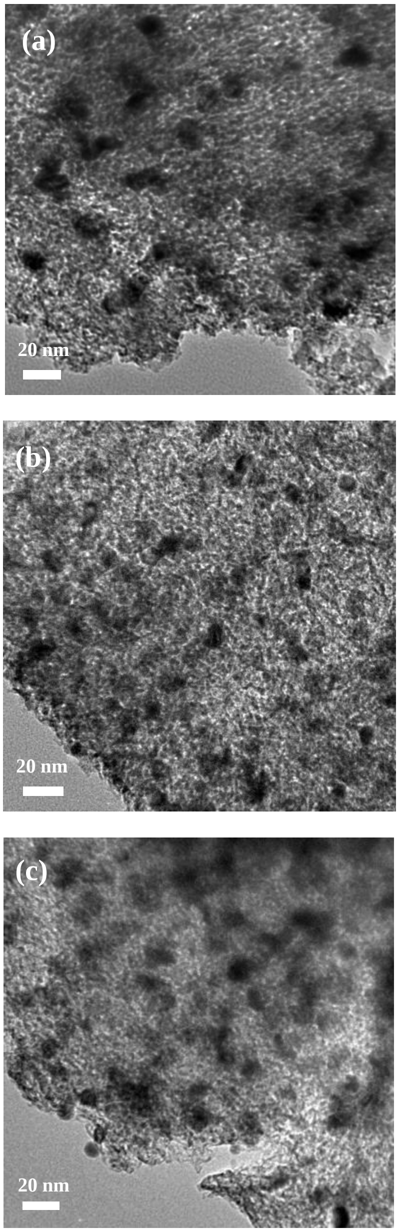

Fig. 3.40. TEM images of reduced (a) 0CNAZ, (b) 0.2CNAZ, and (c) 1.0CNAZ catalysts.

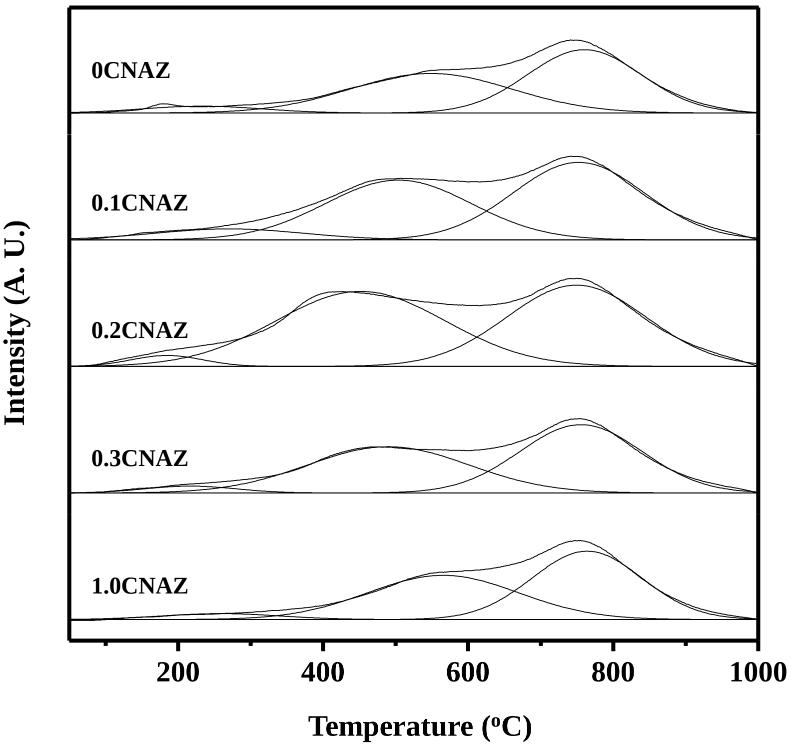

Fig. 3.41. H_2-TPD profiles of reduced XCNAZ (X = 0, 0.1, 0.2, 0.3, and 1.0) catalysts.

Table 3.18

H_2-TPD results for reduced XCNAZ catalysts

Catalyst	Amount of H_2 desorbed (μmol-H_2/g)[a]			Nickel surface area (m^2/g-Ni)[b]
	Weak site (< 300 °C)	Strong site (300-600 °C)	Total	
0CNAZ	8.4	66.2	74.6	38.8
0.1CNAZ	12.8	69.8	82.6	43.0
0.2CNAZ	5.9	95.3	101.2	52.7
0.3CNAZ	4.8	56.7	61.5	32.0
1.0CNAZ	5.1	48.3	53.4	27.8

[a] Calculated from peak area of H_2-TPD profiles in Fig. 3.41

[b] Calculated by assuming $H/Ni_{atom} = 1$

3.5.3. Ethanol adsorption study on the reduced catalysts

In order to investigate ethanol adsorption-desorption behavior of XCNAZ catalysts, EtOH-TPD measurements were conducted. Fig. 3.42 shows the EtOH-TPD spectra of 0CNAZ (Fig. 3.42(a)), 0.2CNAZ (Fig. 3.42(b)), and 1.0CNAZ (Fig. 3.42(c)) catalysts reduced at 650 ^{o}C. It was observed that EtOH-TPD spectra comprised signals for molecularly desorbed ethanol (m/z = 31), methane (m/z = 16), acetaldehyde (m/z = 29), carbon monoxide (m/z = 28), and carbon dioxide (m/z = 44). Interestingly, all the carbon-containing products exhibited desorption peaks at around 280 ^{o}C, indicating that ethanol decomposition ($C_2H_5OH \rightarrow CO + CH_4 + H_2$), ethanol dehydrogenation ($C_2H_5OH \leftrightarrow C_2H_4O + H_2$), and boudouard reaction ($2CO \leftrightarrow CO_2$) occurred concurrently during ethanol desorption. It was also found that additional desorption peaks for CO and CO_2 appeared at around 450 ^{o}C. This might be due to carbonaceous deposits on the Ni surface and oxygen species originated from adsorbed species. The amount of ethanol adsorbed was then calculated from total amount of desorbed species in the EtOH-TPD profiles as summarized in Table 3.19. The amount of adsorbed ethanol decreased in the order of 0.2CNAZ > 0.1CNAZ > 0CNAZ > 0.3CNAZ > 1.0CNAZ. This trend of ethanol adsorption capacity was well matched with the trend of nickel surface area (Table 3.18). Thus, nickel surface area was closely related to the ethanol adsorption capacity of the catalysts. In addition, it was observed that CH_3CHO/CH_4 molar ratio increased with increasing copper content. This is because copper not only promoted dehydrogenation of ethanol but also reduced C-C cleavage activity of nickel atoms [116].

Fig. 3.43 shows the in-situ FT-IR spectra obtained during EtOH-TPD over 0.2CNAZ catalyst. The bands corresponding to ethoxide species were observed at 2976 cm^{-1} (C-H stretching), 2880 cm^{-1} (C-H stretching), and 1395 cm^{-1} (C-H deformation). Intensity of these bands decreased above 200 ^{o}C, and finally, these bands disappeared at 350 ^{o}C. Acetaldehyde species, characterized by band at 1747 cm^{-1} (C=O stretching), were also detected at 200 ^{o}C. The band at 1747 cm^{-1} slightly increased upon heating to 250 ^{o}C, but it was not detected at 350 ^{o}C. This demonstrates that dehydrogenation of adsorbed ethoxide to acetaldehyde occurred at temperature window of 200-350 ^{o}C, which was in accordance with the EtOH-TPD profiles in Fig. 3.42. Above 250 ^{o}C, bands for carbonate species (1530 and 1428 cm^{-1}), carbon monoxide (2178 cm^{-1}, CO stretching), and carbon dioxide (2358 cm^{-1}, C=O stretching) were observed [117]. Judging from the mass spectroscopy and FT-IR results, therefore, it is inferred that bond breakage of ethanol on the catalyst occurred in the following order; O-H bond scission in adsorbed ethanol (ethoxide formation), C-H bond scission in adsorbed ethoxides (acetaldehyde formation), and C-C bond scission in adsorbed acetaldehyde (carbon monoxide and carbon dioxide formation).

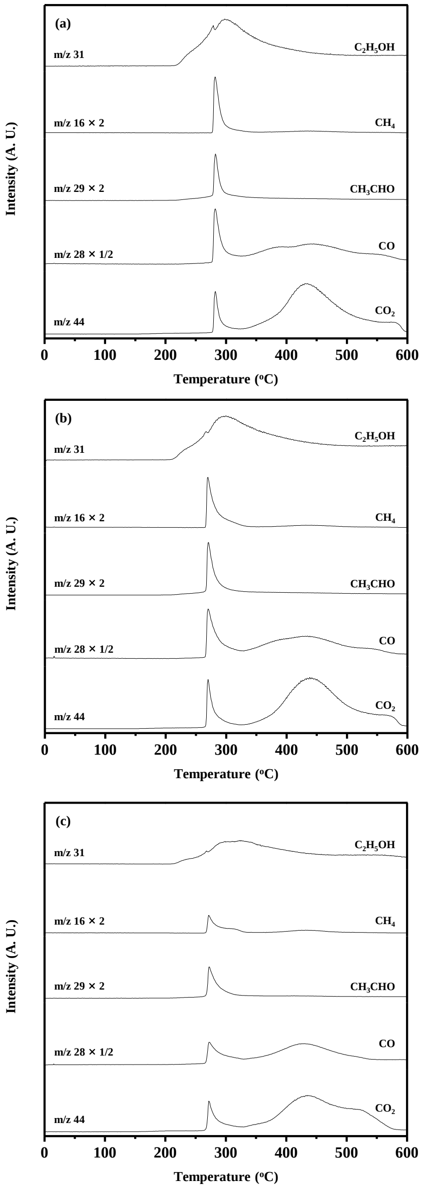

Fig. 3.42. EtOH-TPD profiles of reduced (a) 0CNAZ, (b) 0.2CNAZ, and (c) 1.0CNAZ catalysts.

Table 3.19

EtOH-TPD results for reduced XCNAZ catalysts

Catalyst	CH_3CHO/CH_4 molar ratio[a]	Amount of ethanol adsorbed (mmol/g)[a]
0CNAZ	1.27	1.97
0.1CNAZ	1.35	2.24
0.2CNAZ	1.35	2.26
0.3CNAZ	1.43	1.47
1.0CNAZ	1.71	1.32

[a] Calculated from peak area of EtOH-TPD profiles in Fig. 3.42

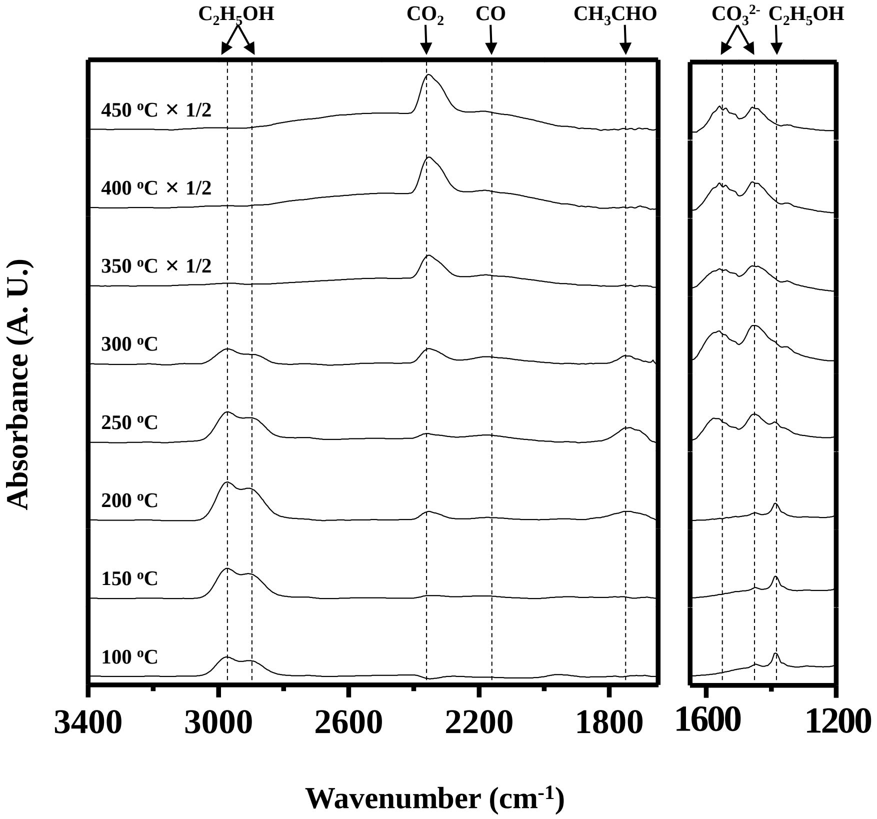

Fig. 3.43. In-situ FT-IR spectra of reduced 0.2CNAZ catalyst after ethanol adsorption at 100 °C.

3.5.4. Catalytic performance in the steam reforming of ethanol

Hydrogen yields with time on stream over XCNAZ (X = 0, 0.1, 0.2, 0.3, and 1.0) catalysts in the steam reforming of ethanol at 450 ^{o}C are presented in Fig. 3.44. All the catalysts exhibited a stable catalytic performance during a 1000 min-reaction. High stability of the catalysts might be due to their mesoporous structure and high nickel dispersion.

Table 3.20 shows the detailed catalytic performance of XCNAZ catalysts in the steam reforming of ethanol after a 1000 min-reaction. All the catalysts showed complete conversion of ethanol under the reaction condition. Carbon-containing compounds such as methane, carbon monoxide, carbon dioxide, and ethylene were produced as by-products. This indicates that additional reactions such as ethanol decomposition ($C_2H_5OH \rightarrow CH_4 + CO + H_2$) and steam reforming of ethanol to syngas ($C_2H_5OH + H_2O \rightarrow 2CO + 4H_2$) occurred during the steam reforming of ethanol. Interestingly, hydrogen yield increased and selectivity for methane decreased with increasing copper content in the XCNAZ (X = 0, 0.1, and 0.2) catalysts. This is because copper addition not only increased nickel surface area of catalyst but also induced ethanol dehydrogenation rather than ethanol decomposition. It is also known that acetaldehyde steam reforming is more favorable than methane steam reforming at low temperature. Therefore, decrease in selectivity for methane resulted in increase of hydrogen yield in the steam reforming of ethanol [18]. On the other hand, 0.3CNAZ and 1.0CNAZ catalyst exhibited relatively low hydrogen yield. This is because low nickel surface area of the catalysts was not favorable for ethylene steam reforming, methane steam reforming, and water-gas shift reaction. In particular, 1.0CNAZ catalyst produced ethylene, demonstrating that excess amount of copper decreased nickel surface area and suppressed C-C cleavage reaction in the steam reforming of ethanol.

Fig. 3.45(a) shows the hydrogen yields over XCNAZ (X = 0, 0.1, 0.2, 0.3, and 1.0) catalysts in the steam reforming of ethanol, plotted as a function of copper content. Hydrogen yield over XCNAZ catalysts showed a volcano-shaped curve with respect to copper content. This result demonstrates that an optimal copper content was required for efficient hydrogen production by steam reforming of ethanol. Hydrogen yields over XCNAZ catalysts in the steam reforming of ethanol were also correlated with nickel surface area as presented in Fig. 3.45(b). It was revealed that hydrogen yield over XCNAZ catalyst increased with increasing nickel surface area. This indicates that ethanol steam reforming reaction and related reactions mainly occurred on active nickel surface of the catalyst. Therefore, it is concluded that nickel surface area played a key role in determining the catalytic performance in the steam reforming of ethanol. Among the catalysts tested, 0.2CNAZ catalyst with the highest nickel surface area showed the highest hydrogen yield.

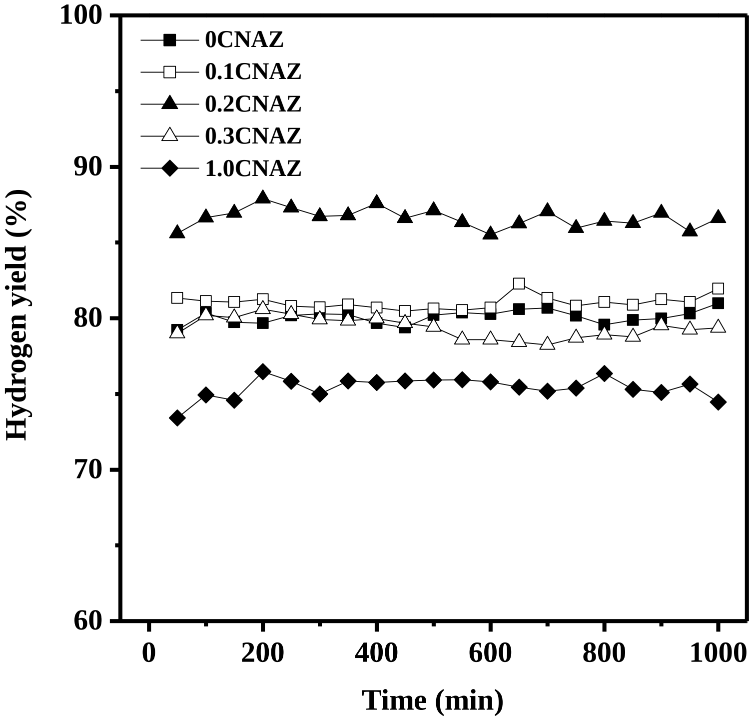

Fig. 3.44. Hydrogen yields with time on stream in the steam reforming of ethanol over XCNAZ (X = 0, 0.1, 0.2, 0.3, and 1.0) catalysts at 450 °C. All the catalysts were reduced at 650 °C for 3 h prior to the reaction.

Table 3.20

Detailed catalytic performance of XCNAZ catalysts in the steam reforming of ethanol at 450 °C after a 1000 min-reaction

Catalyst	0CNAZ	0.1CNAZ	0.2CNAZ	0.3CNAZ	1.0CNAZ
Ethanol conversion (%)	100	100	100	100	100
Hydrogen yield (%)	81.0	81.9	86.6	79.3	74.5
Selectivity for CH_4 (%)	46.1	45.7	35.9	40.1	38.6
Selectivity for C_2H_4 (%)	0	0	0	0	1.2
Selectivity for CO (%)	0	0	1.8	6.4	8.4
Selectivity for CO_2 (%)	53.9	54.3	62.3	53.4	50.7

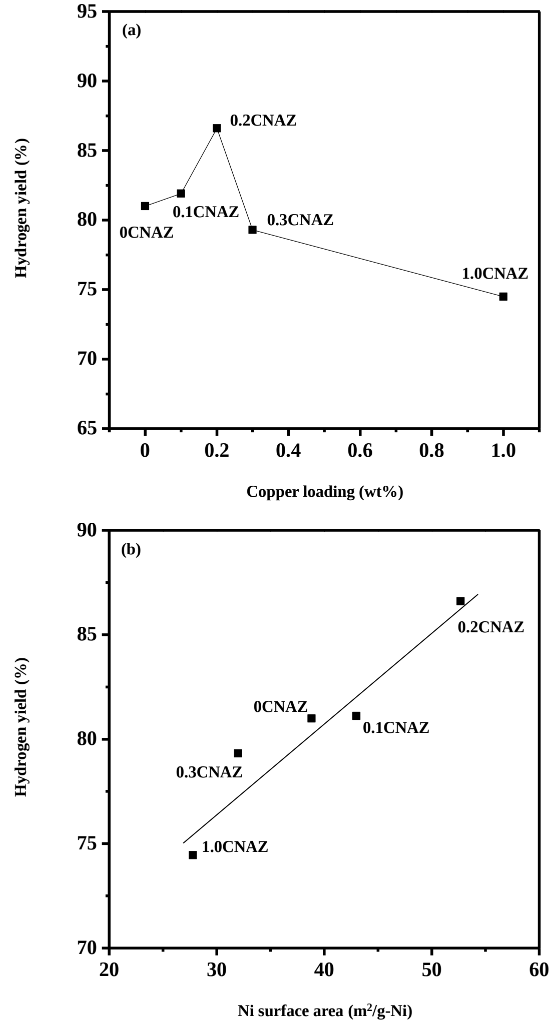

Fig. 3.45. Hydrogen yields over XCNAZ (X = 0, 0.1, 0.2, 0.3, and 1.0) catalysts in the steam reforming of ethanol obtained after a 1000 min-reaction, (a) plotted as a function of copper content and (b) plotted as a function of nickel surface area.

Chapter 4. Conclusions

Various nickel-alumina-zirconia catalysts were designed by optimization of zirconium/aluminum molar ratio, optimization of nickel content, carbon dioxide supercritical drying, P123-assisted sol-gel method, and copper addition. They were applied to the hydrogen production by steam reforming of ethanol. With various characterization techniques, the effect of physicochemical properties of catalyst on catalytic performance in the steam reforming of ethanol was investigated.

A series of mesoporous Ni-Al_2O_3-ZrO_2 (Ni-AZ-X) xerogel catalysts with different Zr/Al molar ratio (X) were prepared by a single-step epoxide-driven sol-gel method. The prepared catalysts were applied to the hydrogen production by steam reforming of ethanol. It was found that all the Ni-AZ-X catalysts exhibited a mesoporous structure. Surface area of the catalysts decreased with increasing Zr/Al molar ratio due to the incorporation of ZrO_2. Reducibility of Ni-AZ-X catalysts increased with increasing Zr/Al molar ratio through the formation of NiO-Al_2O_3-ZrO_2 composite structure. Acidity of Ni-AZ-X catalysts monotonically decreased with increasing Zr/Al molar ratio. In the hydrogen production by steam reforming of ethanol, hydrogen yields over Ni-AZ-X catalysts showed a volcano-shaped curve with respect to Zr/Al molar ratio and acidity of the catalysts. Among the catalysts tested, Ni-AZ-0.2 catalyst with an intermediate acidity exhibited the best catalytic performance in the steam reforming of ethanol.

A set of mesoporous Ni-Al_2O_3-ZrO_2 (XNiAZ) xerogel catalysts with different nickel content (X, wt%) were prepared by a single-step epoxide-driven sol-gel method. All the XNiAZ catalysts exhibited a well-developed mesoporous structure and they showed an amorphous NiO-Al_2O_3-ZrO_2 composite phase. Hydrogen yield showed a volcano-shaped trend with respect to nickel content; hydrogen yield decreased in the order of 15NiAZ > 20NiAZ > 10NiAZ > 25NiAZ > 5NiAZ. Nickel surface area served as an important factor determining the catalytic performance of XNiAZ catalysts. Among the catalysts tested, 15NiAZ catalyst with the highest nickel surface area showed the best catalytic performance. It was found that high nickel surface area promoted methane reforming reaction and enhanced resistance toward coke deposition by improving chemisorption capability of the catalyst. It is concluded that an optimal nickel content of Ni-Al_2O_3-ZrO_2 xerogel catalyst was required for maximum production of hydrogen by steam reforming of ethanol. In addition, it was found that the catalytic performance of 15NiAZ catalyst was almost constant with regard to total feed rate, demonstrating its potential applicability in large-scale hydrogen production.

A mesoporous Ni-Al_2O_3-ZrO_2 aerogel (Ni-AZ) catalyst was prepared by a single-step epoxide-driven sol-gel method and a subsequent supercritical CO_2 drying method. For comparison, a mesoporous Ni/Al_2O_3-ZrO_2 aerogel catalyst (Ni/AZ) was prepared by impregnating nickel on Al_2O_3-ZrO_2 aerogel (AZ) support. The prepared catalysts were applied to the hydrogen production by steam reforming of ethanol. It was revealed that both catalysts exhibited a well-developed mesoporous structure. Ni/AZ catalyst retained lower surface area and smaller pore volume than Ni-AZ catalyst due to pore blockage by nickel species during the impregnation step. It was also observed that Ni-AZ catalyst retained higher reducibility and higher dispersion of metallic nickel than Ni/AZ catalyst. Both Ni-AZ and Ni/AZ catalysts showed complete conversion of ethanol and stable catalytic performance in the steam reforming of ethanol. However, Ni-AZ catalyst exhibited higher hydrogen yield than Ni/AZ catalyst.

A series of mesoporous Ni-Al_2O_3-ZrO_2 (X-NAZ) xerogel catalysts were prepared by a P123-assisted epoxide-driven sol-gel method under different P123 concentration (X, mM). It was found that all the X-NAZ catalysts retained a mesoporous structure. In the hydrogen production by steam reforming of ethanol, hydrogen yield over X-NAZ catalysts showed a volcano-shaped trend with respect to P123 concentration in the order of 0-NAZ < 6-NAZ < 24-NAZ < 18-NAZ < 12-NAZ. The trend of hydrogen yield was well matched with the trend of nickel surface area and ethanol adsorption capacity. Thus, nickel surface area and ethanol adsorption capacity played key roles in determining the catalytic performance of X-NAZ catalysts in the steam reforming of ethanol. Among the catalysts tested, 12-NAZ catalyst with the highest nickel surface area and the largest ethanol adsorption capacity showed the highest hydrogen yield.

A series of mesoporous Cu-Ni-Al_2O_3-ZrO_2 (XCNAZ) xerogel catalysts with different copper content (X, wt%) were prepared by a single-step epoxide-driven sol-gel method. It was observed that all the calcined XCNAZ catalysts exhibited a mesoporous structure. It was also revealed that addition of copper increased surface area by forming a highly branched gel structure. From TPR and XPS results, it was found that addition of copper decreased metal-support interaction and enhanced reducibility of the catalysts. H_2-TPD measurements showed that nickel surface area exhibited a volcano-shaped trend with respect to copper content. Among the catalysts, 0.2CNAZ catalyst showed the highest nickel surface area and the largest ethanol adsorption capacity. In the hydrogen production by steam reforming of ethanol, hydrogen yields over XCNAZ catalysts decreased in the order of 0.2CNAZ > 0.1CNAZ > 0CNAZ > 0.3CNAZ > 1.0CNAZ. This trend of hydrogen yield was well matched with nickel surface area. Thus, nickel surface area served as an important factor determining the catalytic activity for steam reforming of ethanol. It is concluded that an optimal copper content was required for efficient hydrogen production by steam reforming of ethanol over XCNAZ catalysts.

In summary, physicochemcial properties of nickel-alumina-zirconia catalysts were modified by optimization of catalyst composition, various preparation method, and copper addition. Catalytic performance of the catalysts were closely related to several physicochemical properties such as surface area, porosity, crystalline structure, reducibility, nickel dispersion, and ethanol adsorption affinity. Especially, it was found that nickel surface area of reduced catalysts served as an important factor determining overall catalytic activity in the hydrogen production by steam reforming of ethanol. Therefore, optimal catalyst composition and preparation methods are required in order to generate highly active nickel species on the surface of nickel-alumina reforming catalyst for efficient hydrogen production.

Bibliography

[1] M. Asif, T. Muneer, “Energy supply, its demand and security issues for developed and emerging economies”, *Renew. Sustain. Energy Rev.* **11** (2007) 1388.

[2] M.S. Dresselhaus, I.L. Thomas, “Alternative energy technologies”, *Nature* **414** (2001) 332.

[3] H. Lund, “Renewable energy strategies for sustainable development”, *Energy* **32** (2007) 912.

[4] R.D. Cortright, R.R. Davda, J.A. Dumesic, “Hydrogen from catalytic reforming of biomass-derived hydrocarbons in liquid water”, *Nature* **418** (2002) 964.

[5] K. Mazloomi, C. Gomes, “Hydrogen as an energy carrier: Prospects and challenges”, *Renew. Sustain. Energy Rev.* **16** (2012) 3024.

[6] S. Sharma, S.K. Ghoshal, “Hydrogen the future transportation fuel: From production to applications”, *Renew. Sustain. Energy Rev.* **43** (2015) 1151.

[7] S.E. Hosseini, M.A. Wahid, “Hydrogen production from renewable and sustainable energy resources: Promising green energy carrier for clean development”, *Renew. Sustain. Energy Rev.* **57** (2016) 850.

[8] O.Z. Sharaf, M.F. Orhan, “An overview of fuel cell technology: Fundamentals, and applications”, *Renew. Sustain. Energy Rev.* **32** (2014) 810.

[9] R. Raza, N. Akram, M.S. Javed, A. Rafique, K. Ullah, A. Ali, M. Saleem, R. Ahmed, “Fuel cell technology for sustainable development in Pakistan-An over-view”, *Renew. Sustain. Energy Rev*. **53** (2016) 450.

[10] A. Züttel, A. Borgschulte, L. Schlapbach, “Hydrogen as a future energy carrier”, *Environ. Eng. Manage. J.* **3** (2008) 343.

[11] J.D. Holladay, J. Hu, D.L. King, Y. Wang, “An overview of hydrogen

production technologies", *Catal. Today* **139** (2009) 244.

[12] A.N. Fatsikostas, D.I. Kondarides, X.E. Verykios, "Steam reforming of biomass-derived ethanol for the production of hydrogen for fuel cell applications", *Chem. Commun.* **9** (2001) 851-852.

[13] R. Lan, J.T.S. Irvine, S. Tao, "Ammonia and related chemicals as potential indirect hydrogen storage materials", *Int. J. Hydrogen Energy* **37** (2012) 1482.

[14] M. Ni, D.Y.C. Leung, M.K.H. Leung, "A review on reforming bio-ethanol for hydrogen production", *Int. J. Hydrogen Energy* **32** (2007) 3238.

[15] H. Ma, L. Zeng, H. Tian, D. Li, X. Wang, X. Li, J. Gong, "Efficient hydrogen production from ethanol steam reforming over La-modified ordered mesoporous Ni-based catalysts", *Appl. Catal. B: Environ.* **181** (2016) 321.

[16] G. Rabenstein, V. Hacker, "Hydrogen for fuel cells from ethanol by steam-reforming, partial-oxidation and combined auto-thermal reforming: A thermodynamic analysis", *J. Power Sources* **185** (2008) 1293.

[17] I. Fishtik, A. Alexander, R. Datta, D. Geana, "A thermodynamic analysis of hydrogen production by steam reforming of ethanol via response reactions", *Int. J. Hydrogen Energy* **25** (2000) 31.

[18] P.D. Vaidya, A.E. Rodrigues, "Insight into steam reforming of ethanol to produce hydrogen for fuel cells", *Chem. Eng. J.* **117** (2006) 39.

[19] J.L. Contreras, J. Salmones, J.A. Colín-Luna, L. Nuño, B. Quintana, I. Córdova, B. Zeifert, C. Tapia, G.A. Fuentes, "Catalysts for H_2 production using the ethanol steam reforming (a review)", *Int. J. Hydrogen Energy* **39** (2014) 18835.

[20] M.C. Sánchez-Sánchez, R.M. Navarro, J.L.G. Fierro, "Ethanol steam reforming over Ni/M_xO_y-Al_2O_3 (M=Ce, La, Zr and Mg) catalysts:

Influence of support on the hydrogen production", *Int. J. Hydrogen Energy* **32** (2007) 1462.

[21] A.L. Alberton, M.M.V.M. Souza, M. Schmal, "Carbon formation and its influence on ethanol steam reforming over Ni/Al_2O_3 catalysts", *Catal. Today* **123** (2007) 257.

[22] M.E.S. Hegarty, A.M. O'Connor, J.R.H. Ross, "Syngas production from natural gas using ZrO_2-supported metals", *Catal. Today* **42** (1998) 225.

[23] S. Therdthianwong, A. Therdthianwong, C. Siangchin, S. Yongprapat, "Synthesis gas production from dry reforming of methane over Ni/Al_2O_3 stabilized by ZrO_2", *Int. J. Hydrogen Energy* **33** (2008) 991.

[24] J.G. Seo, M.H. Youn, K.M. Cho, S. Park, S.H. Lee, J. Lee, I.K. Song, "Effect of Al_2O_3-ZrO_2 xerogel support on hydrogen production by steam reforming of LNG over Ni/Al_2O_3-ZrO_2 catalyst", *Korean J. Chem. Eng.* **25** (2008) 41.

[25] J.H. Song, S.J. Han, J. Yoo, S. Park, D.H. Kim, I.K. Song, "Effect of Sr content on hydrogen production by steam reforming of ethanol over Ni-Sr/Al_2O_3-ZrO_2 xerogel catalysts", *J. Mol. Catal. A: Chemical* **418** (2016) 68.

[26] P. Biswas, D. Kunzru, "Steam reforming of ethanol on Ni-CeO_2-ZrO_2 catalysts: Effect of doping with copper, cobalt and calcium", *Catal. Lett.* **118** (2007) 36.

[27] A.F. Cunha, Y.-J. Wu, J.C. Santos, A.E. Rodrigues, "Sorption enhanced steam reforming of ethanol on hydrotalcite-like compounds impregnated with active copper", *Chem. Eng. Res. Des.* **91** (2013) 582.

[28] A.F. Cunha, Y.-J. Wu, P. Li, J.-G. Yu, A.E. Rodrigues, "Sorption-enhanced steam reforming of ethanol on a K-Cu-Ni-hydrotalcite hybrid material", *Ind. Eng. Chem. Res.* **53** (2014) 3842.

[29] S. Natesakhawat, O. Oktar, U.S. Ozkan, "Effect of lanthanide promotion on catalytic performance of sol-gel Ni/Al_2O_3 catalysts in steam reforming

of propane", *J. Mol. Catal. A: Chemical* **241** (2005) 133.

[30] J.A. Montoya, E. Romero-Pascual, C. Gimon, P.D. Angel, A. Monzón, "Methane reforming with CO_2 over Ni/ZrO_2-CeO_2 catalysts prepared by sol-gel", *Catal. Today* **63** (2000) 71.

[31] A.C. Pierre, G.M. Pajonk, "Chemistry of aerogels and their applications", *Chem. Rev.* **102** (2002) 4243.

[32] M.J. Bommel, A.B. Haan, "Drying of silica gels with supercritical carbon dioxide", *J. Mater. Sci.* **29** (1994) 943.

[33] Y. Bang, J.G. Seo, I.K. Song, "Hydrogen production by steam reforming of liquefied natural gas (LNG) over mesoporous Ni-La-Al_2O_3 aerogel catalysts: Effect of La content", *Int. J. Hydrogen Energy* **36** (2011) 8307.

[34] W. Li, Q. Yue, Y. Deng, D. Zhao, "Ordered mesoporous materials based on interfacial assembly and engineering", *Adv. Mater.* **25** (2013) 5129.

[35] Q. Yuan, A.-X. Yin, C. Luo, L.-D. Sun, Y.-W. Zhang, W.-T. Duan, H.-C. Liu, C.-H. Yan, "Facile synthesis for ordered mesoporous γ-aluminas with high thermal stability", *J. Am. Chem. Soc.* **130** (2008) 3465.

[36] Q. Yuan, L.-L. Li, S.-L. Lu, H.-H. Duan, Z.-X. Li, Y.-X. Zhu, C.-H. Yan, "Facile synthesis of Zr-based functional materials with highly ordered mesoporous structures", *J. Phys. Chem.* **113** (2009) 4117.

[37] M.E. Davis, "Ordered porous materials for emerging applications", *Nature* **417** (2002) 813.

[38] S.C. Warren, L.C. Messina, L.S. Slaughter, M. Kamperman, Q. Zhou, S.M. Gruner, F.J. DiSalvo, U. Wiesner, "Ordered mesoporous materials from metal nanoparticle-block copolymer self-assembly", *Science* **320** (2008) 1748.

[39] Y. Deng, J. Wei, Z. Sun, D. Zhao, "Large-pore ordered mesoporous materials templated from non-pluronic amphiphilic block copolymers", *Chem. Soc. Rev.* **42** (2013) 4054.

[40] G.P. Szijjártó, Z. Pászti, I. Sajó, A. Erdöhelyi, G. Radnóczi, "Nature of the

active sites in Ni/$MgAl_2O_4$-based catalysts designed for steam reforming of ethanol", *J. Catal.* **305** (2013) 290.

[41] S. Abelló, E. Bolshak, D. Montané, "Ni-Fe catalysts derived from hydrotalcite-like precursors for hydrogen production by ethanol steam reforming", *Appl. Catal. A: Gen.* **450** (2013) 261.

[42] C. Dang, H. Yu, H. Wang, F. Peng, Y. Yang, "A bi-functional Co-CaO-$Ca_{12}Al_{14}O_{33}$ catalyst for sorption-enhanced steam reforming of glycerol to high-purity hydrogen", *Chem. Eng. J.* **286** (2016) 329.

[43] S.F. Wu, Q.H. Li, J.N. Kim, K.B. Yi, "Properties of a nano CaO/Al_2O_3 CO_2 sorbent", Ind. Eng. Chem. Res. **47** (2008) 180.

[44] A.J. Vizcaíno, M. Lindo, A. Carrero, J.A. Calles, "Hydrogen production by steam reforming of ethanol using Ni catalysts based on ternary mixed oxides prepared by coprecipitation", *Int. J. Hydrogen Energy* **37** (2012) 1985.

[45] W. Wang, Y. Wang, "Steam reforming of ethanol to hydrogen over nickel metal catalysts", *Int. J. Hydrogen Energy* **34** (2010) 1285.

[46] I. Rossetti, C. Biffi, C.L. Bianchi, V. Nichele, M. Signoretto, F. Menegazzo, E. Finocchio, G. Ramis, A.D. Michele, "Ni/SiO_2 and Ni/ZrO_2 catalysts for the steam reforming of ethanol", *Appl. Catal. B: Environ.* **117** (2012) 384.

[47] P. Mărgineanu, A. Olariu, "The promoting action of chromia for nickel catalysts", *J. Catal.* **8** (1967) 359.

[48] J.G. Seo, M.H. Youn, J.S. Chung, I.K. Song, "Effect of calcinations temperature of mesoporous nickel-alumina catalysts on their catalytic performance in hydrogen production by steam reforming of liquefied natural gas (LNG)", *J. Ind. Eng. Chem.* **16** (2010) 795.

[49] H.H. Kung, E.I. Ko, "Preparation of oxide catalysts and catalyst supports - A review of recent advances", *Chem. Eng. J.* **64** (1996) 203.

[50] M. Schneider, A. Baiker, "Aerogels in catalysis", *Catal. Rev. Sci. Eng.* **37**

(1995) 515.

[51] F. Cansell, B. Chevalier, A. Demourgues, J. Etourneau, C. Even, V. Pessey, S. Petit, A. Tressaud, F. Weill, "Supercritical fluid processing: A new route for materials synthesis", *J. Mater. Chem.* **9** (1999) 67.

[52] D.W. Matson, R.D. Smith, "Supercritical fluid technologies for ceramic-processing applications", *J. Am. Ceram. Soc.* **72** (1989) 871.

[53] G.M. Pajonk, "Aerogel catalysts", *Appl. Catal.* **72** (1991) 217.

[54] J.Y. Ying, C.P. Mehnert, M.S. Wong, "Synthesis and applications of supramolecular-templated mesoporous materials" *Angew. Chem. Int. Ed.* **38** (1999) 56.

[55] U. Ciesla, F. Schüth, "Ordered mesoporous materials", *Microporous Mesoporous Mater.* **27** (1999) 131.

[56] Q. Wu, F. Zhang, J. Yang, Q. Li, B. Tu, D. Zhao, "Synthesis of ordered mesoporous alumina with large pore sizes and hierarchical structure", *Microporous Mesoporous Mater.* **143** (2011) 406.

[57] J.G. Seo, M.H. Youn, D.R. Park, J.C. Jung, I.K. Song, "Hydrogen production by steam reforming of liquefied natural gas over mesoporous Ni-Al_2O_3 composite catalyst prepared by a single-step non-ionic surfactant-templating method" *Catal. Lett.* **132** (2009) 395.

[58] A.J. Vizcaíno, A. Carrero, J.A. Calles, "Hydrogen production by ethanol steam reforming over Cu-Ni supported catalysts", *Int. J. Hydrogen Energy* **32** (2007) 1450.

[59] Y.P. Gao, C.N. Sisk, L.J. Hope-Weeks, "A sol-gel route to synthesize monolithic zinc oxide aerogels", *Chem. Mater.* **19** (2007) 6007.

[60] Y. Bang, J. Lee, S.J. Han, J.G. Seo, M.H. Youn, J.H. Song, I.K. Song, "Hydrogen production by steam reforming of liquefied natural gas (LNG) over mesoporous nickel-alumina xerogel catalysts prepared by a single-step carbon-templating sol-gel method", *Int. J. Hydrogen Energy* **37** (2012) 11208.

[61] E.J.A. Pope, J.D. Mackenzie, "Sol-gel processing of silica", *J. Non-Cryst. Solids* **87** (1986) 185.

[62] A.E. Gash, T.M. Tillotson, J.H. Satcher, L.W. Hrubesh, R.L. Simpson, "New sol-gel synthetic route to transition and main-group metal oxide aerogels using inorganic salt precursors", *J. Non-Cryst. Solids* **285** (2001) 22.

[63] S.J. Han, Y. Bang, J.G. Seo, J. Yoo, I.K. Song, "Hydrogen production by steam reforming of ethanol over mesoporous Ni-Al_2O_3-ZrO_2 xerogel catalysts: Effect of Zr/Al molar ratio", *Int. J. Hydrogen Energy* **38** (2013) 1376.

[64] C.H. Bartholomew, "Chemistry of nickel-alumina catalysts", *J. Catal.* **45** (1976) 41.

[65] P. Kim, Y. Kim, C. Kim, H. Kim, Y. Park, J.H. Lee, I.K. Song, J. Yi, "Synthesis and characterization of mesoporous alumina as a catalyst support for hydrodechlorination of 1,2-dichloropropane: effect of catalyst preparation method", *Catal. Lett.* **89** (2003) 185.

[66] A.C. Faro, K.R. Souza, V.L.D.L. Camorim, M.B. Cardoso, "Zirconia-alumina mixing in alumina-supported zirconia prepared by impregnation with solutions of zirconium acetylacetonate", *Phys. Chem. Chem. Phys.* **5** (2003) 1932.

[67] J.M. Dominguez, J.L. Hernandez, G. Sandoval, "Surface and catalytic properties of Al_2O_3-ZrO_2 solid solutions prepared by sol-gel methods", *Appl. Catal. A: Gen.* **197** (2000) 119.

[68] Y. Bang, J.G. Seo, M.H. Youn, I.K. Song, "Hydrogen production by steam reforming of liquefied natural gas (LNG) over mesoporous Ni-Al_2O_3 aerogel catalyst prepared by a single-step epoxide-driven sol-gel method", *Int. J. Hydrogen Energy* **37** (2012) 1436.

[69] M.H. Youn, J.G. Seo, J.C. Jung, S. Park, I.K. Song, "Hydrogen production by auto-thermal reforming of ethanol over nickel catalyst

supported on mesoporous yttria-stabilized zirconia", *Int. J. Hydrogen Energy* **34** (2009) 5390.

[70] E. Breval, Z. Deng, S. Chiou, C.G. Pantano, "Sol-gel prepared Ni-alumina composite materials", *J. Mater. Sci.* **27** (1992) 1464.

[71] P. Kim, J.B. Joo, H. Kim, W. Kim, Y. Kim, I.K. Song IK, J. Yi, "Preparation of mesoporous Ni-alumina catalyst by one-step sol-gel method: control of textural properties and catalytic application to the hydrodechlorination of *o*-dichlorobenzene" *Catal. Lett.* **104** (2005) 184.

[72] J.G. Seo, M.H. Youn, S. Park, J. Lee, S.H. Lee, H. Lee, I.K. Song, "Hydrogen production by steam reforming of LNG over Ni/Al_2O_3-ZrO_2 catalysts: Effect of ZrO_2 and preparation method of Al_2O_3-ZrO_2", *Korean J. Chem. Eng.* **25** (2008) 95.

[73] H. Pines, W.O. Haag, "Alumina: Catalyst and support. I. Alumina, its intrinsic acidity and catalytic activity", *J. Am. Chem. Soc.* **82** (1960) 2471.

[74] M.G. Cutrufello, I. Ferino, R. Monaci, E. Rombi, V. Solinas, "Acid-base properties of zirconium, cerium and lanthanum oxides by calorimetric and catalytic investigation", *Top. Catal.* **19** (2002) 225.

[75] W. Wang, Y.Q. Wang, "Thermodynamic analysis of steam reforming of ethanol for hydrogen generation", *Int. J. Energy Res.* **32** (2008) 1432.

[76] L.V. Mattos, G. Jacobs, B.H. Davis, F.B. Noronha, "Production of hydrogen from ethanol: Review of reaction mechanism and catalyst deactivation", *Chem. Rev.* **112** (2012) 4094.

[77] P. Djinović, J. Levec, A. Pintar, "Effect of structural and acidity/basicity changes of CuO-CeO_2 catalysts on their activity for water-gas shift reaction", *Catal. Today* **138** (2008) 222.

[78] K.S.W. Sing, D.H. Everett, R.A.W. Haul, L. Moscou, R.A. Pierotti, J. Rouquerol, T. Siemieniewska, "Reporting physisorption data for gas/solid systems with special reference to the determination of surface area and porosity", *Pure Appl. Chem.* **57** (1985) 603.

[79] S. Inamura, H. Miyamoto, Y. Imaida, M. Takagawa, K. Hirota, O. Yamaguchi, “Formation and hot isostatic pressing of ZrO_2 solid solution in the system ZrO_2-Al_2O_3”, *J. Mater. Sci.* **29** (1994) 4913.

[80] L. Gao, Q. Liu, J.S. Hong, H. Miyamoto, S.D. Torre, A. Kakitsuji, K. Liddell, D.P. Thompson, “Phase transformation in the Al_2O_3-ZrO_2 system”, *J. Mater. Sci.* **33** (1998) 1399.

[81] M. Wu, D.M. Hercules, “Studies of supported nickel catalysts by X-ray photoelectron and ion scattering spectroscopies”, *J. Phys. Chem.* **83** (1979) 2003.

[82] Z. Li, X. Hu, L. Zhang, S. Liu, G. Lu, “Steam reforming of acetic acid over Ni/ZrO_2 catalysts: Effects of nickel loading”, *Appl. Catal. A: Gen.* **417** (2012) 281.

[83] M. Zangouei, A.Z. Moghaddam, M. Arasteh, “The influence of nickel loading on reducibility of NiO/Al_2O_3 catalysts synthesized by sol-gel method”, *Chem. Eng. Res. Des.* **212** (2001) 17.

[84] H. Courbon, J.-M. Herrmann, P. Pichat, “Metal content and temperature effect on the photocatalytic isotopic exchange cyclopentane-deuterium over Pt or Ni/TiO_2 catalysts in the “normal” or “strong metal-support interaction” state”, *J. Catal.* **95** (1985) 539.

[85] J.-H. Kim, D.J. Suh, T.-J. Park, K.-L. Kim, “Effect of metal particle size on coking during CO_2 reforming of CH_4 over Ni-alumina aerogel catalysts”, *Appl. Catal. A: Gen.* **197** (2000) 191.

[86] J. Comas, F. Marioño, M. Laborde, N. Amadeo, “Bio-ethanol steam reforming on Ni/Al_2O_3 catalyst”, *Chem. Eng. J.* **98** (2004) 61.

[87] M.A. Goula, S.K. Kontou, P.E. Tsiakaras, “Hydrogen production by ethanol steam reforming over a commercial Pd/ γ-Al_2O_3 catalyst”, *Appl. Catal. B: Environ.* **49** (2004) 135.

[88] P. Biswas, D. Kunzru, “Steam reforming of ethanol for production of hydrogen over Ni/CeO_2-ZrO_2 catalyst: Effect of support and metal

loading”, *Int. J. Hydrogen Energy* **32** (2007) 969.

[89] H. Song, L. Zhang, U.S. Ozkan, “Effect of synthesis parameters on the catalytic activity of Co-ZrO_2 for bio-ethanol steam reforming”, *Green Chem.* **9** (2007) 686.

[90] A. Iulianelli, S. Liguori, T. Longo, S. Tosti, P. Pinacci, A. Basile, “An experimental study on bio-ethanol steam reforming in a catalytic membrane reactor. Part II: Reaction pressure, sweep factor and WHSV effects”, *Int. J. Hydrogen Energy* **35** (2010) 3159.

[91] J.G. Seo, M.H. Youn, Y. Bang, I.K. Song, “Hydrogen production by steam reforming of simulated liquefied natural gas (LNG) over mesoporous nickel-M-alumina (M = Ni, Ce, La, Y, Cs, Fe, Co, and Mg) aerogel catalysts”, *Int. J. Hydrogen Energy* **36** (2011) 3505.

[92] S. Cavallaro, V. Chiodo, S. Freni, N. Mondello, F. Frusteri, “Performance of Rh/Al_2O_3 catalyst in the steam reforming of ethanol: H_2 production for MCFC”, *Appl. Catal. A: Gen.* **249** (2003) 119.

[93] Z.-G. Wu, Y.-X. Zhao, D.-S. Liu, “The synthesis and characterization of mesoporous silica-zirconia aerogels”, Microporous Mesoporous Mater. **68** (2004) 127.

[94] A.C. Pierre, E. Elaloui, G.M. Pajonk, “Comparison of the structure and porous texture of alumina gels synthesized by different methods”, *Langmuir* **14** (1998) 66.

[95] S.J. Han, Y. Bang, J. Yoo, J.G. Seo, I.K. Song, “Hydrogen production by steam reforming of ethanol over mesoporous Ni-Al_2O_3-ZrO_2 xerogel catalysts: Effect of nickel content”, *Int. J. Hydrogen Energy* **38** (2013) 8285.

[96] D.J. Suh, T.-J. Park, J.-H. Kim, K.-L. Kim, “Nickel-alumina aerogel catalysts prepared by fast sol-gel synthesis”, *J. Non-Cryst. Solids* **225** (1998) 168.

[97] J. Zieliński, “Morphology of nickel/alumina catalysts”, *J. Catal.* **76**

(1982) 157.

[98] N.W. Hurst, S.J. Gentry, A. Jones, “Temperature programmed reduction”, *Catal. Rev. Sci. Eng.* **24** (1982) 233.

[99] R. Kramer, M. Andre, “Adsorption of atomic hydrogen on alumina by hydrogen spillover”, *J. Catal.* **58** (1979) 287.

[100] S. Velu, S.K. Gangwal, “Synthesis of alumina supported nickel nanoparticle catalysts and evaluation of nickel metal dispersions by temperature programmed desorption”, *Solid State Ionics* **177** (2006) 803.

[101] A. Haryanto, S. Fernando, N. Murali, S. Adhikari, “Current status of hydrogen production techniques by steam reforming of ethanol: A review”, *Energy Fuels* **19** (2005) 2098.

[102] C.H. Bartholomew, “Mechanisms of catalyst deactivation”, *Appl. Catal. A: Gen.* **212** (2001) 17.

[103] E.C. Vagia, A.A. Lemonidou, “Thermodynamic analysis of hydrogen production via steam reforming of selected components of aqueous bio-oil fraction”, *Int. J. Hydrogen Energy* **32** (2007) 212.

[104] G. Leofanti, M. Padovan, G. Tozzola, B. Venturelli, “Surface area and pore texture of catalysts”, *Catal. Today* **41** (1998) 207.

[105] S.J. Han, Y. Bang, J. Yoo, K.H. Kang, J.H. Song, J.G. Seo, I.K. Song, “Hydrogen production by steam reforming of ethanol over mesoporous Ni-Al_2O_3-ZrO_2 aerogel catalysts”, *Int. J. Hydrogen Energy* **38** (2013) 15119.

[106] P.-Y. Sheng, G.A. Bowmaker, H. Idriss, “The reactions of ethanol over Au/CeO_2”, *Appl. Catal. A: Gen.* **261** (2004) 171.

[107] A.N. Fatsikostas, X.E. Verykios, “Reaction network of steam reforming of ethanol over Ni-based catalysts”, *J. Catal.* **225** (2004) 439.

[108] Y.-J. Wu, J.C. Santos, P. Li, J.-G. Yu, A.F. Cunha, A.E. Rodrigues, “Simplified kinetic model for steam reforming of ethanol on a Ni/Al_2O_3 catalyst”, *Can. J. Chem. Eng.* **92** (2014) 116.

[109] C.L. Glaves, C.J. Brinker, D.M. Smith, P.J. Davis, “In situ pore structure studies of xerogel drying”, *Chem. Mater.* **1** (1989) 34.

[110] C.J. Brinker, K.D. Keefer, D.W. Schaefer, C.S. Ashiley, “Sol-gel transition in simple silicates”, *J. Non-Cryst. Solids* **48** (1982) 47.

[111] F. Mariño, G. Baronetti, M. Jobbagy, M. Laborde, “Cu-Ni-K/γ-Al_2O_3 supported catalysts for ethanol steam reforming: Formation of hydrotalcite-type compounds as a result of metal-support interaction”, *Appl. Catal. A: Gen.* **238** (2003) 41.

[112] L.-C. Chen, H. Cheng, C.-W. Chiang, S.D. Lin, “Sustainable hydrogen production by ethanol steam reforming using a partially reduced copper-nickel oxide catalyst”, *ChemSusChem* **8** (2015) 1787.

[113] W.M. Sachtler, P.V.D. Plank, “The role of individual surface atoms in chemisorption and catalysis by nickel-copper alloys”, *Surf. Sci.* **18** (1969) 62.

[114] A.R. Naghash, T.H. Etsell, S. Xu, “XRD and XPS study of Cu-Ni interactions on reduced copper-nickel-aluminum oxide solid solution catalysts”, *Chem. Mater.* **18** (2006) 2480.

[115] A. Ruban, B. Hammer, P. Stoltze, H.L. Skriver, J.K. Nørskov, “Surface electronic structure and reactivity of transition and noble metals”, *J. Mol. Catal. A: Chem.* **115** (1997) 421.

[116] F. Mariño, M. Boveri, G. Baronetti, M. Laborde, “Hydrogen production via catalytic gasification of ethanol. A mechanism proposal over copper-nickel catalysts”, *Int. J. Hydrogen Energy* **29** (2004) 67.

[117] A. Yee, S.J. Morrison, H. Idriss, “A study of the reactions of ethanol on CeO_2 and Pd/CeO_2 by steady state reactions, temperature programmed desorption, and in situ FT-IR”, *J. Catal.* **186** (1999) 279.

초 록

지속적인 발전을 위한 재생 가능한 대체 에너지원으로서 수소 에너지에 대한 관심이 날로 증가하고 있다. 수소 활용에 있어서 수소의 높은 에너지 밀도 및 친환경성이 주요 장점으로 작용한다. 수소 생산 기술은 크게 가열 공정(thermal process), 전기분해 공정(electrolytic process) 및 광분해 공정(photolytic process)로 분류할 수 있다. 광촉매 공정 및 전기분해 공정이 수소 생산의 궁극적인 해법으로 알려져 있으나, 대부분의 수소 생산은 화석연료인 액화천연가스(LNG)의 개질 공정을 기반으로 하고 있다. 따라서 기술의 지속성 및 연료자유도를 확보하기 위해 재생가능한 원료를 기반으로 한 수소 생산 기술의 개발이 필요하다. 이러한 상황에서, 가까운 미래에 실행가능성이 높은, 바이오매스 기반 액체연료의 개질 반응을 통한 수소 생산 기술이 연구되고 있다. 바이오매스 기반 액체연료 중 에탄올은 독성이 없고 저장하기 용이하며 생분해가 가능하다는 장점이 있어 수소 연료로서 각광을 받고 있다. 또한, 바이오 에탄올은 미래의 대체 운송수단으로 주목받고 있는 SOFC 자동차의 연료로 사용될 수 있다. 따라서 에탄올 수증기 개질 반응은 환경문제를 개선하고 지속 가능한 성장에 기여할 수 있는 유망한 기술이라고 할 수 있다.

에탄올 수증기 개질 반응에는 높은 탄소결합 분해 반응성 및 높은 가격 경쟁력을 갖는 니켈 기반 촉매가 광범위하게 사용되어 왔다. 특히 니켈/알루미나 촉매가 에탄올 수증기 개질반응에 보편적으로 이용되어 왔는데 이는 알루미나 담체의 높은 비표면적 및 높은 금속-담체 상호작용력에 기인한다. 하지만 알루미나

담체는 높은 산특성을 가지고 있어 탄소침적의 원인이 되는 에탄올 탈수반응을 유도한다는 단점이 있다. 이에 니켈/알루미나 촉매의 활성 및 반응안정성을 증진시키기 위해 담체 물질을 변형하는 시도가 있어왔다. 마그네슘 옥사이드 및 칼슘 옥사이드 같은 알칼리 토금속 산화물을 조촉매로 도입하면 알루미나의 산점을 중화시켜 탄소침적을 줄여준다는 보고가 있다. 또한 란타넘족 산화물을 도입하면 니켈 표면의 탄소 가스화 반응을 촉진시켜 줌으로써 촉매의 활성을 증진시킬 수 있다. 특히 지르코늄 옥사이드는 촉매의 반응안정성을 증진시킬 뿐만 아니라 물의 흡착 및 해리를 촉진하기 때문에 에탄올 수증기 개질 반응 상에서 니켈/알루미나 촉매의 효과적인 조촉매로 알려져 있다.

본 연구에서는, 에탄올 수증기 개질 반응에서 효과적인 촉매를 개발하기 위해 중형기공성 니켈-알루미나-지르코니아 촉매를 제조하였으며, 에폭사이드 기반 졸-겔법, 촉매 조성의 최적화, 이산화탄소 초임계 건조법, 주형물질의 도입 및 구리의 도입 등 다양한 촉매 제조법에 의해 촉매를 물리화학적으로 개선하였다.

먼저, 다양한 지르코늄/알루미늄 몰 비(X)를 갖는 중형기공성 니켈-알루미나-지르코니아 제로젤 촉매(Ni-AZ-X)를 단일공정 에폭사이드 기반 졸-겔법으로 제조하고, 제조된 촉매를 에탄올 수증기 개질 반응에 적용하였다. 촉매의 비표면적은 지르코늄/알루미늄 몰 비가 증가할수록 감소하는 경향을 나타내었다. 니켈 옥사이드 종과 담체의 상호작용력은 지르코늄/알루미늄 몰 비가 증가할수록 니켈-알루미나-지르코니아 복합 종 형성을 통해 감소하였다. 또한 지르코늄/알루미늄 몰 비 가 증가할수록 촉매의 산량이 감소하였는데 이는 첨가된 지르코늄 옥사이드가 알루미나의

산점을 중화시켰기 때문으로 판단된다. 에탄올 수증기 개질 반응에서 제조된 촉매 중 적절한 산량을 갖는 Ni-AZ-0.2 (Zr/Al=0.2) 촉매에서 가장 우수한 활성을 나타내었다.

다양한 니켈 함량(X, wt%)을 니켈-알루미나-지르코니아 촉매(XNiAZ)를 단일공정 에폭사이드 기반 졸-겔법을 통해 제조하였다. 모든 XNiAZ 촉매가 발달된 중형기공구조를 나타내었으며, $NiO-Al_2O_3-ZrO_2$ 복합상이 형성되어 높은 니켈 옥사이드 분산도를 나타내었다. XNiAZ 촉매의 니켈 표면적 및 환원성은 니켈 함량에 따라 화산형 곡선을 나타내었다. 에탄올 수증기 개질 반응에서 제조된 촉매 중 가장 높은 니켈 표면적을 갖는 15NiAZ 촉매가 가장 우수한 활성을 나타내었다.

단일공정 에폭사이드 기반 졸-겔법 및 이산화탄소 초임계 건조법에 의해 중형기공성 니켈-알루미나-지르코니아 에어로젤 촉매(Ni-AZ)를 제조하였다. 비교를 위해 중형기공성 알루미나-지르코니아 에어로젤 담체(AZ)를 에폭사이드 기반 졸-겔법 및 이산화탄소 초임계 건조법을 통해 제조한 뒤 습윤 함침법을 통해 중형기공성 니켈/알루미나-지르코니아 촉매(Ni/AZ)를 제조하였다. 두 촉매 모두 중형기공성을 나타내었으며, Ni/AZ 촉매가 Ni-AZ 촉매에 비해 더 작은 비표면적을 나타내었다. TPR, XRD 및 H_2-TPD 분석을 통해 Ni-AZ 촉매가 Ni/AZ 촉매에 비해 높은 환원성 및 니켈 분산도를 갖는다는 것을 확인하였다. 에탄올 수증기 개질 반응에서 높은 물리적 특성, 높은 환원성 및 높은 니켈 표면적을 갖는 Ni-AZ 촉매가 Ni/AZ 촉매에 비해 우수한 활성을 나타내었다.

다양한 농도(X, mM)의 P123 이 도입된 에폭사이드 기반 졸-겔법을 통해 중형기공성 니켈-알루미나-지르코니아 제로젤

촉매(X-NAZ)를 제조하였다. 모든 촉매가 중형기공구조를 형성하였으며, P123 의 농도가 증가할수록 촉매의 기공부피가 증가하였다. X-NAZ 촉매의 니켈 표면적 및 에탄올 흡착능력은 P123 농도에 따라 화산형 경향성을 나타내었다. 에탄올 수증기 개질 반응에서, 제조된 촉매 중 가장 높은 니켈 표면적 및 에탄올 흡착능력을 갖는 12-NAZ 촉매에서 가장 우수한 활성을 나타내었다.

다양한 구리 함량(X, wt%)을 갖는 중형기공성 구리-니켈-알루미나-지르코니아 제로젤 촉매(XCNAZ)를 단일공정 에폭사이드 기반 졸-겔법을 통해 제조하고, 제조된 촉매를 에탄올 수증기 개질 반응에 적용하였다. 제조된 모든 촉매가 중형기공 구조를 나타내었으며, 구리의 함량이 증가할수록 비표면적이 증가하는 경향성을 나타내었다. 금속-지지체 상호작용력은 구리 함량이 증가할수록 감소하였는데 이는 구리의 전자적 효과에 기인한다. 제조된 촉매 중 0.2CNAZ 촉매가 가장 높은 니켈 표면적 및 에탄올 흡착능력을 나타내었다. 에탄올 수증기 개질 반응에서 촉매의 활성은 구리의 함량에 따라 화산형 곡선을 나타내었으며, 가장 높은 니켈 표면적을 가진 0.2CNAZ 촉매가 가장 우수한 활성을 나타내었다.

요약하자면, 본 연구에서는 물리화학적으로 개선된 다양한 니켈-알루미나-지르코니아 촉매를 제조하고 이를 에탄올 수증기 개질 반응을 통한 수소 생산 반응에 적용하였다. 촉매의 물리화학적 특성이 에탄올 수증기 개질반응 활성에 미치는 영향을 규명하기 위해 질소 흡탈착 분석, XRD, TPR, TEM, H_2-TPD, EtOH-TPD 및 in-situ FT-IR 등의 다양한 특성 분석 기법이 수행되었다.

결과적으로, 촉매의 니켈 표면적이 에탄올 수증기 개질 반응을 통한 수소 생산에서의 촉매 활성을 결정짓는 주요 인자라는 것이 밝혀졌다.

주요어: 수소 생산, 에탄올의 수증기 개질, 니켈 촉매, 에폭사이드 기반 졸–겔법, 이산화탄소 초임계 건조, 구리 첨가, 제로젤, 에어로젤

학　번: 2012-20983

List of publications

Papers

International papers published (First author)

1. **S.J. Han**, J.H. Song, J. Yoo, S. Park, K.H. Kang, I.K. Song, "Sorption-enhanced Hydrogen Production by Steam Reforming of Ethanol over Mesoporous Co/CaO-Al_2O_3 Xerogel Catalysts: Effect of Ca/Al Molar Ratio", *International Journal of Hydrogen Energy* (In Press).

2. **S.J. Han**, J.H. Song, Y. Bang, J. Yoo, S. Park, K.H. Kang, I.K. Song, "Hydrogen Production by Steam Reforming of Ethanol over Mesoporous Cu-Ni-Al_2O_3-ZrO_2 Xerogel Catalysts", *International Journal of Hydrogen Energy*, 41(4), pp.2554-2563 (2016).

3. **S.J. Han**, Y. Bang, J.H. Song, J. Yoo, S. Park, K.H. Kang, I.K. Song, "Hydrogen Production by Steam Reforming of Ethanol over Dual-templated Ni-Al_2O_3 Catalyst", *Catalysis Today*, 265, pp.103-110 (2016).

4. **S.J. Han**, Y. Bang, H. Lee, K. Lee, I.K. Song, J.G. Seo, "Synthesis of a Dual Templated MgO-Al_2O_3 Using Block Copolymer and Ionic Liquid for CO_2 Capture", *Chemical Engineering Journal*, 270, pp.411-417 (2015) .

5. **S.J. Han**, Y. Bang, J. Yoo, S. Park, K.H. Kang, J.H. Choi, J.H. Song, I.K. Song, "Hydrogen Production by Steam Reforming of Ethanol over P123-assisted Mesoporous Ni-Al_2O_3-ZrO_2 Xerogel Catalysts", *International Journal of Hydrogen Energy*, 39(20), pp.10445-10453 (2014).

6. **S.J. Han**, Y. Bang, H.J. Kwon, H.C. Lee, V. Hiremath, I.K. Song, J.G. Seo, "Elevated Temperature CO_2 Capture on Nano-Structured MgO-Al_2O_3 Aerogel:

Effect of Mg/Al Molar Ratio”, *Chemical Engineering Journal*, 242, pp.357-363 (2014).

7. **S.J. Han**, Y. Bang, J. Yoo, K.H. Kang, J.H. Song, J.G. Seo, I.K. Song, “Hydrogen Production by Steam Reforming of Ethanol over Mesoporous Ni-Al_2O_3-ZrO_2 Aerogel Catalysts”, *International Journal of Hydrogen Energy*, 38(35), pp.15119-15127 (2013).

8. **S.J. Han**, Y. Bang, J. Yoo, J.G. Seo, I.K. Song, “Hydrogen Production by Steam Reforming of Ethanol over Mesoporous Ni-Al_2O_3-ZrO_2 Xerogel Catalysts: Effect of Nickel Content”, *International Journal of Hydrogen Energy*, 38(20), pp.8285-8292 (2013).

9. **S.J. Han**, Y. Bang, J.G. Seo, J. Yoo, I.K. Song, “Hydrogen Production by Steam Reforming of Ethanol over Mesoporous Ni-Al_2O_3-ZrO_2 Xerogel Catalysts: Effect of Zr/Al Molar Ratio”, *International Journal of Hydrogen Energy*, 38(3), pp.1376-1383 (2013).

International papers published (Co-author)

1. S. Park, **S.J. Han**, J. Yoo, J.H. Song, E.J. Lee, I.K. Song, “Hydrogen Production by Steam Reforming of Liquefied Natural Gas (LNG) over Nickel-iron-alumina Aerogel Catalyst”, *Journal of Nanoscience and Nanotechnology* (In Press).

2. M.Y. Gim, **S.J. Han**, T.H. Kang, J.H. Song, T.H. Kim, D.H. Kim, K-Y. Lee, I.K. Song, “BTX Production by Direct Dehydroaromatization of Methane over WOx/HZSM-5 Catalysts”, *Journal of Nanoscience and Nanotechnology* (In Press).

3. J.H. Song, **S.J. Han**, J. Yoo, S. Park, D.H. Kim, I.K. Song, “Hydrogen Production by Steam Reforming of Ethanol over Ni-Sr-Al_2O_3-ZrO_2 Aerogel Catalyst”, *Journal of Molecular Catalysis A: Chemical*, 424, pp.342-350 (2016).

4. K.H. Kang, **S.J. Han**, J.W. Lee, T.H. Kim, I.K. Song, “Effect of Boron Content on 1,4-Butanediol Production by Hydrogenation of Succinic Acid over Re-Ru/BMC (Boron-modified Mesoporous Carbon) Catalysts”, *Applied Catalysis A: General*, 524, pp.206-213 (2016).

5. J.H. Song, **S.J. Han**, J. Yoo, S. Park, D.H. Kim, I.K. Song, “Effect of Sr Content on Hydrogen Production by Steam Reforming of Ethanol over Ni-Sr/Al_2O_3-ZrO_2 Xerogel Catalysts”, *Journal of Molecular Catalysis A: Chemical*, 418-419, pp.68-77 (2016).

6. J.H. Song, J.O. Jun, K.H. Kang, **S.J. Han**, J. Yoo, S. Park, D.H. Kim, I.K. Song, “Synthesis of Dimethyl Carbonate from Propylene Carbonate and Methanol over Y_2O_3/CeO_2-La_2O_3 Catalysts”, *Journal of Nanoscience and Nanotechnology*, 16(10), pp.10810-10815 (2016).

7. J. Yoo, Y. Bang, **S.J. Han**, S. Park, J.H. Song, I.K. Song, “Hydrogen Production by Steam Reforming of Liquefied Natural Gas (LNG) over Magnesium-doped Nickel-alumina Aerogel Catalyst”, *Journal of Nanoscience and Nanotechnology*, 16(10), pp.10835-10840 (2016).

8. J.H. Song, **S.J. Han**, J. Yoo, S. Park, D.H. Kim, I.K. Song, “Hydrogen Production by Steam Reforming of Ethanol over Ni-X/Al_2O_3-ZrO_2 (X=Mg, Ca, Sr, and Ba) Xerogel Catalysts: Effect of Alkaline Earth Metal Addition”, *Journal of Molecular Catalysis A: Chemical*, 415, pp.151-159 (2016).

9. Y. Bang, S. Park, **S.J. Han**, J. Yoo, J.H. Choi, T.H. Kang, J. Lee, I.K, Song, “Hydrogen Production by Steam Reforming of Liquefied Natural Gas (LNG) over Nickel-phosphorus-alumina Xerogel Catalyst Prepared by a Carbon-

templating Epoxide-driven Sol-gel Method", *Journal of Nanoscience and Nanotechnology*, 16(5), pp.4605-4611 (2016).

10. Y. Bang, S. Park, **S.J. Han**, J. Yoo, J.H. Song, J.H. Choi, K.H. Kang, I.K. Song, "Hydrogen Production by Steam Reforming of Liquefied Natural Gas (LNG) over Mesoporous Ni/Al_2O_3 Catalyst Prepared by an EDTA-assisted Impregnation Method", *Applied Catalysis B: Environmental*, 180, pp.179-188 (2016).

11. J. Yoo, Y. Bang, **S.J. Han**, S. Park, J.H. Song, I.K. Song, "Hydrogen Production by Tri-reforming of Methane over Nickel-alumina Aerogel Catalyst", *Journal of Molecular Catalysis A: Chemical*, 410, pp.74-80 (2015).

12. S. Park, Y. Bang, **S.J. Han**, J. Yoo, J.H. Song, J.C. Song, J. Lee, I.K. Song, "Hydrogen Production by Steam Reforming of Liquefied Natural Gas (LNG) over Mesoporous Nickel-iron-alumina Catalyst", *International Journal of Hydrogen Energy*, 40(17), pp.5869-5877 (2015).

13. K.H. Kang, J.O. Jun, **S.J. Han**, K. Kwon, O.-S. Kwon, B. Jang, I.K. Song, "Direct Synthesis of Diphenyl Carbonate from Phenol and Carbon Dioxide over Ti-salen-based Catalysts", *Journal of Nanoscience and Nanotechnology*, 15(10), pp.8353-8358 (2015).

14. K.H. Kang, U.G. Hong, Y. Bang, J.H. Choi, J.K. Kim, J.K. Lee, **S.J. Han**, I.K. Song, "Hydrogenation of Succinic Acid to 1,4-Butanediol over Re-Ru Bimetallic Catalysts Supported on Mesoporous Carbon", *Applied Catalysis A: General*, 490, pp.153-162 (2015).

15. K.H. Kang, U.G. Hong, J.O. Jun, J.H. Song, Y. Bang, J.H. Choi, **S.J. Han**, I.K. Song, "Hydrogenation of Succinic Acid to γ-Butyrolactone and 1,4-Butanediol over Mesoporous Rhenium-copper-carbon Composite Catalyst", *Journal of Molecular Catalysis A: Chemical*, 395, pp.234-242 (2014).

16. Y. Bang, **S.J. Han**, S. Kwon, V. Hiremath, I.K. Song, J.G. Seo, “High Temperature Carbon Dioxide Capture on Nano-structured $MgO\text{-}Al_2O_3$ and $CaO\text{-}Al_2O_3$ Adsorbents: An Experimental and Theoretical Study”, *Journal of Nanoscience and Nanotechnology*, 14(11), pp.8531-8538 (2014).

17. Y. Bang, **S.J. Han**, J. Yoo, S. Park, J.H. Choi, Y.J. Lee, J.H. Song, I.K. Song, “Hydrogen Production by Steam Reforming of Liquefied Natural Gas (LNG) over Mesoporous Nickel-phosphorus-alumina Aerogel Catalyst”, *International Journal of Hydrogen Energy*, 39(10), pp.4909-4916 (2014).

18. Y. Bang, **S.J. Han**, J. Yoo, J.H. Choi, J.K. Lee, J.H. Song, J. Lee, I.K. Song, “Hydrogen Production by Steam Reforming of Simulated Liquefied Natural Gas (LNG) over Nickel Catalyst Supported on Mesoporous Phosphorus-modified Alumina Xerogel”, *Applied Catalysis B: Environmental*, 148-149, pp.269-280 (2014).

19. J. Yoo, Y. Bang, **S.J. Han**, T.H. Kang, J. Lee, I.K. Song, “Hydrogen Production by Steam Reforming of Liquefied Natural Gas (LNG) over Mesoporous Alkaline Earth Metal-promoted Nickel-alumina Xerogel Catalysts”, *Journal of Molecular Catalysis A: Chemical*, 380, pp.28-33 (2013).

20. Y. Bang, **S.J. Han**, J. Yoo, J.H. Choi, K.H. Kang, J.H. Song, J.G. Seo, J.C. Jung, I.K. Song, “Hydrogen Production by Steam Reforming of Liquefied Natural Gas (LNG) over Trimethylbenzene-assisted Ordered Mesoporous Nickel-alumina Catalyst”, *International Journal of Hydrogen Energy*, 38(21), pp.8751-8758 (2013).

21. Y. Bang, **S.J. Han**, J.G. Seo, M.H. Youn, J.H. Song, I.K. Song, “Hydrogen Production by Steam Reforming of Liquefied Natural Gas (LNG) over Ordered Mesoporous Nickel-alumina Catalyst”, *International Journal of Hydrogen Energy*, 37(22), pp.17967-17977 (2012).

22. Y. Bang, J. Lee, **S.J. Han**, J.G. Seo, M.H. Youn, J.H. Song, I.K. Song,

“Hydrogen Production by Steam Reforming of Liquefied Natural Gas (LNG) over Mesoporous Nickel-alumina Xerogel Catalysts Prepared by a Single-step Carbon-templating Sol-gel Method”, *International Journal of Hydrogen Energy*, 37(15), pp.11208-11217 (2012).

Patents

Registered patents

1. 송인규, **한승주**, 방용주, 유재경, 박승원. 이현주, “이온성 액체를 이용한 중형기공성 니켈-알루미나 촉매의 제조, 그 촉매 및 상기 촉매를 이용한 수소가스 제조 방법”, 대한민국 특허출원 10-2015-0024318, 대한민국특허 제 1,659,264 호 (2016).

2. 송인규, 방용주, 박승원, **한승주**, 유재경, 이현주, “알루미나 담체에 화학적으로 고정화된 니켈 촉매, 그 제조 방법 및 상기 촉매를 이용한 액화천연가스의 수증기 개질 반응에 의한 수소 가스 제조 방법”, 대한민국 특허출원 10-2014-0181396, 대한민국특허 제 1,636,055 호 (2016).

3. 송인규, 박승원, 방용주, **한승주**, 유재경, 이현주, “중형기공성 니켈-철-알루미나 제로젤 촉매, 그 제조 방법 및 상기 촉매를 이용한 액화천연가스의 수증기 개질 반응에 의한 수소 가스 제조 방법”, 대한민국 특허출원 10-2014-0157965, 대한민국특허 제 1,628,695 호 (2016).

4. 송인규, 방용주, **한승주**, 유재경, 이현주, “중형기공성 니켈-인-알루미나 에어로젤 촉매, 그 제조 방법 및 상기 촉매를 이용한 액화천연가스의 수증기 개질 반응에 의한 수소 가스 제조 방법”, 대한민국 특허출원 10-2013-0117889 (2013), 대한민국특허 제 1,460,348 호 (2014).

5. 송인규, 방용주, **한승주**, 유재경, 이현주, “인을 포함한 중형기공성 알루미나 제어로젤 담체에 담지된 니켈 촉매, 그 제조 방법 및 상기

촉매를 이용한 액화천연가스의 수증기 개질 반응에 의한 수소가스 제조 방법", 대한민국 특허출원 10-2013-0108834, 대한민국특허 제 1,512,505 호 (2015).

6. 송인규, **한승주**, 방용주, 이현주, "중형기공성 니켈-알루미나-지르코니아 제어로젤 촉매 및 상기 촉매를 이용한 에탄올의 수증기 개질 반응에 의한 수소가스 제조 방법", 대한민국 특허출원 10-2012-0097393, 대한민국특허 제 1,392,996 호 (2014).

7. 이현주, 송인규, 죄준환, 방용주, **한승주**, "나노 탄소 입자를 주형 물질로 사용하여 제조된 중형기공성 니켈-알루미나 제어로젤 촉매, 그 제조 방법 및 상기 촉매를 이용한 액화천연가스(LNG)의 수증기 개질 반응에 의한 수소가스 제조 방법", 대한민국 특허출원 10-2012-0003937, 대한민국특허 제 1,405,306 호 (2014).

Applied patents

1. 송인규, 김민영, **한승주**, 송창열, 김도희, 이관영, "메탄 및 프로판의 탈수소방향족화 반응을 위한 미세기공과 중형기공이 혼재된 HZSM-5 에 담지된 메탈 옥사이드 촉매의 제조방법 및 상기 촉매를 이용한 BTX 제조방법", 대한민국 특허출원 10-2016-0171251 (2016).

2. 송인규, **한승주**, 유재경, 박승원, 송지환, "중형기공성 칼슘옥사이드-알루미나 제로젤 담체에 담지된 코발트 촉매, 그 제조 방법 및 상기 촉매를 이용한 에탄올의 수증기 개질 반응에 의한 수소가스 제조 방법", 대한민국 특허출원 10-2016-0095933 (2016).

3. 송인규, 박승원, **한승주**, 유재경, 송지환, "중형기공성 니켈-붕소-

알루미나 제로젤 촉매, 그 제조 방법 및 상기 촉매를 이용한 액화천연가스의 수증기 개질 반응에 의한 수소 가스 제조 방법", 대한민국 특허출원 10-2016-0061001 (2016).

4. 송인규, **한승주**, 유재경, 박승원, 송지환, 이현주, "단일공정 졸-겔(Sol-gel)법으로 제조된 중형기공성 니켈-구리-알루미나-지르코니아 제로젤 촉매, 그 제조 방법 및 상기 촉매를 이용한 에탄올의 수증기 개질 반응에 의한 수소가스 제조 방법", 대한민국 특허출원 10-2015-0144560 (2015).

Conferences

International conferences (First author)

1. **S.J. Han**, Y. Bang, J.H. Song, J. Yoo, S. Park, K.H. Kang, I.K. Song, "Hydrogen Production by Steam Reforming of Ethanol over Dual-templated Ni-Al_2O_3 Catalyst", *NANO KOREA 2015*, P1503_097, COEX, Seoul, Korea (2015/7/1-3).

2. **S.J. Han**, Y. Bang, S. Park, K.H. Kang, J.H. Choi, J.H. Song, I.K. Song, "Ethanol Steam Reforming over P123-assisted Mesoporous Ni-Al_2O_3-ZrO_2 Xerogel Catalysts", *The 15th Korea-Japan Symposium on Catalysis*, YO A14, Busan, Korea (2015/05/26-28).

3. **S.J. Han**, Y. Bang, J. Yoo, I.K. Song, "Hydrogen Production by Steam Reforming of Ethanol over Mesoporous Ni-Al_2O_3-ZrO_2 Aerogel Catalyst", *20th WHEC (World Hydrogen Energy Conference) 2014*, 56, Kwangju, Korea (2014/6/15-20).

4. **S.J. Han**, Y. Bang, V. Hiremath, I.K. Song, J.G. Seo, "Synthesis of Mesoporous MgO-Al_2O_3 Adsorbents for CO_2 Capture Using Block Copolymers and Ionic Liquids", *NANO KOREA 2014*, P1403_008, COEX, Seoul, Korea (2014/7/2-4).

5. **S.J. Han**, Y. Bang, J. Yoo, K.H. Kang, J.H. Song, J.G. Seo, I.K. Song, "Ethanol Steam Reforming over a Mesoporous Ni-Al_2O_3-ZrO_2 Aerogel Catalyst", *Seventh Tokyo Conference on Advanced Catalytic Science and Technology*, GP2035, Kyoto, Japan (2014/6/1-6).

6. **S.J. Han**, Y. Bang, J. Yoo, I.K. Song, "Ethanol Steam Reforming over a Mesoporous Ni-Al_2O_3-ZrO_2 Xerogel Catalysts", *International Conference on Hydrogen Production - 2014*, P-44, Fukuoka, Japan (2014/2/2-5).

7. **S.J. Han**, Y. Bang, H. Kang, I.K. Song, J.G. Seo, "CO_2 Physicochemical Adsorption on the Hierarchically Mesoporous MgO-Al_2O_3 Adsorbents with Bimodal Pore System", *NANO Korea 2013 Symposium*, P1303_035, Coex, Seoul, Korea (2013/7/10-12).

8. **S.J. Han**, Y. Bang, J.G. Seo, J. Yoo, I.K. Song, "Hydrogen Production by Steam Reforming of Ethanol over Mesoporous Ni-Al_2O_3-ZrO_2 Xerogel Catalysts: Effect of Zr/Al Molar Ratio", *The 4th International Conference on New & Renewable Energy 2013*, P2-11, Daegu. Korea (2013/3/28-30).

International conferences (Co-author)

1. S. Park, T.H. Kim, E.J. Lee, **S.J. Han**, J. Yoo, J.H. Song, I.K. Song, "Mesoporous Nickel-iron-alumina Catalysts for Hydrogen Production by Steam Reforming of Liquefied Natural Gas (LNG)", *The 16th International Congress on Catalysis*, PC066, Beijing, China (2016/07/3-8).

2. M.Y. Gim, **S.J. Han**, T.H. Kang, J.H. Song, T.H. Kim, I.K. Song, "BTX Production by Direct Dehydroaromatization of Methane over WO_x/HZSM-5 Catalysts", *NANO KOREA 2016*, P1605_0544, KINTEX, Korea (2016/7/13-15).

3. S. Park, **S.J. Han**, J. Yoo, J.H, Song, E.J. Lee, I.K. Song, "Hydrogen Production by Steam Reforming of Liquefied Natural Gas (LNG) over Nickel-iron-alumina Aerogel Catalyst", *NANO KOREA 2016*, P1605_0546, KINTEX, Korea (2016/7/13-15).

4. J. Yoo, Y. Bang, **S.J. Han**, T.H. Kang, I.K. Song, "Alkaline Earth Metal-promoted Nickel-alumina Xerogel Catalysts for Hydrogen Production by Steam Reforming of Natural Gas", *APCChE 2015 Congress*, P-3126273,

Melbourne, Australia (2015/09/27-2015/10/01).

5. K.H. Kang, T.H. Kim, J.K. Lee, **S.J. Han**, W.C. Choi, Y.-K. Park, I.K. Song, "Dehydrogenation of Propane to Propylene over Cr-based Catalysts", *NANO KOREA 2015*, P1503_101, COEX, Seoul, Korea (2015/7/1-3).

6. J. Yoo, Y. Bang, **S.J. Han**, S. Park, J.H. Song, I.K. Song, "Hydrogen Production by Steam Reforming of Liquefied Natural Gas (LNG) over Magnesium-doped Nickel-alumina Aerogel Catalyst", *NANO KOREA 2015*, P1503_105, COEX, Seoul, Korea (2015/7/1-3).

7. J.H. Song, J.O. Jun, K.H. Kang, **S.J. Han**, J. Yoo, S. Park, D.H. Kim, I.K. Song, "Synthesis of Dimethyl Carbonate from Propylene Carbonate and Methanol over $Y_2O_3/CeO_2-La_2O_3$ Catalysts", *NANO KOREA 2015*, P1503_098, COEX, Seoul, Korea (2015/7/1-3).

8. J. Yoo, Y. Bang, **S.J. Han**, S. Park, J.H. Song, I.K. Song, "Methane Tri-reforming over Nickel-alumina Aerogel Catalyst", *The 15th Korea-Japan Symposium on Catalysis*, GP43, Busan, Korea (2015/05/26-28).

9. K.H. Kang, J.K. Kim, J.K. Lee, **S.J. Han**, I.K. Song, "Re-Ru Bimetallic Catalysts for Hydrogenation of Succinic Acid to 1,4-Butanediol", *The 15th Korea-Japan Symposium on Catalysis*, GP59, Busan, Korea (2015/05/26-28).

10. Y. Bang, **S.J. Han**, J. Yoo, J.H. Choi, J.K. Lee, I.K. Song, "Hydrogen Production by Steam Reforming of Liquefied Natural Gas (LNG) over Nickel Catalyst Supported on Mesoporous Phosphorus-modified Alumina Xerogel", *20th WHEC(World Hydrogen Energy Conference) 2014*, 58, Kwangju, Korea (2014/6/15-20).

11. J. Yoo, Y. Bang, **S.J. Han**, T.H. Kang, I.K. Song, "Hydrogen Production by Steam Reforming of Liquefied Natural Gas (LNG) over Mesoporous Alkaline Earth Metal-promoted Nickel-alumina Xerogel Catalysts", *20th WHEC(World*

Hydrogen Energy Conference) 2014, 52, Kwangju, Korea (2014/6/15-20).

12. K.H. Kang, J.O. Jun, **S.J. Han**, K. Kwon, O.-S. Kwon, B. Jang, I.K. Song, “Direct Synthesis of Diphenyl Carbonate from Phenol and Carbon Dioxide over Ti-salen-based Catalysts”, *NANO KOREA 2014*, P1403_168, COEX, Seoul, Korea (2014/7/2-4).

13. Y. Bang, **S.J. Han**, J. Yoo, S. Park, J.H. Choi, J. Lee, I.K. Song, “Hydrogen Production by Steam Reforming of LNG over Nickel-phosphorus-alumina Catalyst Prepared by a Templating Sol-gel Method”, *NANO KOREA 2014*, P1406_001, COEX, Seoul, Korea (2014/7/2-4).

14. K.H. Kang, J.O. Jun, **S.J. Han**, K. Kwon, D.B. Kim, Y. Lee, O.-S. Kwon, I.K. Song, “Direct Synthesis of Diphenyl Carbonate from Methanol and Carbon Dioxide over Metal-Salen Catalysts”, *Seventh Tokyo Conference on Advanced Catalytic Science and Technology*, GP2028, Kyoto, Japan (2014/6/1-6).

15. Y. Bang, **S.J. Han**, J. Yoo, J.H. Choi, K.H. Kang, I.K. Song, “Preparation of Structure-modified Ordered Mesoporous Nickel-alumina Catalyst for Hydrogen Production by Steam Reforming of Liquefied Natural Gas (LNG)”, *International Conference on Hydrogen Production - 2014*, P-45, Fukuoka, Japan (2014/2/2-5).

16. J. Yoo, Y. Bang, **S.J. Han**, T.H. Kang, I.K. Song, “Effect of Promoter on Nickel-alumina Xerogel Catalyst for Hydrogen Production by Steam Reforming of Liquefied Natural Gas (LNG)”, *International Conference on Hydrogen Production - 2014*, P-43, Fukuoka, Japan (2014/2/2-5).

17. Y. Bang, **S.J. Han**, H.J. Kwon, S. Kwon, H.C. Lee, I.K. Song, J.G. Seo, “High Temperature Carbon Dioxide Capture on Nano-structured Alkaline-earth Metal Oxide Adsorbent”, *NANO Korea 2013 Symposium*, P1303_034, Coex, Seoul, Korea (2013/7/10-12).

18. Y. Bang, J. Lee, **S.J. Han**, J.G. Seo, I.K. Song, "Hydrogen Production by Steam Reforming of LNG over Mesoporous Nickel-alumina Xerogel Catalysts Prepared by a Carbon-templating Method", *The 9th World Congress of Chemical Engineering (The 15th Asian Pacific Confederation Chemical Engineering Congress)*, P-01-136, COEX, Korea (2013/8/18-23).

19. Y. Bang, **S.J. Han**, J.G. Seo, J. Yoo, I.K. Song, "Hydrogen Production by Steam Reforming of Liquefied Natural Gas (LNG) over Ordered Mesoporous Nickel-alumina Catalyst", *The 4th International Conference on New & Renewable Energy 2013*, P2-9, Daegu. Korea (2013/3/28-30).

20. Y. Bang, J.G. Seo, M.H. Youn, **S.J. Han**, I.K. Song, "Hydrogen Production by Steam Reforming of Liquefied Natural Gas (LNG) over Mesoporous Ni-Al_2O_3 Aerogel Catalyst", *The 15th International Congress on Catalysis*, 6607, Munich, Germany (2012/07/1-7).

Domestic conferences (First author)

1. **한승주**, 송지환, 유재경, 박승원, 강기혁, 송인규, "정렬된 중형기공을 갖는 니켈-알루미나-지르코니아 상의 에탄올의 수증기 개질 반응을 통한 수소 가스 생산", 2016 년 한국화학공학회 추계학회, P 촉매금-82, 대전 DCC (2016/10/19-21).

2. **한승주**, 송지환, 유재경, 박승원, 강기혁, 송인규, "칼슘이 도입된 중형기공성 코발트-알루미나 제로겔 촉매의 제조 및 에탄올 수증기 개질 반응으로의 적용", 2016 년 한국화학공학회 춘계학회, P 촉매금-80, 부산 BEXCO (2016/4/27-29).

3. **한승주**, 송지환, 유재경, 박승원, 강기혁, 송인규. "스피넬 구조를

갖는 복합 알루미나 담체에 담지된 코발트 촉매 상의 에탄올 수증기 개질 반응을 통한 수소 가스 생산”, 2015 년 한국화학공학회 추계학술회의, P 촉매금-9, 일산 KINTEX (2015/10/21-23).

4. **한승주**, 방용주, 유재경, 박승원, 송지환, 송인규, “단일공정 에폭사이드 기반 졸-겔법을 통해 제조된 니켈-구리-알루미나-지르코니아 제로젤 촉매를 이용한 에탄올 수증기 개질 반응에 대한 연구”, 2015 년 한국화학공학회 춘계학술회의, P 촉매목-5, 제주 ICC (2015/4/22-24).

5. **한승주**, 방용주, 유재경, 박승원, 송인규, “P123 과 이온성 액체가 주형물질로 도입된 중형기공성 니켈-알루미나 촉매 제조 및 에탄올 수증기 개질 반응으로의 적용”, 2014 년 한국화학공학회 추계학술회의, P 촉매금-4, 대전 DCC (2014/10/22-24).

6. **한승주**, 방용주, 유재경, 서정길, 송인규, “P123 이 도입된 졸겔법을 통한 니켈-알루미나-지르코니아 제로젤 촉매 제조 및 에탄올 수증기 개질 반응으로의 적용”, 2014 년 한국공업화학회 춘계학술회의, 1P-254, 제주 ICC (2014/4/30-5/2).

7. **한승주**, 방용주, 유재경, 서정길, 송인규, “P123 이 도입된 중형기공성 니켈-알루미나-지르코니아 제로젤 촉매 상에서 에탄올 수증기 개질 반응을 통한 수소 가스 생산”, 2014 년 한국화학공학회 춘계학술회의, P 촉매금-67, 창원 컨벤션센터 (2014/4/23-25).

8. **한승주**, 방용주, 유재경, 서정길, 송인규, “에탄올 수증기 개질 반응에서 니켈-알루미나-지르코니아 촉매에 도입된 계면활성제가 반응 활성에 미치는 영향”, 2013 년 한국공업화학회 추계학술회의, 2P-174, 대전 컨벤션센터 (2013/10/30-11/1).

9. **한승주**, 방용주, 유재경, 서정길, 송인규. “계면활성제가 도입된 중형기공성 니켈-알루미나-지르코니아 제로젤 촉매 상에서 에탄올 수증기 개질 반응을 통한 수소 가스 생산”, 2013 년 한국화학공학회 추계학술회의, P 촉매목-3, 대구 EXCO (2013/10/23-25).

10. **한승주**, 방용주, 유재경, 서정길, 송인규, “초임계 건조를 통해 제조한 니켈-알루미나-지르코니아 에어로젤 촉매의 에탄올 수증기 개질 반응으로의 적용”, 2013 년 한국공업화학회 춘계학술회의, 1P-401, 제주 국제컨벤션센터 (2013/5/1-3).

11. **한승주**, 방용주, 유재경, 서정길, 송인규, “중형기공성 니켈-알루미나-지르코니아 에어로젤 촉매 상에서 에탄올 수증기 개질 반응을 통한 수소 가스 생산”, 2013 년 한국화학공학회 춘계학술회의, P 촉매금-6, 광주 김대중컨벤션센터 (2013/4/24-26).

12. **한승주**, 방용주, 유재경, 서정길, 윤민혜, 송인규, “에탄올 수증기 개질반응에서 중형기공성 니켈-알루미나-지르코니아 촉매의 니켈 담지량이 반응 활성에 미치는 영향”, 2012 년 한국공업화학회 추계학술회의, 2P-176, 대전컨벤션센터 (2012/10/31-11/2).

13. **한승주**, 방용주, 유재경, 서정길, 윤민혜, 송인규, “단일공정 에폭사이드 기반 졸-겔법을 통해 제조된 니켈-알루미나-지르코니아 제어로젤 촉매를 이용한 에탄올 수증기 개질반응에 대한 연구”, 2012 년 한국화학공학회 추계학술회의, P 촉매수-12, 부산 BEXCO (2012/10/24-26).

14. **한승주**, 방용주, 서정길, 윤민혜, 송인규, “에폭사이드 기반 졸-겔 법을 통한 중형기공성 알루미나-지르코니아에 담지된 니켈 촉매의 제조 및 에탄올 수증기 개질 반응으로의 적용”, 2012 년

한국공업화학회 춘계학술회의, 2P-203, 김대중컨벤션센터 (2012/5/9-11).

15. **한승주**, 방용주, 서정길, 윤민혜, 송인규, “중형기공성 알루미나-지르코니아 복합 제어로젤 담체에 담지 니켈 촉매 상의 에탄올 수증기 개질 반응을 통한 수소 가스 생산”, 2012 년 한국화학공학회 춘계학술회의, P 촉매금-33, 제주 ICC (2012/4/25-27).

Domestic conferences (Co-author)

1. 강기혁, **한승주**, 이종원, 유재경, 박승원, 이어진, 송인규, “붕소가 첨가된 Re-Ru/C 촉매 상에서 숙신산의 수소화를 통한 1,4-부탄디올의 제조”, 2016 년 한국화학공학회 추계학회, P 촉매금-94, 대전 DCC (2016/10/19-21).

2. 유재경, **한승주**, 박승원, 송지환, 송인규, “담지 과정에서 계면활성제를 도입한 니켈/알루미나 제로젤 촉매 상에서 천연가스의 수증기 개질 반응을 통한 수소 생산”, 2016 년 한국화학공학회 추계학회, P 촉매금-34, 대전 DCC (2016/10/19-21).

3. 박승원, **한승주**, 유재경, 송지환, 이어진, 송인규, “니켈-붕소-알루미나 제로젤 촉매 상에서 수소 가스 생산을 위한 액화천연가스의 수증기 개질 반응”, 2016 년 한국화학공학회 추계학회, P 촉매금-35, 대전 DCC (2016/10/19-21).

4. 송지환, **한승주**, 유재경, 박승원, 송인규, “니켈-스트론튬-알루미나-지르코니아 에어로젤 촉매 상에서의 에탄올 수증기 개질 반응을 통한 수소 가스 생산”, 2016 년 한국화학공학회 추계학회, P 촉매금-36, 대전 DCC (2016/10/19-21).

5. 유재경, **<u>한승주</u>**, 박승원, 송지환, 송인규, “바나듐-니켈-알루미나 제로젤 촉매 상에서 천연가스의 수증기 개질 반응을 통한 수소 생산”, 2016 년 한국화학공학회 춘계학회, P 촉매금-27, 부산 BEXCO (2016/4/27-29).

6. 박승원, **<u>한승주</u>**, 유재경, 송지환, 송인규, “비금속 조촉매로 붕소를 도입한 중형기공성 니켈-붕소-알루미나 제로젤 촉매 상에서 액화천연가스의 수증기 개질 반응을 통한 수소 가스 생산”, 2016 년 한국화학공학회 춘계학회, P 촉매금-28, 부산 BEXCO (2016/4/27-29).

7. 송지환, **<u>한승주</u>**, 유재경, 박승원, 송인규, “지르코니아 촉매 상에서 에탄올 수증기 개질 반응을 통한 수소 가스 생산”, 2016 년 한국화학공학회 춘계학회, P 촉매금-31, 부산 BEXCO (2016/4/27-29).

8. 김민영, **<u>한승주</u>**, 강기혁, 강태훈, 김태협, 송인규, “텅스텐 산화물이 담지된 제올라이트 촉매상에서 메탄의 직접탈수소방향족화 반응을 통한 BTX 생산”, 2016 년 한국화학공학회 춘계학회, P 촉매금-50, 부산 BEXCO (2016/4/27-29).

9. 강기혁, **<u>한승주</u>**, 이종원, 강태훈, 유재경, 송인규, “중형기공성 탄소 담체에 담지된 귀금속 촉매 상에서 숙신산의 수소화를 통한 1,4-부탄디올의 제조”, 2016 년 한국화학공학회 춘계학회, O 촉매 J 목-1, 부산 BEXCO (2016/4/27-29).

10. 유재경, **<u>한승주</u>**, 박승원, 송지환, 송인규, “Hollow sphere 구조를 갖는 니켈-알루미나 촉매 상에서의 메탄의 삼중 개질 반응”, 2015 년 한국화학공학회 추계학술회의, P 촉매금-7, 일산 KINTEX (2015/10/21-23).

11. 송지환, **<u>한승주</u>**, 유재경, 박승원, 송인규, “알칼리 토금속 조촉매가

도입된 니켈/알루미나-지르코니아 촉매 상의 에탄올 수증기 개질 반응을 통한 수소 가스 생산", 2015 년 한국화학공학회 추계학술회의, P 촉매금-10, 일산 KINTEX (2015/10/21-23).

12. 박승원, 송인규, **한승주**, 유재경, 송지환, "중형기공성 니켈-붕소-알루미나 제로젤 촉매 상의 액화천연가스 수증기 개질 반응을 통한 수소 가스 생산", 2015 년 한국화학공학회 추계학술회의, P 촉매금-12, 일산 KINTEX (2015/10/21-23).

13. 김태협, 강기혁, 이종권, **한승주**, 최원춘, 박용기, 송인규, "크로미아 기반 금속 산화물 촉매 상에서 프로판의 탈수소화 반응을 통한 프로필렌의 제조", 2015 년 한국화학공학회 추계학술회의, P 촉매금-14, 일산 KINTEX (2015/10/21-23).

14. 박승원, 방용주, **한승주**, 유재경, 송지환, 송인규, "에폭사이드 기반 졸겔법으로 제조된 중형기공성 니켈-철-알루미나 제로젤 촉매 상의 액화천연가스 수증기 개질 반응을 통한 수소 가스 생산", 2015 년 한국화학공학회 춘계학술회의, P 촉매목-3, 제주 ICC (2015/4/22-24).

15. 유재경, 방용주, **한승주**, 박승원, 송지환, 송인규, "니켈-알루미나 에어로젤 촉매 상에서의 메탄의 삼중 개질 반응", 2015 년 한국화학공학회 춘계학술회의, P 촉매목-4, 제주 ICC (2015/4/22-24).

16. 강기혁, 김정권, 이종권, **한승주**, 김태협, 송인규, "레늄-루세늄 이중금속 촉매 상에서 숙신산의 수소화를 통한 1,4-부탄디올의 제조", 2015 년 한국화학공학회 춘계학술회의, P 촉매목-6, 제주 ICC (2015/4/22-24).

17. 강기혁, 홍웅기, 전진오, 방용주, 최정호, **한승주**, 송인규, "레늄-구리-카본 복합체 촉매 상에서 숙신산의 수소화를 통한 감마부티로락톤과

1,4-부탄디올의 제조”, 2014 년 한국화학공학회 추계학술회의, P 촉매금-2, 대전 DCC (2014/10/22-24).

18. 유재경, 방용주, **한승주**, 박승원, 송인규, “세리아를 담체로 이용한 니켈 촉매 상에서의 메탄의 삼중 개질 반응”, 2014 년 한국화학공학회 추계학술회의, P 촉매금-6, 대전 DCC (2014/10/22-24).

19. 박승원, 방용주, **한승주**, 유재경, 송인규, “중형기공성 니켈-철-알루미나 제로젤 촉매 상의 액화천연가스 수증기 개질반응을 통한 수소가스 생산”, 2014 년 한국화학공학회 추계학술회의, P 촉매금-8, 대전 DCC (2014/10/22-24).

20. 방용주, 박승원, **한승주**, 유재경, 최정호, 송인규, “킬레이트화된 니켈 전구체의 함침을 통한 니켈/알루미나 촉매의 제조 및 액화천연가스의 수증기 개질 반응으로의 적용”, 2014 년 한국화학공학회 추계학술회의, P 촉매금-11, 대전 DCC (2014/10/22-24).

21. 방용주, **한승주**, 유재경, 박승원, 최정호, 송인규, “탄소 입자를 주형 물질로 하는 중형기공성 니켈-인-알루미나 촉매의 제조 및 액화천연가스의 수증기 개질 반응으로의 적용”, 2014 년 한국공업화학회 춘계학술회의, 1P-256, 제주 ICC (2014/4/30-5/2).

22. 박승원, 방용주, **한승주**, 유재경, 송인규, “에폭사이드 기반 졸-겔법을 통해 제조된 니켈-철-알루미나 제로젤 촉매의 액화천연가스 수증기 개질 반응으로의 적용”, 2014 년 한국공업화학회 춘계학술회의, 1P-262, 제주 ICC (2014/4/30-5/2).

23. 유재경, 방용주, **한승주**, 송인규, “세리아가 포함된 중형기공성 니켈 촉매 상에서 메탄의 삼중 개질 반응을 통한 수소 가스 생산”, 2014 년

한국공업화학회 춘계학술회의, 1P-265, 제주 ICC (2014/4/30-5/2).

24. 박승원, 방용주, **한승주**, 유재경, 송인규, “중형기공성 니켈-철-알루미나 제로젤 촉매 상의 액화천연가스의 수증기 개질 반응을 통한 수소 가스 생산”, 2014 년 한국화학공학회 춘계학술회의, P 촉매금-68, 창원 컨벤션센터 (2014/4/23-25).

25. 유재경, 방용주, **한승주**, 송인규, “세리아의 도입이 니켈계 촉매 상에서의 메탄의 삼중 개질 반응에 미치는 영향”, 2014 년 한국화학공학회 춘계학술회의, P 촉매금-69, 창원 컨벤션센터 (2014/4/23-25).

26. 방용주, **한승주**, 유재경, 박승원, 최정호, 송인규,“인이 도입된 중형기공성 니켈-알루미나 촉매 상의 액화천연가스의 수증기 개질 반응”, 2014 년 한국화학공학회 춘계학술회의, O 촉매목-10, 창원 컨벤션센터 (2014/4/23-25).

27. 방용주, **한승주**, 유재경, 최정호, 송인규, “인이 도입된 중형기공성 니켈-인-알루미나 에어로젤 촉매의 제조 및 액화천연가스의 수증기 개질 반응으로의 적용”, 2013 년 한국공업화학회 추계학술회의, 2P-253, 대전 컨벤션센터 (2013/10/30-11/1).

28. 유재경, 방용주, **한승주**, 송인규, “중형기공성 니켈-알루미나 촉매 상의 액화천연가스의 수증기 개질 반응에 마그네슘 조촉매의 도입이 미치는 영향”, 2013 년 한국공업화학회 추계학술회의, 2P-179, 대전 컨벤션센터 (2013/10/30-11/1).

29. 방용주, **한승주**, 유재경, 최정호, 송인규, “인이 도입된 중형기공성 니켈/알루미나 제어로젤 촉매 상의 액화천연가스의 수증기 개질 반응을 통한 수소 가스 생산”, 2013 년 한국화학공학회 추계학술회의,

P 촉매목-2, 대구 EXCO (2013/10/23-25).

30. 유재경, 방용주, **한승주**, 송인규, “마그네슘을 조촉매로 첨가한 중형기공성 니켈-알루미나 촉매의 제조 및 액화천연가스(LNG)의 수증기 개질 반응으로의 적용”, 2013 년 한국화학공학회 추계학술회의, P 촉매목-9, 대구 EXCO (2013/10/23-25).

31. 방용주, **한승주**, 유재경, 서정길, 송인규, “인이 도입된 중형기공성 Ni-P2O5-Al2O3 제어로젤 촉매의 제조 및 액화천연가스의 수증기 개질 반응으로의 적용”, 2013 년 한국공업화학회 춘계학술회의, 1P-459, 제주 국제컨벤션센터 (2013/5/1-3).

32. 유재경, 방용주, **한승주**, 서정길, 송인규, “중형기공성 M/니켈-알루미나(M=Mg, Ca, Sr 및 Ba) 촉매 상의 액화천연가스의 수증기 개질 반응을 통한 수소 가스 생산”, 2013 년 한국공업화학회 춘계학술회의, 1P-398, 제주 국제컨벤션센터 (2013/5/1-3).

33. 방용주, **한승주**, 유재경, 서정길, 송인규, “기공팽창제가 도입된 중형기공성 니켈-알루미나 촉매 상의 액화천연가스의 수증기 개질 반응을 통한 수소 가스 생산”, 2013 년 한국화학공학회 춘계학술회의, O 촉매 I 목-23, 광주 김대중컨벤션센터 (2013/4/24-26).

34. 유재경, 방용주, **한승주**, 서정길, 송인규, “알칼리 토금속을 첨가한 중형기공성 니켈-알루미나 촉매의 제조 및 액화천연가스(LNG)의 수증기 개질 반응으로의 적용”, 2013 년 한국화학공학회 춘계학술회의, P 촉매금-10, 광주 김대중컨벤션센터 (2013/4/24-26).

35. 방용주, **한승주**, 유재경, 서정길, 윤민혜, 송인규, “기공팽창제의 도입을 통한 정렬된 중형기공을 갖는 니켈-알루미나 촉매의 제조 및

액화천연가스의 수증기 개질 반응으로의 적용”, 2012 년 한국공업화학회 추계학술회의, 2P-179, 대전컨벤션센터 (2012/10/31-11/2).

36. 방용주, **<u>한승주</u>**, 유재경, 서정길, 윤민혜, 송인규, “정렬된 중형기공을 갖는 니켈-알루미나 촉매 상의 액화천연가스의 수증기 개질 반응을 통한 수소 가스 생산”, 2012 년 한국화학공학회 추계학술회의, P 촉매수-15, 부산 BEXCO (2012/10/24-26).

37. 방용주, **<u>한승주</u>**, 서정길, 윤민혜, 송인규, “정렬된 기공 구조를 갖는 중형기공성 니켈-알루미나 촉매의 제조 및 액화천연가스의 수증기 개질 반응으로의 적용”, 2012 년 한국공업화학회 춘계학술회의, 2P-175, 김대중컨벤션센터 (2012/5/9-11).

38. 방용주, 이중원, **<u>한승주</u>**, 서정길, 윤민혜, 송인규, “탄소 입자를 주형 물질로 하여 제조된 중형기공성 니켈-알루미나 제어로젤 촉매 상의 액화천연가스의 수증기 개질 반응을 통한 수소 가스 생산”, 2012 년 한국화학공학회 춘계학술회의, P 촉매금-24, 제주 ICC (2012/4/25-27).